Design and Simulation of Pixel Layout and Data Processing Algorithms for the DEEP Instrument

A thesis by

Hogne Andersen

for the degree of

Master of Science in Physics

Department of Physics and Technology

University of Bergen

September 2018

Abstract

A team of researchers at Birkeland Centre for Space Science is developing an instrument that is able to measure particle precipitation into the atmosphere. The instrument consist of both electron and proton detectors, hence the name Distribution of Energetic Electron and Proton (DEEP) instrument. This thesis initiates and specifies the functions of the Digital Signal Processing (DSP) needed for the instrument.

This works covers the design and development of the three main DSP functions; the coincidence check, data binning and data packet. Coincidence check is used to determine the energy of the incoming particle and will be used to determine the direction of the incoming particle (Front→Back or Back→Front). Data binning is used to reduce the data size and make it possible to transfer the data with a satellite link, and the required bin sizes are proposed. As part of the packet definition, the structure of the electron and proton payload data packet is specified, and the payload data sizes are calculated based on various energy channels. GATE simulations are used to investigate the electron scattering. A total of 7 distinct DEEP relevant geometries were designed, and for each geometry a total of 7 simulations were computed with energies ranging from 30 to 1920 keV. A complete GATE simulation guide for the DEEP instrument is written as well.

It was uncovered that scattering, out of a pixel, increases with energy of the incoming electron. At low energies this was negligible. At higher energies, scattering caused problems when evaluating the readout. To manage this at higher energies a combination of super pixels and a wolfram-mask was designed. By using the mask, significant improvement were observed at higher energies, and some improvement were observed at lower energies.

Preface

This work was carried out at the Department of Physics and Technology at the University of Bergen (UiB) between August 2017 and September 2018.

The DEEP project is a relatively new project at Birkeland Centre for Space Science, and little relevant documentation and information existed. Solving challenges that appeared was done without much prior knowledge, especially regarding the GATE simulations and all its different parts. In specific, the major parts related to the GATE simulations were the GATE macro language and the ROOT data analysis framework. An introduction course in ROOT was taken alongside the thesis work in the first semester.

Some work has been done on analog-to-digital converting in a previous master thesis and some work has been done on the pre-amplifying and signal-shaping in another master thesis. At the time of writing an ongoing PhD candidate focuses on front-end electronics, with a focus on converting the signal from the sensor into digital format.

Acknowledgments

I would like to express my gratitude to the DEEP project team consisting of my supervisors Professor **Kjetil Ullaland** and Associate Professor **Johan Alme**, Researcher and Team Leader at the Birkeland Centre of Space Science **Hilde N. Tyssøy**, Professor Emeritus **Johan Stadsnes** and PhD Candidate **Are Haslum**. Thank you for all your contributions.

A special salute to all of my **fellow students at room 312** and PhD Candidate **Magnus R. Ersdal**. You have all made these two years more enjoyable.

Finally, I would like to thank my **friends**, and my **family** for always being there for me. A special thanks to **Eva** for comments and suggestions.

Hogne Andersen
Bergen, September 2018

Contents

Nomenclature

Acronyms and Abbreviations

ADC	Analog-to-Digital Converter
Al	Aluminium
ASC	Andøya Space Center
ASCII	American Standard Code for Information Interchange
ASIC	Application-Specific Integrated Circuit
BCCS	Birkeland Centre for Space Science
CCD	Charge-Coupled Device
CLHEP	Class Library for High Energy Physics
CME	Coronal Mass Ejection
CMOS	Complementary Metal–Oxide–Semiconductor
CPU	Central Processing Unit
CRC	Cyclic Redundancy Check
CSDA	Continuous-Slowing-Down Approximation
CSV	Comma-Separated Values
CT	Computed Tomography
DEEP	Distribution of Energetic Electron and Proton
DH	Detector House
E	Energy
ECC	Error-Correcting Code
EDS	Electron Detector System
EISCAT3D	European Incoherent SCATter scientific association
EMIC	ElectroMagnetic Ion Cyclotron
ENA	Energetic Neutral Atom
ESFRI	European Strategy Forum on Research Infrastructures
eV	electron Volt
FIFO	First In, First Out
FPGA	Field-Programmable Gate Array
GATE	GEANT4 Application for Emission Tomography
GEANT	GEometry ANd Tracking

H	Hydrogen
He	Helium
IC	Integrated Circuit
I/O	Input/Output
ISS	International Space Station
LEO	Low Earth Orbit
LTS	Long Term Support
MEPED	Medium Energy Proton and Electron Detector
N	Nitrogen
NBS	National Bureau of Standards
Ni	Nickel
NIST	National Institute of Standards and Technology
O	Oxygen
PET	Positron Emission Tomography
PDS	Proton Detector System
PLL	Phase-Locked-Loop
POES	Polar Orbiting Environmental Satellites
RAM	Random-Access Memory
RTL	Register-Transfer-Level
SCT	Scattering
SEE	Single Event Effect
SER	Soft Error Rate
SFF	Senter for Fremragende Forskning
Si	Silicon
SIOS	Svalbard Integrated arctic earth Observing System
SNR	Signal-to-Noise Ratio
SoC	System on Chip
SPE	Solar Proton Event
SPECT	Single Photon Emission Computed Tomography
SP	Super Pixel
SRAM	Static Random-Access Memory
TAE	Total Absorbed Energy
TID	Total Ionizing Dose
TMR	Triple-Module-Redundancy
TOT	Time Over Threshold
UiB	University of Bergen
UV	UltraViolet
UVVM	Universal VHDL Verification Methodology
W	Wolfram
VHDL	VHSIC Hardware Description Language
VHSIC	Very High Speed Integrated Circuit

CHAPTER 1

Introduction

1.1 Background and Motivation

The primary scientific objective for the Distribution of Energetic Electron and Proton (DEEP) instrument is to accurately quantify energetic electron precipitation into the atmosphere [1]. Electrons below 1 MeV deposits their energy between 50 and 100 km altitude. The resulting ionization is of great importance for changing chemistry and dynamics in this altitude region. To accurately quantify this effect, a good estimate of the energy deposited in the atmosphere and how energy is distributed globally is required. The instrument is designed to fly on a small satellite in Low Earth Orbit (LEO) at 600 to 800 km altitude. The current particle detectors already in space, have a design and/or orbit inadequate for determining the amount of particles precipitating into the atmosphere. The amount of electrons observed by a detector might vary strongly with the detectors pointing direction relative to Earth's magnetic field. This is called the pitch angle distribution and is not properly monitored by current detectors in space.

Measurements from the DEEP instrument will provide new information supporting scientific questions studied at Birkeland Centre for Space Science (BCSS); What are the effects of particle precipitation on the atmosphere? BCSS is a Norwegian Centre of Excellence (SFF) whose primary objective is to try to understand the Earth's relationship to space [2]. These measurements are highly relevant for observational European Strategy Forum on Research Infrastructures (ESFRI) programs like Svalbard Integrated arctic earth Observing System (SIOS), European Incoherent SCATter scientific association (EISCAT3D) and measurements done with rocket campaigns at Andøya Space Center (ASC).

1.2 Thesis Objective

The DEEP project plans to use three Electron Detector Systems (EDS), and three Proton Detector Systems (PDS). By doing this, a field of view of 180° is achieved. Each system consists of a front and a back detector. The front and back detectors of the EDS are divided into eight separate patches (pixelated design) to facilitate a high angular resolution. The front and the back detector of the PDS are divided into four separate patches. Protons contaminate the measurements in the EDS system as there is no way of filtering out protons. By having a separate proton detector the contamination can be accounted for. In the PDS only protons is measured, because electrons is filtered out by employing magnets. The EDS is capable of measuring electrons in the range of 30 keV to 2 MeV. The PDS is capable of measuring protons in the range of 30 keV to 10 MeV.

A particle that hit the sensor deposits energy and the sensor will then convert the deposited energy to an electrical signal. From the sensor the signal is fed into the front-end electronics. The front-end electronics purpose is to amplify and shape the signal before it is digitized. After digitization the signal is fed into the back-end electronics. The back-end electronics consist of a Field-Programmable Gate Array (FPGA), inside the FPGA the Digital Signal Processing (DSP) is achieved. The DSP will analyse the data and prepare it for storage. The conceptual design is illustrated in figure 1.1.

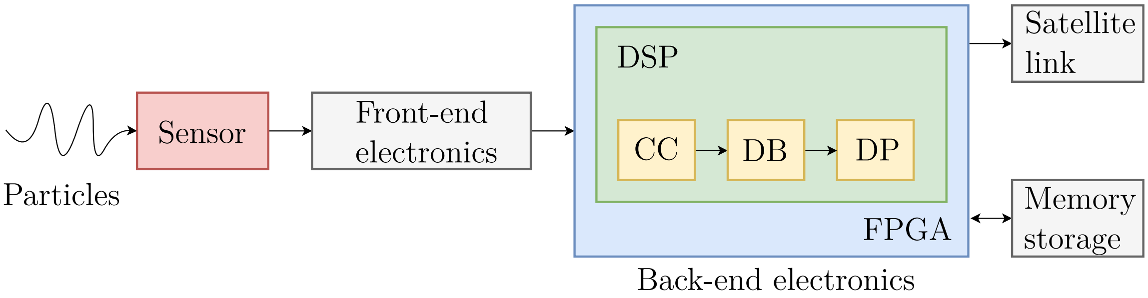

Figure 1.1: Conceptual overview of the readout chain for the DEEP instrument.

The primary goal of this thesis is to define the specifications and requirements for the DSP needed for the DEEP instrument. This work covers the design and development of the three main DSP functions; the coincidence check (CC), data binning (DB) and data packet (DP). Coincidence check is used to determine the energy of the incoming particle, and will be used to determine if the particle hit the front or the back layer first. Data binning is used to reduce the data size and to make it possible to transfer the data with a satellite link, and the required bin sizes are proposed. The structure of the electron and proton payload is specified as part of the packet definition.

A significant effort was put on GATE simulations to investigate if electron scattering could cause a problem when evaluating the readout. The majority of this work was put on designing a total of seven distinct DEEP relevant geometries. Particular emphasis was put into investigating and validating suitable physics lists to be utilized in the simulations. A solution to reduce scattering is proposed and effectiveness is validated with simulations. A complete GATE simulation guide for the DEEP instrument is created as well.

A strong emphasis has been put on documentation and version control in the simulation phase to ease future simulations. All code and documentation are collected in a structured hierarchy of folders. All C and VHDL code written complies to the department's guidelines. All simulations and testing are accomplished by using scripts to automate the process as much as possible. A strong focus has been put on collaboration with the scientists involved in the project.

1.3 Thesis Outline

This thesis is divided into the following chapters:

Chapter 2: Sun, Earth, and Particle Interaction This chapter starts with explaining the origin of electron and proton particles. It gives further information about how the Earth and the Sun are linked together. Information about Earth's magnetic field and atmosphere is given as well. Finally, how electrons and protons interact with matter is explained. This theory is required to understand why such emphasis has been put on the GATE simulations.

Chapter 3: Radiation Detector Systems in Space This chapter provides a brief explanation of the basics of a semiconductor-based detector system and problems that may occur in space due to radiation. This theory is required to understand how the DEEP instrument work, as well as which design steps are needed to make sure the electronics survive in the harsh space environment.

Chapter 4: DEEP Instrument This chapter describes the DEEP instrument and gives theoretical information on how the underlying electronics involved in the system work. Both the electron and the proton detector systems are described, as well as the sensor and detector house. Detailed information about the front-end electronics and a brief introduction to the back-end electronics is given as well.

Chapter 5: GATE Simulation Setup This chapter explains how the GATE simulation setup geometries for the DEEP instrument are designed, and discusses the necessary simulation parameters needed. Validation of the physics list utilized is also performed. Finally, a brief explanation on how the data extraction and processing of the simulation output data is done.

Chapter 6: GATE Simulation Results This chapter evaluates the results from various GATE simulations. In addition, a simulation setup for future simulations is proposed.

Chapter 7: Back-end Electronics This chapter gives a detailed explanation of the back-end electronics and the DSP components involved. The section on coincidence provides a solution to the electron scattering. The data binning section provides a discussion on data binning for various bit precisions based on the expected count rate out of the front-end electronics. Based on the previous discussions, a data packet is proposed. It includes a discussion on the packet size as well. Finally, a system implementation and test system is proposed and discussed.

Chapter 8: Discussion and Conclusion This chapter summarizes the work for this thesis, and then discusses the further work required to complete the system. Finally, there is a section that concludes the thesis and the results of the work.

Appendices The last section of the thesis includes multiple appendices which includes too many details to be included in the main sections of the thesis. It includes a complete GATE simulation guide which aims to give the necessary information and documentation for installing and running a GATE simulation. It provides a detailed explanation of how the data extraction and processing of the GATE simulation output data was designed. Detailed results of the DEEP simulation results is also provided. Lastly, information about the GATE simulation and testbench framework repositories is given.

1.4 Citation Principles

This thesis is using the principle that citations listed in the chapter or section introduction refers to statements in that chapter or section. Citations listed before any punctuation will always refer to the last statements.

CHAPTER 2

Sun, Earth, and Particle Interaction

This chapter aims to give background information on how the Sun and the Earth are linked together. There will also be given an introduction on the fundamentals of electrons and protons, and how they interact with matter.

2.1 The Sun

The Sun is a G-type main sequence star (G2V) and constitute 99.86% of the total mass in our Solar System. The mass consists mainly of Hydrogen (H) and Helium (He). The Sun produces energy by fusion of the hydrogen atom, and the energy flux out to 0.7 of the solar radii is mainly transported through radiation. Beyond this radius the plasma density is adequate for the formation of convection cells, and the energy can be effectively transported through these. Information is this section is based on [3], [4], [5], and [6].

The floating body of the Sun causes an exciting phenomenon. The mass on the equator rotates faster than on the poles, twisting the magnetic field lines near the surface. It takes in average 27 days for the Sun to rotate on its axis, while at the equator it takes 24 days, and the poles takes more than 30 days. This distortion causes regions of stronger magnetic fields, where the temperature and particle density is reduced, due to reduced convection. Since the magnetic field strength is not evenly distributed over the whole surface, there will be areas that are cooler than others. These areas will be associated with less radiation and hence they appear darker compared to the rest of the solar disk. These darker areas are known as sunspots. The lower density in these areas also cause the magnetic field lines to rise to the surface, and eventually bends over the surface between two sunspots. As a result, sunspots are formed in pairs where they have different magnetic polarity, and huge amounts of plasma are collected along the lines.

A phenomenon associated with sunspots is the Coronal Mass Ejection (CME). CME is an unusually large discharge of plasma which carry an embedded magnetic field from the Suns corona. The released plasma will travel with the solar wind. A CME is relatively slow and will reach Earth in one to five days. When a CME hits the Earth, it can cause a geomagnetic storm. Large geomagnetic storms can cause damage to spacecrafts, such as communication satellites. Geomagnetic storms can also cause power outage at Earth. Astronauts and electronics located beyond the atmosphere of the Earth could be harmed during such a storm.

The solar wind is a stream of charged particles ejected from the Sun. The solar wind protects the Solar System from cosmic radiation, and as a result the Earth is protected from high-energetic radiation from outer space. Earth, however, must in turn protect itself from the solar wind. The solar wind has a velocity of about 400 km/s, which implies it takes 2-4 days before it reaches Earth, from the Sun.

Many phenomena on Earth are caused by the solar wind, such as the Aurora which occur around the Earth's magnetic poles. This phenomenon can be observed when high-energetic particles trapped in the Earth's magnetic field hits different atoms and molecules in the atmosphere. The incoming particles follow the magnetic field lines toward the poles, where they ionize and excite particles in the Earth's upper atmosphere creating the Auroras. The different colours are determined by the wavelength of the emitted light corresponding to the excited states of Oxygen (O) and Nitrogen (N). Hence, the colour depends on the composition and density of the atmosphere, as well as the energy of the incoming particles.

2.2 The Earth

Earth is the only planet in our Solar System with an atmosphere that can sustain life. The blanket of gases not only contain the air that many inhabitants on Earth are dependent on, but also protects them from the blasts of heat and radiation emanating from the Sun. These gases warms the planet by day, and cools it at night. Information in this section is based on [4], and [7].

2.2.1 The Magnetic Field

The magnetic field surrounding the Earth protects the planet from the high-energy particles in the solar wind. Earth's magnetic field can be seen, to a first approximation, as symmetrical about an axis through the geomagnetic poles. This is called a dipole field and, as a result, the planet is a dipole magnet. A magnetic field resides from the south hemisphere (magnetic north) to the north hemisphere (magnetic south) offset to the geographic poles. Earth's magnetic field is illustrated in figure 2.1.

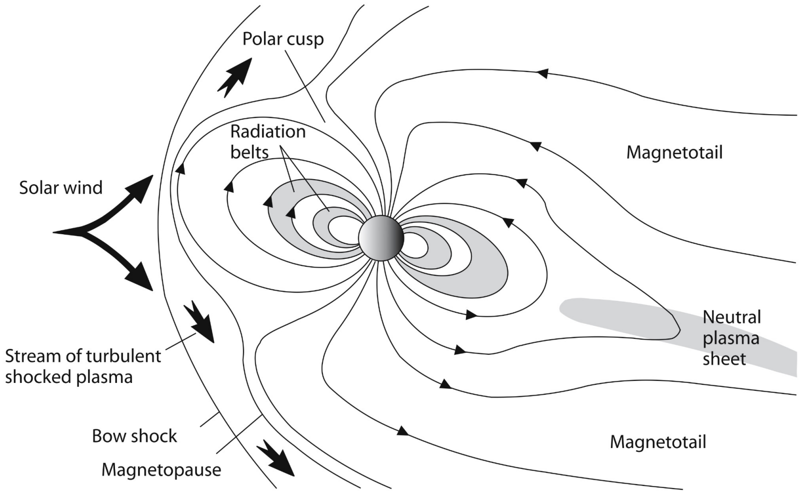

Figure 2.1: The magnetosphere is the region where Earth's magnetic field predominates. The magnetosheath is the region where the field shares its effects with the solar field. The magnetopause is the boundary between these two regions. The region outside the bow shock is where the interplanetary field predominates. The location of the radiation belts can also be observed [8].

In the magnetosphere, the magnetic field are so strong that it prevents direct penetration of plasma. The outer boundary of the magnetosphere is called the magnetopause. The magnetic field is not able to stop all the incoming particles in the solar wind. The shielding is also weaker around the poles. In this area some of the precipitating particles have energies that allow them to penetrate into the atmosphere. The solar wind interferes with Earth's dipole field with the continuous flux of charged particles. On the day side, facing the Sun, a shock front is formed due to particle compression, and within this area it is very turbulent. At night, the magnetic field lines are pulled outward and form a tail. In this area, the solar wind plasma can switch to magnetosphere plasma. Due to the variation in strength of the solar wind, and the major problems it can cause on Earth, it is important to study it further so that space weather can be predicted.

The radiation belts, which might be harmful for space instrumentation, were discovered with the satellite Explorer 1. The satellite had a Geiger counter on board and detected electrically charged particles. These belts mainly consist of electrons and protons, both of which are trapped in the Earth's magnetic field. The inner belt primarily contains protons, while the outer belt contains electrons. Around 1895, Kristian Birkeland considered the possibility of these trapped particles [9], but it was the American satellite that first observed them in 1958. The solar wind interaction with the magnetosphere affects the radiation belts, and especially the outer belt varies with the intensity of the solar wind. The outer belt extends from 15,000 to 25,000 km from the Earth's surface.

2.2.2 Pitch Angle

The angle between the particle velocity vector and the magnetic field is called the pitch angle. This relationship is illustrated in figure 2.2. Information in this section is based on [10].

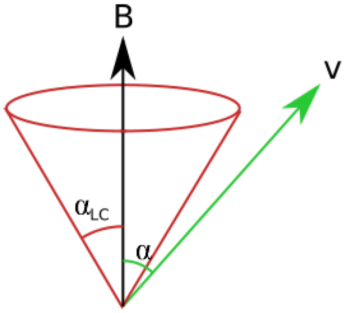

Figure 2.2: Illustration of the velocity vector (V) of an electron, and its pitch angle (α), relative to the magnetic field (B). All electrons that have pitch angles inside the loss cone (α_{LC}) will be lost to the atmosphere [10].

All charged particles trapped in the Earth's magnetic field can be characterized by their pitch angle. Due to conservation of magnetic moment, the pitch angle will increase when a particle moves into a converging magnetic field. If the angle reaches 90°, the particle will mirror back along Earth's field line. If the mirroring point is less than ~100 km altitude, the particle will be lost to the atmosphere. Hence, all particles with smaller pitch angles than the ones mirroring at 100 km, is said to be in the loss cone. The particle mirroring can be observed as a bouncing motion and this is illustrated in figure 2.3.

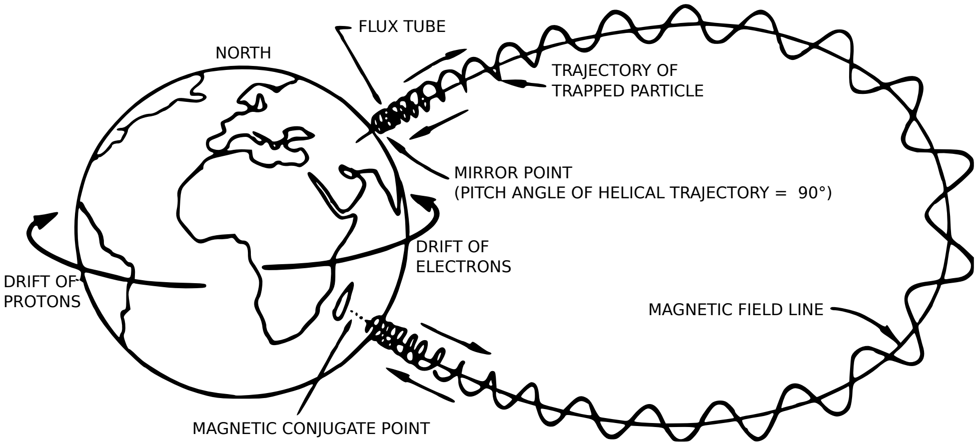

Figure 2.3: Illustration of the three basic motions of charged particle trapped in the Earth's magnetic field: Gyro, bounce (mirroring), and drift [8].

The pitch angle will change throughout the motion, as the particle bounces back and forth along the field lines between each hemisphere. The pitch angle grows bigger as the particle approaches the polar regions. The pitch angle is smallest in the equatorial plane, where the magnetic field strength is weakest. Following the polar magnetic field lines to the equator, the loss cone is less than ∼5° wide, making it difficult for a particle detector at equator to determine the radiation belt loss to the atmosphere. At 600 to 800 km altitude the loss cone size has increased to ∼60° wide, making it possible for particle detectors to differentiate between particles that will be lost to the atmosphere, and the ones that will mirror. Figure 2.4 illustrates why it is important that the detector has a wide resolved field of view. A good pitch angle resolution will provide a firm estimate of the loss cone.

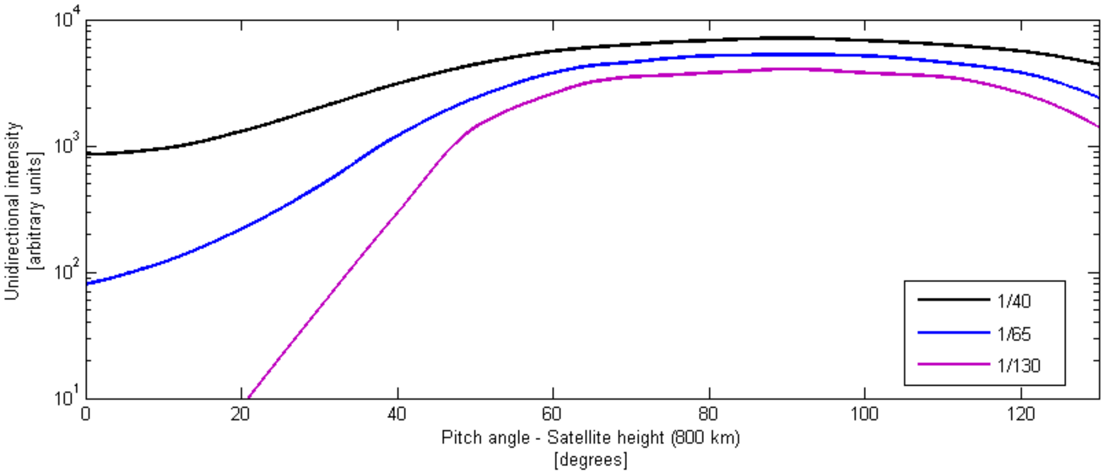

Figure 2.4: Theoretical distribution of fluxes depending on pitch angles at an altitude of 800 km [8].

The pitch angle of an electron can be altered by wave-particle interactions, thus moving a previously trapped electron into the loss cone. There are three types of wave-particle interactions responsible for such pitch angle scattering. Plasmapheric hiss, whistler mode chorus, and ElectroMagnetic Ion Cyclotron (EMIC) waves. In addition to being scattered into the loss cone by these mechanisms, particles may be lost to the magnetopause during a geomagnetic storm main phase. Energetic electrons precipitating into the atmosphere has been of high interest for scientists in the recent years, as the collisions initiate a series of chemical reactions changing the composition of the middle atmosphere (50-120 km). By measuring particles in an altitude of 600 km above the surface one can estimate the flux of particle precipitation into the middle atmosphere.

2.2.3 Atmosphere

The Earth's atmosphere is divided into different layers based on the temperature structure. Upward from the surface, these layers are named troposphere, stratosphere, mesosphere and thermosphere. The atmospheric layers are illustrated in figure 2.5. Information in this section is based on [11], and [12].

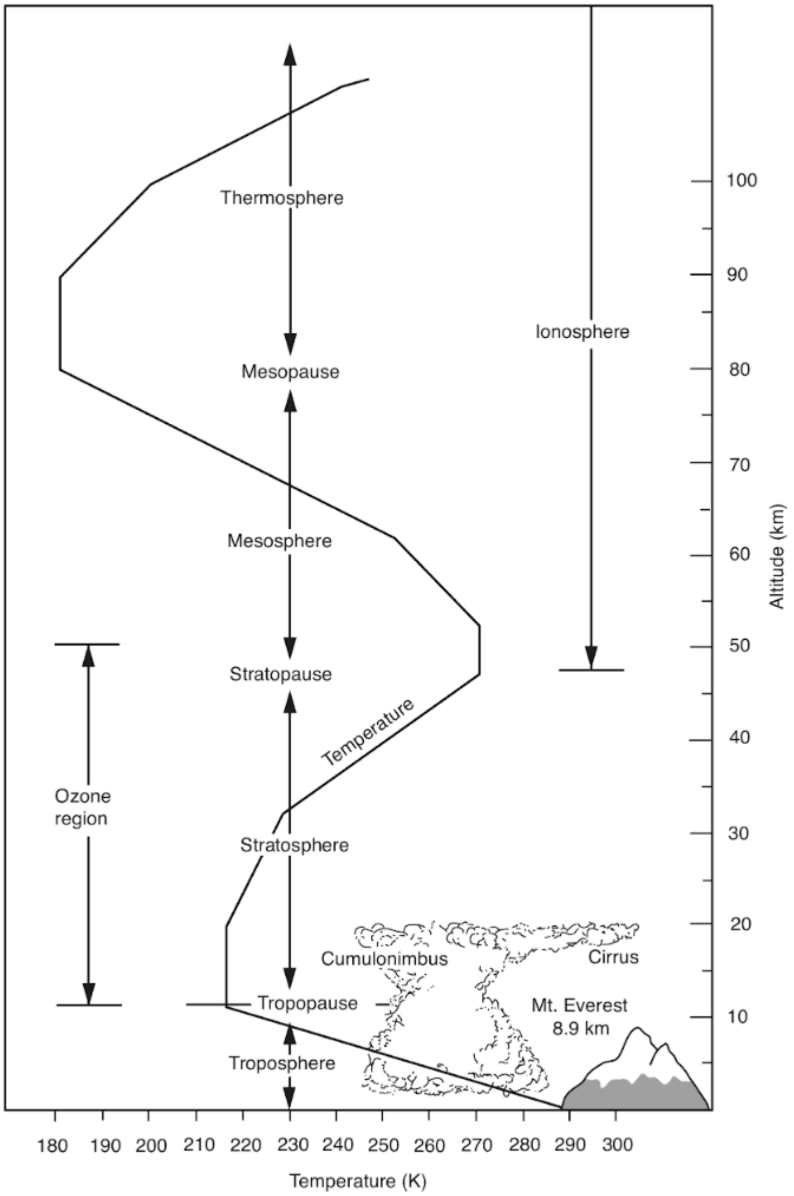

Figure 2.5: One-dimensional structure of Earth's atmosphere [13].

Some of the precipitating particles from the Sun have energies that allow them to penetrate down to the middle atmosphere before their energy is absorbed. The energy transfer from these particles can affect the atmosphere in different ways. Energetic electrons and protons, trapped in the Earth's magnetic field, can collide with gases in our atmosphere. How deep they are able to penetrate into the atmosphere, depends on their initial energy. The altitude versus ionization rates for monoenergetic proton and electrons can be seen in figure 2.6.

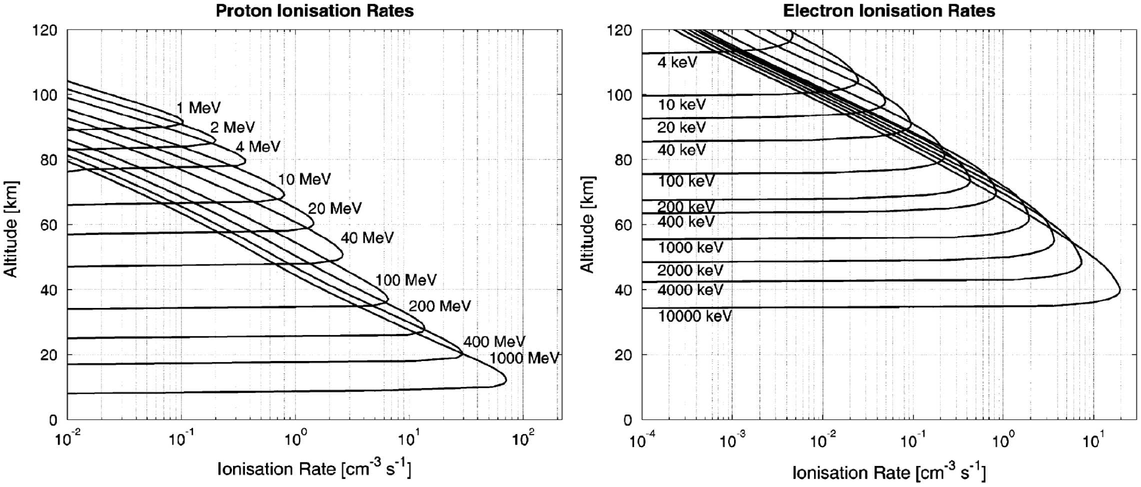

Figure 2.6: Altitude versus ionisation rates for monoenergetic beams of protons 1–1000 MeV (left) and electrons 4–4000 keV (right) [14].

Most particles will be stopped above 100 km. Associated with eruptions on the Sun or periods of high velocity solar winds, some particles may reach as low as 50 km altitude. The collisions initiate several chemical reactions leading to the production of NOx and HOx gases, which in turn can reduce the ozone concentration. Ozone is important in the energy budget at these altitudes. Hence, changing the concentration of ozone at 50 km might also impact temperature and winds. The winds have links to our weather system. A good estimate of the particle energy input, and its altitude distribution is therefore crucial for determining its effects on the atmosphere, as well as its potential impact on the regional surface temperature.

The troposhere is the closest layer to Earth's surface reaching up to 15 km. Temperature decreases with altitude at a nearly constant rate, approximately −6°C per kilometre. A distinctive convective motion characterizes this layer. Dominating climate processes are water vapour, aerosols and the greenhouse gases. Clouds, and nearly all the water vapour and dust in the atmosphere exists in the troposhere. The temperature maximizes near equator and decreases towards each pole. The upper boundary of the troposphere is called the tropopause. In the tropopause the temperature changes, and will start to increase with altitude.

The stratosphere is the second layer. The layer starts from the tropopause up to about 50 km from the Earth's surface. The increase in temperature in the stratosphere is due to heating by ozone absorption of Solar UltraViolet (UV) radiation. Radiative processes dominate the energy flow, as only weak vertical motions of air occur. Weather balloons fly in this region, and the air is very dry. At the top of the stratosphere the stratopause is found, in this region the temperature begin to decrease with altitude again.

The mesosphere is the third layer, it starts at 50 km and extends to a height of 85 km (95 km during the winter). Temperature starts to decrease with altitude as ozone heating decreases. The transportation of energy in this layer is due to radiative processes, and convective and wave motions. The mesopause is found at the top of the mesosphere and is the coldest part of Earth's atmosphere. Here, the temperature ranges between −150°C in winter and −90°C in summer. This is the hardest layer of the atmosphere to study, as air planes and balloons are not able to fly this high, and satellites which travel at a much higher altitude are not able to orbit this low. This means rockets are the only viable option to use when studying this region. Rocket campaigns have shown that meteors burn up in this layer. At approximately 83 km noctilucent clouds can be formed due to the cold temperature. Both season and latitude will affect the altitude of the mesopause.

The thermosphere is the fourth layer and final layer, it extends from around 90 km to between 500 and 1,000 km. The thermosphere is considered to be a part of Earth's atmosphere, but the air density is so low that most of this layer is often referred to as outer space. There is no distinct boundary between the atmosphere and space, but an imaginary line 100 km from the surface, called the Karman line, is usually the definition of where space begins. In this region, which is considered a part of the atmosphere, the International Space Station (ISS) orbits the Earth at about 350-400 km altitude. Temperatures can get up to 2,000°C, and are strongly influenced by Solar activity. This is also the layer where the Aurora occurs, when precipitating particles from space collide with atoms and molecules, which excites them into higher states of energy. The atoms shed this excess energy by emitting photons of light, which can be observed as a colourful display in the sky at high (and low) latitudes.

2.3 Particle Interaction with Matter

Particles interacts with matter in different ways depending on the type of particle. Electrons detected in the DEEP instrument is primarily free electrons which has been accelerated in the magnetosphere. Some electrons may originate from the plasma from the Sun as well. Heavy charged particles are defined as all energetic ions with mass of one atomic mass unit or greater, such as the proton. The traditional unit for measuring particle energy is the electron Volt (eV). Electron volt is defined as the kinetic energy gained by an electron by its acceleration through a potential difference of 1 Volt. Expected particle energies measured by the DEEP instrument is in the order of tens of keV and MeV. Information in this section is based on [15] and [16].

2.3.1 Proton

Protons interact with matter primarily through the coulomb force. This force acts between the positive charge and the negative charge of the orbital electrons within the absorber atom. When protons enters any absorbing medium, it immediately interacts with many electrons. The electron particle in the absorbing medium feel an impulse from the attractive coulomb force as the incoming particle passes its vicinity. This impulse, depending on the proximity, may be sufficient to either raise the electron to a higher laying shell within the absorber atom (excitation), or to remove the electron completely from the atom (ionization). As the charged particle passes through the atom its velocity is decreased, as it encounter a lot of electrons, and the resulting energy is transferred to the electrons.

2.3.2 Electron

Electrons, when compared with heavy charged particles, lose their energy at a lower rate and follow a much more twisted path through absorbing materials. Figure 2.7 (adapted from [15]) illustrates how a series of tracks from a source of monoenergetic electrons might appear.

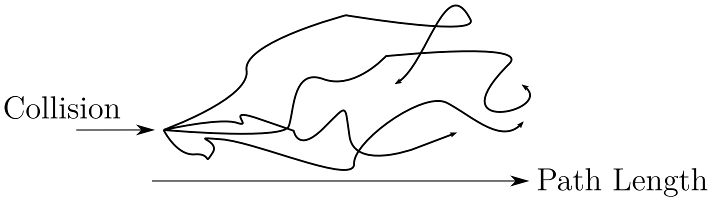

Figure 2.7: Illustration of how a series of tracks from a source of monoenergetic electrons might appear. The electrons approach from the left.

Since the mass of the electron is equal to that of the orbital electron with which it is interacting, a larger fraction of its energy can be lost in a single encounter, and thus a larger deviation in the electron path is possible. Electrons can lose their energy by radiative processes as well as coulomb interactions. In the DEEP instrument, where the detector is made by Silicon (Si), radiative processes can emanate from any position along the electron track. This results in a direction change of the electron.

2.3.3 Straggling

Straggling is defined as the fluctuations in path length for individual particles of the same initial energy. All microscopic interactions experienced by any particle vary randomly, and its energy loss is thus a statistical or stochastic process. This is why a spread in energy is always the result after a beam of monoenergetic charged particles has passed through a given thickness of absorber medium. The resulting width of the energy distribution is the measure of energy straggling. The width varies with the distance along the particle track. The effect play an important role when dealing with electrons. Electron straggling can be observed in figure 2.8 (adapted from [16]). Particles with monoenergetic energy distribution in a medium experience a wider spread as a function of penetration distance, before the width narrows due to the mean particle energy has been greatly reduced.

Slightly different total path lengths are to be expected for charged particles, due to the same stochastic factors that leads to energy straggling at a given penetration distance. For protons the straggling amounts to a few percent of the mean range. The proton straggling can be seen in figure 2.9 (adapted from [16]). The degree of straggling is indicated by the sharpness of the cut-off at the end of the average transmission curve.

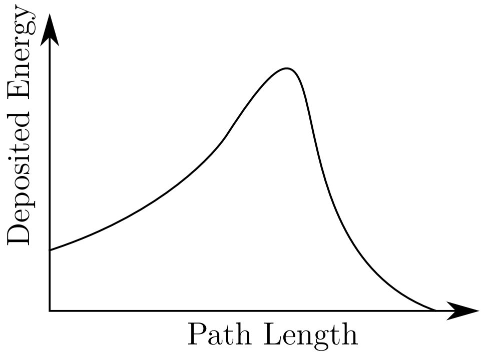

Figure 2.8: Electron straggling with its long tail at the end of the transmission curve.

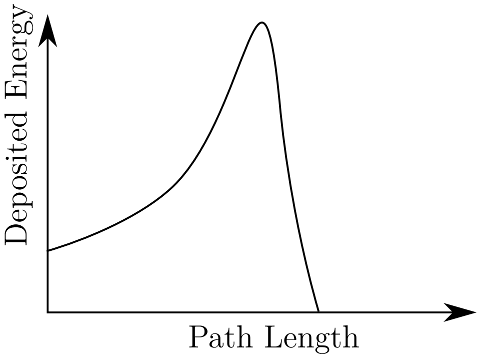

Figure 2.9: Proton straggling with its sharp cut-off at the end of the transmission curve.

2.3.4 Range

When charged particles passes through matter they lose energy (in many steps), until their energy is zero. The distance from the incident to this point is called the range of the particle. The range depends on the type of particle, on its initial energy and on the material it passes through. There are two main ways to give this range, the Continuous-Slowing-Down Approximation (CSDA) and the projected range. Figure 2.10 illustrates the difference between the CSDA and projected range.

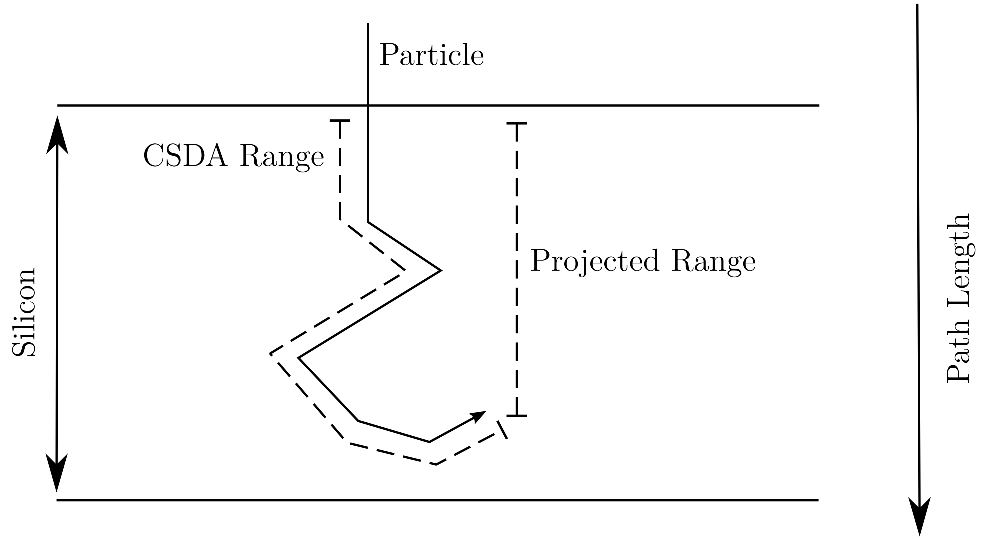

Figure 2.10: Illustration of the difference between CSDA and projected range.

As the particle slows down to rest, the CSDA range is a very close approximation to the average path length travelled by the charged particle [17]. The rate of the energy loss at every point along the track is assumed to be equal to the total stopping power. In this approximation energy-loss fluctuations are neglected. The CSDA range is obtained by integrating the given value of the total stopping power with respect to energy. The projected range is the average value of the depth to which a charged particle will penetrate while slowing down to rest [17]. This depth is measured along the initial direction of the particle.

CHAPTER 3

Radiation Detector Systems in Space

All radiation detector systems include the same basic functions. The signal from each sensor or sensor channel in a detector array is amplified and processed for storage and analysis. Circuit blocks are associated with a distinct function, but frequently circuit blocks is able to perform multiple functions. In this chapter a brief explanation of the basics of a semiconductor-based detector system, and problems that may occur in space will be given. Information in this chapter is based on [18], [19], [20], and [21].

3.1 Semiconductor Detector System

The term detector is open to more than one interpretation, as a detector can consist of several detector subsystems (tracking, calorimetry or particle detection), and each subsystem may in turn consist of several individual detector modules. Hence, a system that translates the presence of a particle to an electrical signal is referred to as a sensor. Figure 3.1 illustrates the basic functionality in such a detector system: Radiation is absorbed in the sensor and converted into an electrical signal. The signal pulse is usually negative, and an inverter inverts it into a positive pulse. The signal, which is low-level, is integrated in a pre-amplifier, and then fed to a pulse shaper before it finally is digitized. After digitization the signal is ready for storage and analysis.

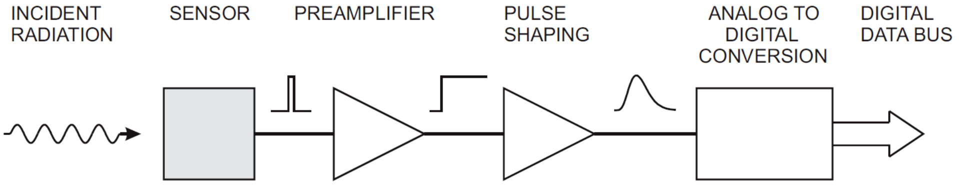

Figure 3.1: Demonstration of the typical basic functions in a detector system [18].

3.1.1 Sensor

When a particle (or photon) deposits energy in a medium, the sensor will convert this energy to an electrical signal. This conversion can be achieved in different ways. In this context energy is absorbed in a semiconductor, such as silicon, which produces mobile charge carriers (electron-hole pairs). An electrical current is induced when the charge carriers are swept to the to electrodes, due to an applied electric field. The number of electron-hole pairs is proportional to the absorbed energy. This means that by integrating the signal current, one obtains the signal charge (which is proportional to the energy). These sensor pulses can be quite short (in order of nanoseconds). A pulse processor can transform a short sensor current pulse into a broader pulse with a peaking time. Semiconductor sensors can handle very high particle rates. Figure 3.2 illustrates a typical semiconductor detector diode.

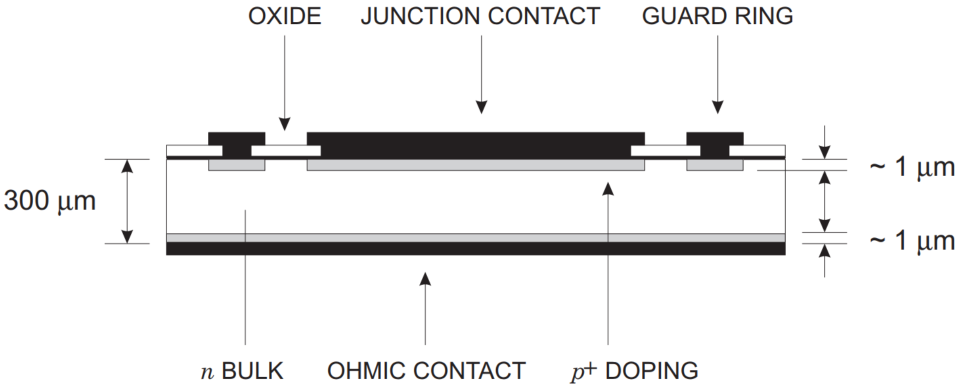

Figure 3.2: Cross-section of a typical semiconductor detector diode [18].

Semiconductor detectors can either be p- or n-doped. When p- and n-type semiconductors are connected, a pn-junction is formed. When a voltage is applied, positive on the n-side, and negative on the p-side (reverse bias), the electrons on the n-side and the holes on the p-side are drawn away from the junction. Electrons are drawn towards the positive terminal, and the holes are drawn against the negative terminal. This results in the region adjacent to the pn-junction is depleted of mobile charge and forms an insulator, and this is where the applied voltage builds up the desired electric field. In solids the absorbed energy must exceed the band-gap to form mobile charge carriers. In silicon the gap energy is 1.12 eV, so particles with greater energy can be detected. Similar doped regions on both sides of the diode indicate a guard ring, which surrounds the detector diode to isolate it from the edge of the wafer. This prevents large leakage currents, due to mechanical damage at the edges. In absence of an externally applied voltage, thermal diffusion forms a depletion region. Hence, every pn-junction starts off with a nonzero depletion width, and a potential difference between the n- and p-side, called the built-in potential.

To achieve a large a radiation-sensitive area, the depletion region should be as large as possible. This can be achieved by increasing the reverse-bias voltage. However, if the voltage is greater than a certain magnitude the structure of the crystals will break down. It is usually difficult to get an adequate depletion region in this type of detector. The common way of mitigating this is inserting an un-doped layer between the p- and n-side, called an intrinsic layer. This reduces the need for a large reverse-bias voltage as well.

3.1.2 Pixel Devices

To obtain two-dimensional information that is not open to more than one interpretation, the sensor must provide fine segmentation in both dimensions. This can be achieved either by geometrical or electronic segmentation. Silicon drift chambers, random access pixel devices and Charge Coupled Devices (CCDs) represents different approaches obtaining this unambiguous two-dimensional information. In the simplest implementation the sensor electrodes are patterned as a chessboard with accompanying readout electronics. In a high resolution pixel device the pixel size is often limited by the area required by each electronic readout cell, which depend on the complexity of the circuitry required for each pixel.

3.2 Radiation Effects

A primary concern for electronics in space is the radiation effects. In space, which is outside Earth's magnetic field, electronics can be damaged by the natural space radiation environment. Damage effects range from degradation in performance to complete functional failure. This will in turn result in reduced mission lifetimes and/or major system failures. The main source of radiation in Low Earth Orbit (LEO) comes from the trapped electron and protons in the inner radiation belt. Two basic radiation damage mechanisms affect semiconductor devices. Displacement damage, such as Single Event Effects (SEEs), and ionization damage, such as the Total Ionizing Dose (TID). However, shielding can be used effectively to mitigate these damage mechanisms.

SEE is an instantaneous failure mechanism, and is expressed in terms of a random failure rate. SEEs are divided into soft errors and hard errors. These failure mechanisms are caused when a single, high energy particle passes through the electronic device and deposits energy, which in turn liberates a charge in the circuit.

Ionization damage is time- and orbit-dependent. When a particle passes through a transistor it will generate electron-hole pairs in the thermal oxide. This collection of charge can create leakage currents, degrade the gain of the device, affect timing characteristics, and in some cases result in complete functional failure.

3.2.1 Soft Error

A soft error is defined as a non-recurring error that is triggered when a chip is irradiated. High energy neutrons (larger than 1 MeV) from cosmic radiation account for most soft errors in space. Soft errors can cause bit-flips, or changes in the state of memory cells or registers. It can cause latch-ups, which is formation of parasitic bipolar action in Complementary Metal–Oxide–Semiconductor (CMOS) wells, which induces a low impedance path between power and ground, which in turn produces a high current condition. Soft errors affect both combinational logic, registers and memories. To tolerate soft errors in memories, error detecting and correcting codes are used. With the use of these codes, soft errors rarely turn in to failures. To counteract soft errors, radiation-hardening can be employed. However, soft errors are a growing problem at 65 nm and below. The Soft Error Rate (SER) increases with altitude. Power cycling the device usually restores functionality.

3.2.2 Hard Error

A hard error causes an irreversible change in operation and is typically associated with permanent damage to devices or circuits. Such as, over-voltage failure, latch-up, oxide and interconnect wear-out. Power cycling does not restore functionality in a device permanently damages by hard errors.

3.3 Space Environment

Electronics in space environment bring, in addition to radiation damages, other challenges as well. These are for example; electrostatic discharge, heat dissipation, large temperature fluctuations, and outgassing.

3.3.1 Electrostatic Discharge

Electrostatic discharge occur when high levels of contamination accumulates on surfaces, as satellites are vulnerable to charging and discharging. This is the reason space applications require components with no floating metal. The degree of charging depend on the design of the system and the orbit. Charging is a variation in the electrostatic potential of the satellite, due to the low-density plasma surrounding the satellite. Plasma bombardment and photo electric effects are the main mechanisms responsible for this this charging. In GEO discharges as high as 20 kV has been observed. Electrostatic discharge can damage the devices if protective measures are not taken. The protective solution is to coat all the outside surfaces of the satellite with a conducting material. Atomic oxygen, which is found in the middle atmosphere, can react with organic materials on satellite exteriors and gradually damage them. As plastic is highly sensitive to atomic oxygen and ionizing radiation, coating is the solution here as well.

3.3.2 Temperature Control

A satellite will encounter very high temperature fluctuations. Satellites orbiting Earth switches between two phases, the sunlit and the eclipse phase. The Sun heats the satellite in the sunlit phase, as the satellite travels through the eclipse phase the satellite is cooled down. The temperature can change as much as 300°C between the two phases. This temperature fluctuation increases with increasing orbit altitude, as satellites travel closer to the Sun. The life expectancy of electronics can be degraded by prolonged periods of high temperature. There are three ways of transferring heat; convective, diffusive, and radiative. In space, there is no thermal convection or conduction taking place, therefore radiative heat transfer is the primary method of transferring heat in vacuum.

3.3.3 Outgassing

When plastic and glues outgas they release vapour, which can be a problem to optical devices. If vapour is deposited on the device, the performance is degraded. The solution is to use ceramics instead of plastic, as this eliminates the problem in electronics. In LEO outgassing of silicones can cause a cloud of contaminants around the satellite. External surfaces on the satellite is contaminated from not just outgassing, but venting, leaks, and thruster firing as well. They all may result in a degraded performance of the system.

CHAPTER 4

DEEP Instrument

This chapter gives an introduction to the proposed Distribution of Energetic Electron and Proton (DEEP) instrument. It will also give theoretical understanding to how the underlying electronics involved in the system work. The information in this chapter is based on [1], [18], and [22].

4.1 Overview

The primary scientific objective for the DEEP instrument is to accurately quantify energetic electron precipitation into the atmosphere. Electrons below 1 MeV deposits their energy in the middle atmosphere. The resulting ionization is of great importance for changing chemistry and dynamics of the atmosphere. To accurately quantify this effect a good estimate of the energy deposited in the atmosphere and how energy is distributed globally is required. The current particle detectors already in space have a design and/or orbit inadequate for determining the amount of particles precipitating into the atmosphere. In particular, the electrons often have a strong anisotropic pitch angle distribution which is not monitored by current detectors in space.

The DEEP project aims to design an electron instrument which will be able to achieve a field of view of 180°. Information collected by this instrument will help to determine the electron fluxes absorbed by the atmosphere, as well as fluxes backscattered from the atmosphere. Three detector houses with one proton detector each is also included in the design. It is mandatory to measure both electrons and protons as the protons to some extent contaminate the electron measurements, and by monitoring both electrons and protons the effect of contamination can be corrected. Information gathered by the DEEP instrument can help study other scientific objectives as well, such as:

Magnetospheric variability is caused by source and loss processes in the magnetosphere. Precise measurements of the angular and energy distribution of the electron and proton fluxes might help to reveal these sources and loss processes. The particle measurements will give information on the level of pitch angle diffusion and wave/particle interaction responsible for energizing and spreading the particles at different energies.

Microbursts at auroral latitudes, typically lasting less than one second, can be measured. To be able to measure this small scale feature, a sampling frequency of 20 measurements per second is required.

Solar Proton Events (SPEs) impacting polar regions is a major space weather phenomena which can cause hazardous effects in near Earth space environment. For example, severe radio absorption and communication blackouts. Although SPEs are infrequent, its contribution on space weather is of interest.

Energetic Neutral Atoms (ENAs) can be detected by the proton sensor near equator. Measurements of ENAs will give information about the loss processes and level of symmetry on Earth's ring current.

4.2 Sensor

The sensor is made from silicon, a solid-state semiconducting material. The basics of a semiconducting sensor is described in section 3.1.1. The sensors can be seen as pad detectors, and will be stacked together to form a unit. The thickness of both the front and the back layer of the electron sensor is 1 mm. The proton sensor has the same thickness in the back layer as the electron sensor, but the thickness of the front layer is 0.3 mm. By having a 0.3 mm front layer, high energetic electrons can be filtered out, as they will only deposit their energy in the back layer. A thick front layer would result in a mix of particles, and make it hard to distinguish them. The design is inspired by [23]. The silicon in both sensors are totally depleted.

4.3 Detector House

The detector house consists of Wolfram (W) and Aluminium (Al). These materials are chosen to prevent electrons of energies less than 6 MeV to penetrate the detector house, as well as protons of energies less than 45 MeV. The pinhole is where the particles can easily penetrate the detector house. Essentially the pinhole controls the flux of particles. The front surface of the detector is covered with a 20 µg/cm^2 thick aluminium film to prevent photons from entering, as well as providing electrical contact. Baffles prevent incoming particles from scattering off the walls and into the sensor. The baffles usually incorporate knife-edges to decrease the number of particles reflecting off the baffle edge and into the detector. Particles that hit the silicon will be absorbed, and electrical current is generated in the sensor. Figure 4.1 show 3D-model of the detector house.

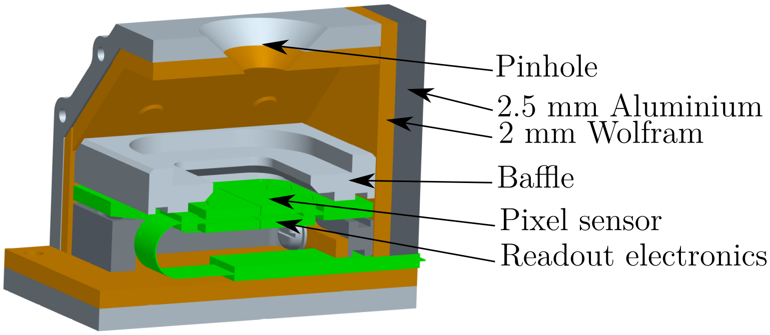

Figure 4.1: 3D-model of the detector house [24].

4.4 Electron Detector System

The Electron Detector System (EDS) will detect electrons with energies in the range 30 keV to 2 MeV. The system consists of two layers, each with 2×4 pixels. The pixel arrangement is illustrated in figure 4.2. The pinhole of the detector house is covered by 0.76 µm Nickel (Ni) foil. The foils purpose is to reduce light sensitivity, and to stop low energy protons from entering the detector. At this stage there are no way to determine the type of the incoming particle. Both electrons and protons will deposit enough energy in the detectors to generate a signal.

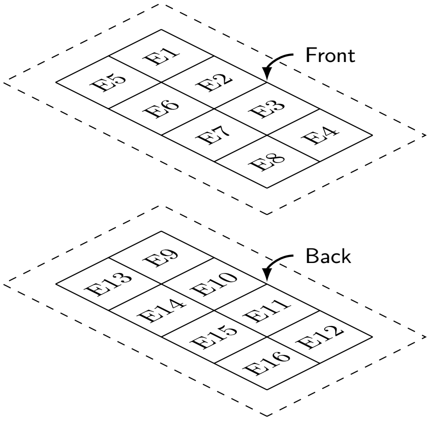

Figure 4.2: Illustration of electron pixel arrangement.

4.5 Proton Detector System

The Proton Detector System (PDS) will detect protons with energies in the range of 30 keV to 10 MeV. The system consists of two layers, each with 2×2 pixels. The pixel arrangement is illustrated in figure 4.3. To prevent electrons with energies less than 1 MeV from entering the detector, a magnetic field of 0.2 Tesla is applied. From the PDS the signal is fed into the front-end electronics. Little focus has been dedicated to this system yet.

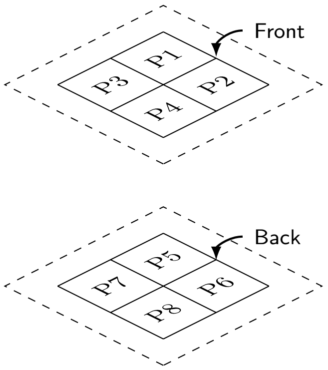

Figure 4.3: Illustration of proton pixel arrangement.

4.6 Front-end Electronics

The front-end electronics consist of an Application-Specific Integrated Circuit (ASIC) and an Analog-to-Digital Converter (ADC). The ASIC's purpose is to amplify and shape the signal before it is digitized in the ADC. Figure 4.4 illustrates the readout chain for the front-end electronics.

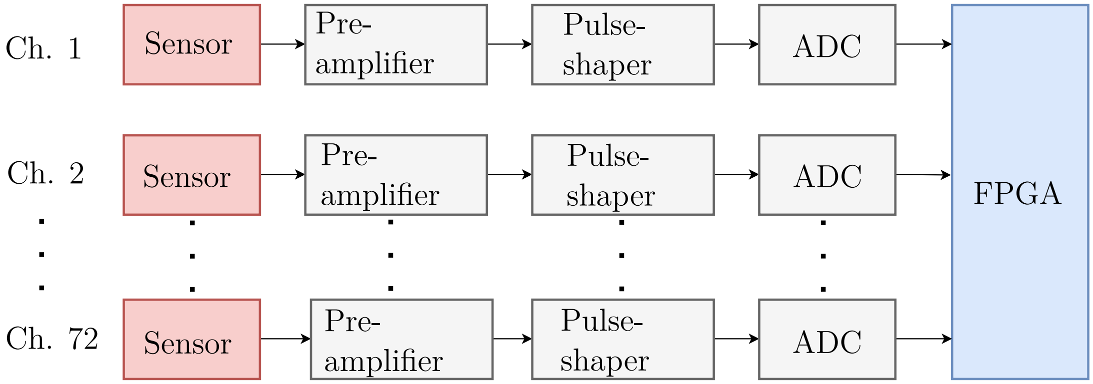

Figure 4.4: Conceptual overview of the readout chain for the front-end electronics.

4.6.1 ASIC – Pre-Amplifier and Pulse-Shaper

The ASIC will integrate two tasks; pre-amplifying and shaping of the signal pulse. Signal charge from the sensor can be quite small, in the order of femtocoloumbs. This means that the sensor signal must be amplified. The magnitude of the signal is open to statistical fluctuations and electronic noise, hence the pre-amplifier must be designed with a focus to minimize electronic noise.

The pre-amplifier is configured as an integrator. The purpose is to convert the current pulse from the sensor into a step impulse with a long decay time. A pulse processor transforms a short sensor current to a broader pulse with a peaking time, T_p, as illustrated in figure 4.5.

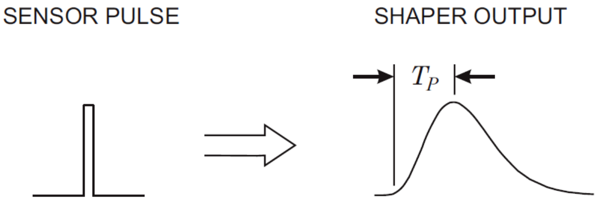

Figure 4.5: Conceptual functionality of a pre-amplifier [18].

The primary function of the pulse-shaper is to improve the Signal-to-Noise Ratio (SNR), as the electrical noise relies critically on this stage. A functional pulse-shaping system is illustrated in figure 4.6. A high-pass filter contributes to set the desired decay time, while a low-pass filter limits the bandwidth and sets the rise time. The sensor capacitance and input capacitance of the amplifier are important parameters, as the SNR increases with decreasing capacitance.

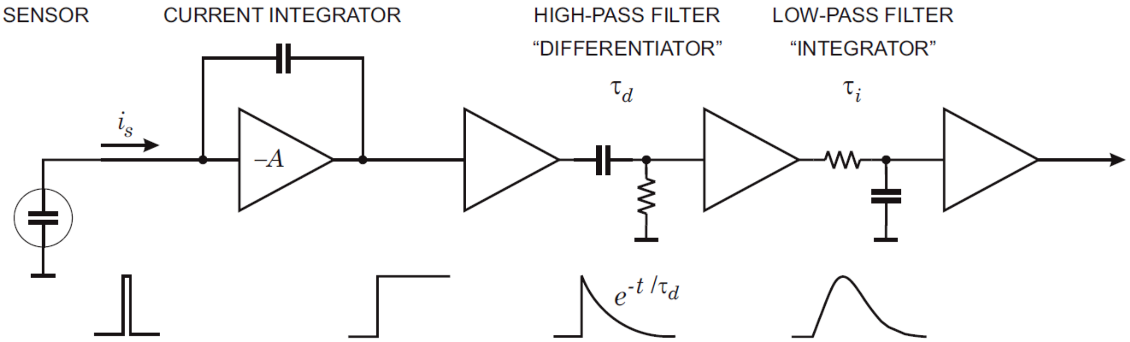

Figure 4.6: Conceptual functionality of a pulse-shaper [18].

By applying a filter that favour the signal, while attenuating the noise, the SNR can be improved. Improving the SNR usually implies reducing the bandwidth, but reducing the bandwidth increases the duration of the pulse. The shaper must handle many pulses at a very high rate. Successive pulses with too large pulse width will lead to pile-up. This happens when another particle hits the detector before the voltage of the previous has returned to the baseline voltage. This is illustrated in figure 4.7.

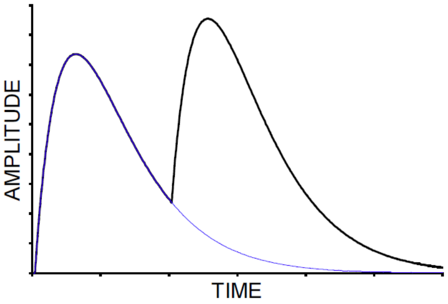

Figure 4.7: Tail pile-up occurs when two pulses overlap and reducing the shaping time allows the first pulse to return to the baseline before the second pulse arrives [18].

When designing a system, it is necessary to find a balance between the conflicting requirements of reducing noise and increasing speed. Usually a compromise between the two must be found. The DEEP system should be able to handle microbursts. The pulse-shaper must be compatible with the next step in the signal line as well. Pile-up will cause erroneous result for the second pulse, thus representing a combination of multiple particle energies. By reducing the pulse width pile-up can be counteracted. Table 4.1 lists the probability of having pile up associated with different count rates and shaping times for 30 keV electrons. To avoid pile-up in the DEEP instrument the shaping time has to be less than of 0.5 µs.

Time [µs]	Count Rate [counts/s]	1×10^5	2×10^5	1×10^5	1×10^6
0.5		0.049	0.095	0.222	0.393
1.0		0.095	0.181	0.393	0.632
2.0		0.182	0.330	0.632	0.865
3.0		0.259	0.451	0.777	0.950
4.0		0.330	0.551	0.865	0.982
5.0		0.393	0.632	0.918	0.993

Table 4.1: Tail pile-up probability related with different shaping time and count rates.

4.6.2 Analog-to-Digital Converter

The purpose of the the ADC is to continuously translate the varying signal amplitude to discrete steps, each corresponding to a unique output bit pattern. At the time of writing several techniques are considered, such as oversampling, peak-hold, and Time Over Threshold (TOT). So far, the TOT technique is considered the most promising. The TOT technique has several advantages over direct pulse height analysis. The simplicity of the conversion circuit leads to lower power consumption. The TOT technique is well suited for multi-channel readout systems with pixelated design [25]. However, the TOT technique have some limitations. For example, the non-linear relation between the input charge and the width of the encoded pulse. Dynamic limitation can also be an issue, but recent studies has shown promising results in that regard [26].

4.7 Back-end Electronics Introduction

The back-end electronics consist of a digital signal processor. The digital signal processing of the information gathered by the sensors will be processed in an FPGA. The processing needed is a coincidence check, data binning, and data packet. Figure 4.8 illustrates the readout chain for the back-end electronics. Suitable FPGAs for the DEEP instrument are also discussed.

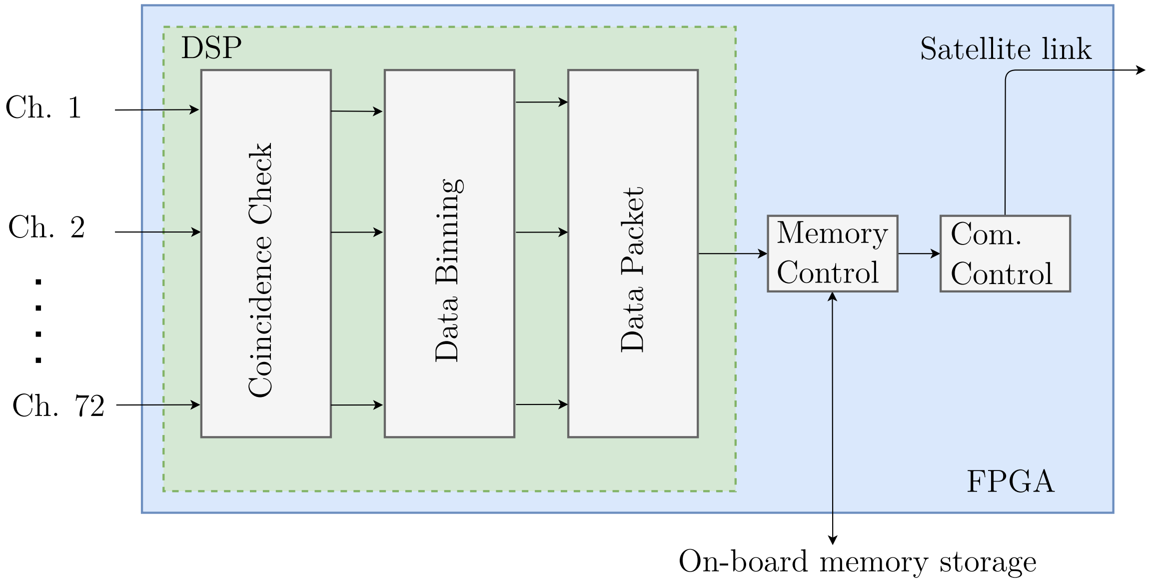

Figure 4.8: Conceptual overview of the readout chain for the back-end electronics.

4.7.1 Field-Programmable Gate Array

Modern FPGAs have millions of logic gates and Input/Outputs (I/Os) can operate at over 10 GHz. They can have embedded microprocessor cores and DSP accelerator hardware. It is the best choice for low- to medium-volume custom logic applications, due to the low up-front cost and ease of correcting design errors. However, for space application, the performance is limited. Logic gates will be in the order of tens/hundred thousands, and I/O performance of hundred MHz. Regardless, FPGAs are still an excellent option for the DEEP project.

Space is an incredibly challenging environment for electronics and radiation is the main concern. Static Random-Access Memory (SRAM) based FPGAs are especially vulnerable to damage, since they are big memory devices. The most frequent fault caused by radiation is bit-flipping in memory elements and the configuration logic itself is vulnerable, not just the data stored. Steps can be taken to mitigate this, usually Triple-Module-Redundancy (TMR) is implemented on memory elements and combined with scrubbing, the effects of radiation is mitigated.

An alternative FPGA solution is the Microsemi antifuse technology specifically designed for space application. Suited for the DEEP project tasks, one FPGA positioned itself as the best candidate, the Microsemi RTG4. It is a radiation tolerant FPGA for signal processing applications. Space-grade electronics are expensive, but Microsemi offers a commercial-grade equivalent FPGA for lab use. This results in affordable lab testing. If the space-grade FPGA is too expensive, a military-grade FPGA can be considered. Best choice would be the Microsemi SmartFusion2. Specifications of the two FPGAs are listed in table 4.2, from [27] and [28].

Peripherals	RTG4	SmartFusion2
Logic Clusters	151,824	144,124
DSP/Mathblocks	462	240
PLLs	8	8
Total RAM [Mbits]	5.2	4.448
Total User I/Os	720/166	574
High Speed Interface	16	24
Grade	Space	Military

Table 4.2: Microsemi RTG4 and SmartFusion2 FPGA specifications compared.

CHAPTER 5

GATE Simulation Setup

Simulations provide an important method of analysis which is easily verified. Additionally it enables experimentation on a digital representation of a system. Simulation software provides a dynamic environment for the analysis, in addition, the possibility to view them in two- or three-dimensions while they are running. Electron scattering, out of a pixel, result in reduced angular resolution of the EDS, and the correlation between the energy and the degree of scattering is crucial information when designing the coincidence check function. To determine to which degree electrons scatter at different energies a GEANT4 Application for Emission Tomography (GATE) simulation is useful. GATE is a Monte Carlo simulation platform developed by the OpenGATE collaboration. A GATE simulation might give information about the limitations of electron detector system. In this chapter, an explanation of the GATE simulation designed for the DEEP instrument is given and the necessary simulation parameters are discussed. Results from the DEEP simulation setups are given in chapter 6. Detailed introduction to GATE simulations and explanation on how to install and set up a simulation are described in appendix A. Every simulation setup is documented in the gate_simulation repository and information about this repository can be found in appendix D.

5.1 Simulation Setup

For the simulation model a new pixelated geometry was designed. Its purpose is to cover most scenarios of the DEEP instrument with one simulation, a smart geometry. That is why each silicon layer will consist of 3×3 pixels instead of 2×4 pixels, as illustrated in 5.1. With a symmetrical geometry and an electron beam pointing to the middle pixel, a symmetrical scattering to nearby pixels is expected. This geometry will make the validation of the results less challenging, as it is the level of scattering that will be investigated. The geometry will provide necessary information to determine if the scattering of the electrons cause problems, even though the pixel setup deviates from the DEEP detector.

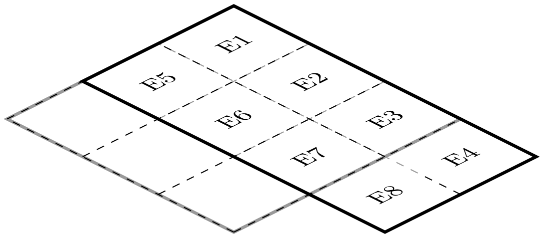

Figure 5.1: Illustration of how the simulation setup 3×3 pixel design overlap of the DEEP instrument 2×4 pixel design.

A total of ten simulation geometries were designed, where seven of those are distinct DEEP relevant geometries. The first one can be considered as proof of concept, as it uses a simple geometry and a source with parallel monoenergetic electron beam. The second is similar to the first, but with a detector house (DH) added. In this simulation the degree of backscattering from the detector house will be investigated. In the third setup the geometry is the same as the first setup, but now the source is a point source, instead of a parallel beam. This means that the electrons hit the detector with different angles, and the effect of this is investigated. The fourth simulation setup is similar to the third, but with a detector house added. The simulation setup *Wide* is nearly identical to simulation setup four, but with a wider beam. The simulation setup *mask* introduced a mask attached to the front layer and used to observe the reduction effect on scattering to nearby pixels. By continuously creating new separate geometries when introducing new geometry or altering the parameters of the source it is possible to examine the impact of each alteration. The DEEP simulation setups are discussed in detail in section 5.4. Table 5.1 shows an overview of the different geometry configurations for the simulation setups.

Simulation	Parallel Beam	Point Source	Wide Beam	DH	Mask
Setup 1	yes	no	no	no	no
Setup 2	yes	no	no	yes	no
Setup 3	no	yes	no	no	no
Setup 4	no	yes	no	yes	no
Wide	no	yes	yes	yes	no
Mask	yes	no	no	yes	yes

Table 5.1: Overview of the geometry configurations for the simulation setups.

5.1.1 Detector Model

The detector model is, as the actual instrument, made up by two layers. The elements of both the front and the back layer are silicon and these layers represent the detector. The dimensions of the layers are 15×15×1 mm. The layers are separated by 0.4 mm vacuum. The front layer is closest to the source. Figure 5.2 illustrates the foundation of all GATE simulation geometries. Each layer consists of 3×3 pixels. The front layer is illustrated as the blue layer, and the back layer is not drawn. The particle source (pink square) is located between 16.4-19.5 mm in the Z-axis, depending on the simulation setup. The grey lines illustrate the world in which the simulation is performed, and only interactions inside the world is documented. The front and the back layer pixels are not pixelated in the detector model as the illustration suggests, but will be created in the readout phase of the simulation, discussed in section 5.5.

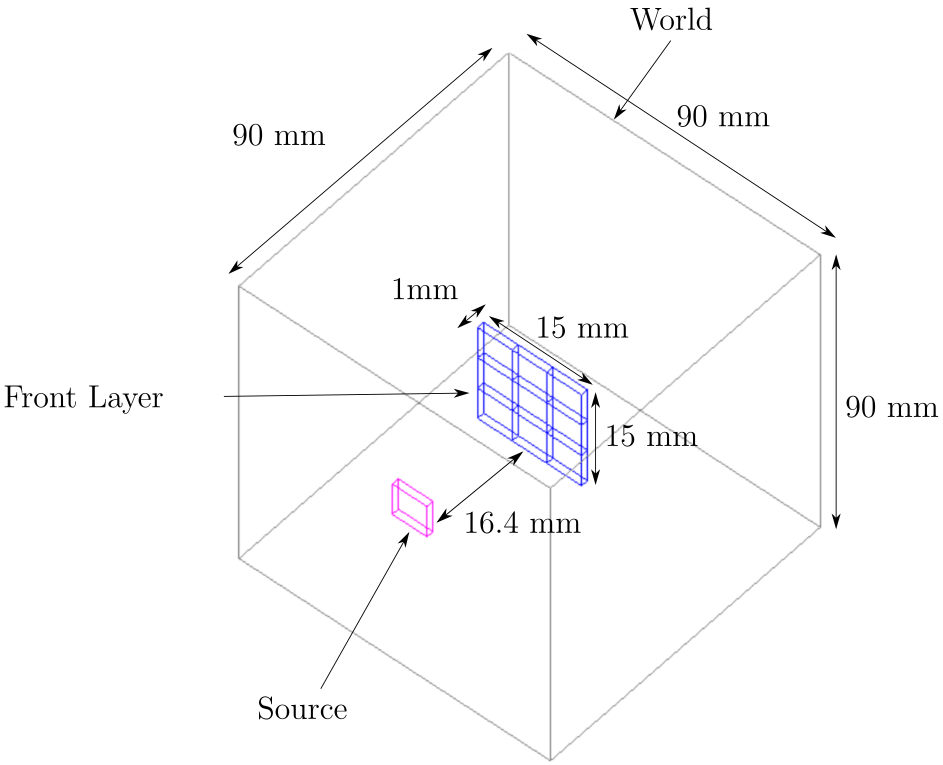

Figure 5.2: The foundation of the GATE simulation geometry.

5.1.2 Pixel Arrangement

Figure 5.3 shows the pixel arrangement in the front and the back layer. Pixel 5 is the middle pixel on the front layer, and pixel 14 is the middle pixel in the back layer.

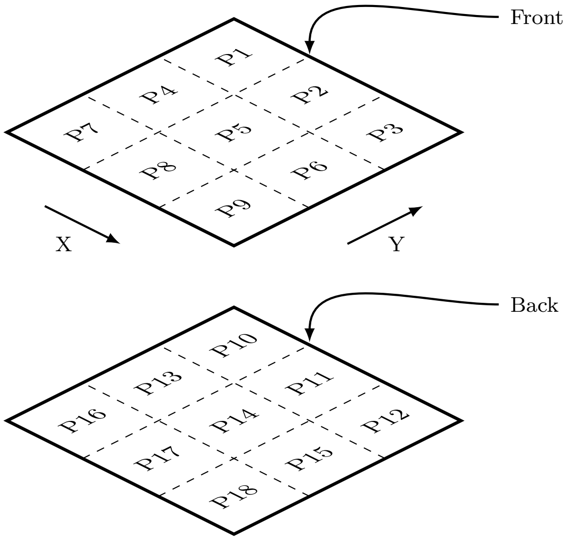

Figure 5.3: Illustration of how the pixels are arranged.

5.2 Physics List Validation

GATE uses the GEometry ANd Tracking 4 (GEANT4) models for physics processes. In GEANT4, a wide choice of physics processes and models are available, each with different detail and accuracy. The physics list used in the DEEP geometry simulations will be weighted between the level of details of the physics models. Since GEANT4 provides tens of models, the first task is to find the most relevant ones. The best candidates will be compared and then validated. Assume a physics list is made for a distinct application and the user changes parameters such as energy, primary particles and/or material, the outcome may be inaccurate simulation results for our purpose. Based on thorough study, two potential candidates were found. The emstandard_opt4 and the emstandardSS list. These lists will be compared regarding how much scattering, to nearby pixels, each electron has, size of the output file and computation time. Nevertheless, the most important aspect is to check if there is any major difference between the two lists regarding the scattering to nearby pixels. For the different available physics lists in GEANT4 10.04, see [29].

The emstandard_opt4 is designed for any application that require higher accuracy of electrons, hadrons and ion tracking. The emstandard_opt4 uses the most accurate standard and low-energy models and is used in extended electromagnetic examples. For the emstandardSS, the SS is an abbreviation for Single Scattering, and the list is used for validation of single scattering models, such as the one in emstandard_opt4. For electrons, the emstandardSS uses the most accurate algorithm regarding single scattering in vicinity of a geometry boundary. Based on this it is presumed that the emstandardSS is the most accurate list.

5.2.1 Validation Setup

Figure 5.4 shows the setup for the simulation. The red colour illustrates where the electron beam hits the front layer. Beaming the electrons in a narrow strip at the edge of the middle pixel maximizes the electron scattering rate, as well as minimizing the output files. The random engine seed is set to the same value when comparing the two physics list, which means that the seed is set to manual. The seed must be an unsigned integer value and it is recommended to be included in the interval [0,900000000]. As a manual seed value had to be set, the random engine seed 9000 was chosen.

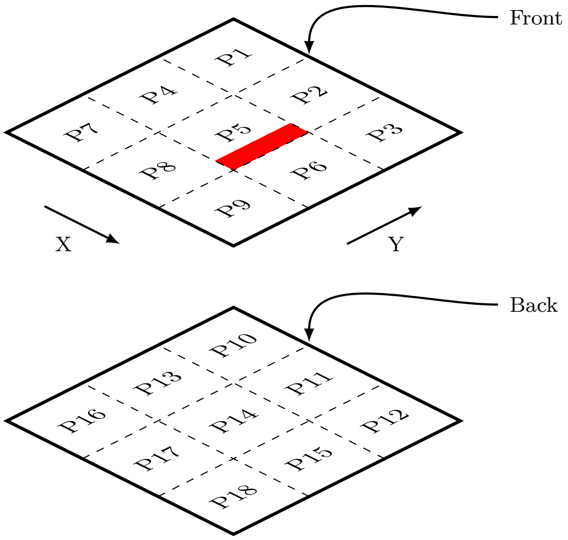

Figure 5.4: Hit pattern on the front layer, illustrated in red, from the source used in physics list validation setup.

5.2.2 Validation Results

Table 5.2 and 5.3 show how the size of the output file and computation time increases with increasing number of particles. The tables shows an average of how many scatterings (SCT) each electron has. With an electron energy equal to 480 keV the emstandard_opt4 averages around 23 scatterings per electron, while the emstandardSS averages around 4832 scatterings. It explains why the two lists are different regarding the size of the output file and the computation time of the simulation. The emstandard_opt4 implies increased computation time, but it is still quite manageable. The emstandardSS implies an enormous increase in simulation time for each step. Both physics list generates nearly double the output data for each doubling in simulated particles. It is almost a linear increase. Observing the tables, it is clear that there are huge differences between the two lists. The output file size for the emdstandardSS with 1×10^4 particles is 3.8 GB. For the same particle amount the emstandard_opt4 has an output file size of 18.7 MB.

Particles	Scattering/e$^-$	Output File Size	Computation Time
1×10^2	23.1	208.1 kB	6.7 sec
1×10^3	23.6	1.9 MB	9.5 sec
1×10^4	23.6	18.7 MB	38.5 sec

Table 5.2: Simulation of electrons with energy equal to 480 keV, with emstandard_opt4 physics list.

Particles	Scattering/e$^-$	Output File Size	Computation Time
1×10^2	4787	36.4 MB	44 sec
1×10^3	4851	374 MB	27 min
1×10^4	4858	3.8 GB	39 hours

Table 5.3: Simulation of electrons with energy equal to 480 keV, with emstandardSS physics list.

Based on the results in table 5.2 and 5.3, simulating 1×10^5 or even 1×10^6 particles with the emstandard_opt4 physics list is achievable within reasonable time, as well as it will generate a manageable output file size, compared to the emstandardSS. Using the emstandardSS would lead to very long computation time, and with only 1×10^4 particles the size of 3.8 GB could already cause problems on different systems.

Table 5.4 shows the two lists compared to each other with aspect to scattering and energy absorption. Both physics lists give similar results. Energy absorption for each layer, total absorbed energy and total absorption are the same for the two lists.

There are some differences between the two lists regarding the amount of scattered particles and the scattered energy. The emstandard_opt4 scatter 6.45 % more energy, while it scatters 5.94 % less particles than the emstandardSS.

	emstandard_opt4	emstandardSS	Difference	Difference [%]
Total SCT	1769	1891	122	6.45
Total SCT E	456.5 MeV	430.9 MeV	25.6 MeV	5.94
Absorption f-layer	4446.6 MeV	4472.1 MeV	25.5 MeV	0.57
Absorption b-layer	776.8 keV	692.1 keV	84.7 keV	0.12
Total absorbed E	4452.5 MeV	4477.5 MeV	25 MeV	0.56
Total Absorption	0.851	0.857	0.006	0.70

Table 5.4: Simulation of electrons with energy equal to 480 keV for both physics list compared to each other.

Table 5.5 and 5.6 show detailed information regarding scattering to the nearby pixels. As mentioned, both physics lists give similar results. For simplicity total absorbed energy is abbreviated TAE.

Pixel	SCT	TAE [keV]	E/e$^-$ [keV]
P1	0	0	0
P2	244	63211.52	259.1
P3	34	7245.78	213.1
P4	0	0	0
P5	N/A	3996025	399.6
P6	1192	314906	264.2
P7	0	0	0
P8	248	65171.73	262.8
P9	24	5160.98	215.0
P10	0	0	0
P11	5	115.26	23.1
P12	1	19.97	20.0
P13	0	0	0
P14	13	296.05	22.8
P15	4	94.52	23.6
P16	0	0	0
P17	1	26.26	26.3
P18	3	224.7	74.9

Table 5.5: 480 keV electrons, with the emstandard_opt4 physics list.

Pixel	SCT	TAE [keV]	E/e$^-$ [keV]
P1	0	0	0
P2	248	54621.82	220.3
P3	22	4121.93	187.4
P4	2	78.50	39.3
P5	N/A	4046580	404.7
P6	1306	307598	235.5
P7	0	0	0
P8	258	59098.67	229.1
P9	27	4703.71	174.2
P10	1	4.17	4.2
P11	2	62.97	31.5
P12	0	0	0
P13	0	0	0
P14	11	220.72	20.1
P15	8	157.76	19.7
P16	0	0	0
P17	3	89.00	29.7
P18	3	157.46	52.5

Table 5.6: 480 keV electrons, with the emstandardSS physics list.

Figure 5.5 and 5.6 show the total energy distribution in pixel 5, and the energy distribution is nearly identical. The emstandardSS has 122 more scatterings, while the scattered energy is 25.6 MeV larger on the emstandard_opt4.

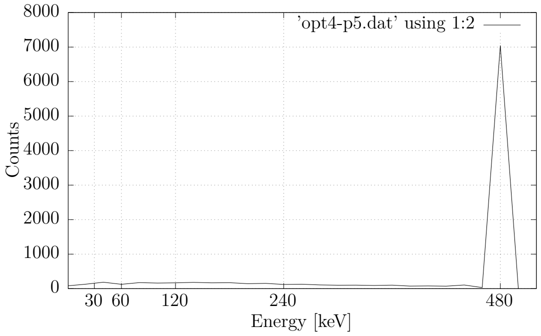

Figure 5.5: Energy distribution in pixel 5 with the emstandard_opt4 physics list for electrons with 480 keV.

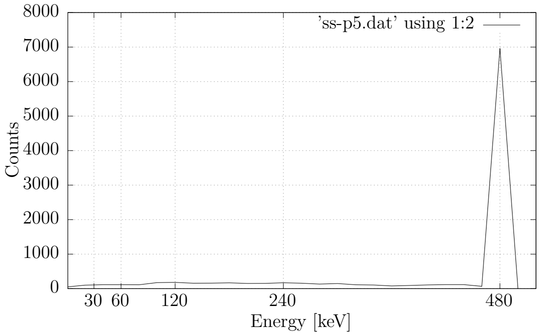

Figure 5.6: Energy distribution in pixel 5 with the emstandardSS physics list for electrons with 480 keV

Figure 5.7 and 5.8 show the energy distribution in pixel 6 for both lists. The lists has dissimilarities, especially at energies below 30 keV. The emstandard_opt4 appear to track particles until a certain threshold, and then accumulating the rest of the energy in that point. The emdstandardSS appear to track particles until no more energy is left, without any accumulation of energy below a certain threshold.

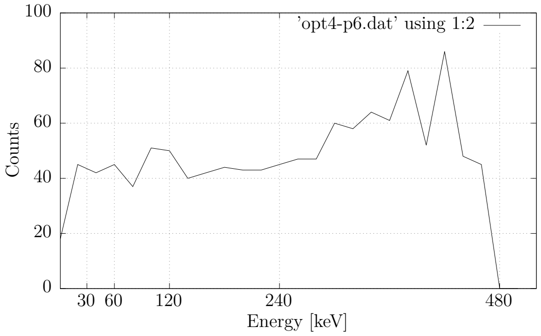

Figure 5.7: Energy distribution in pixel 6 with the emstandard_opt4 physics list for electrons with 480 keV.

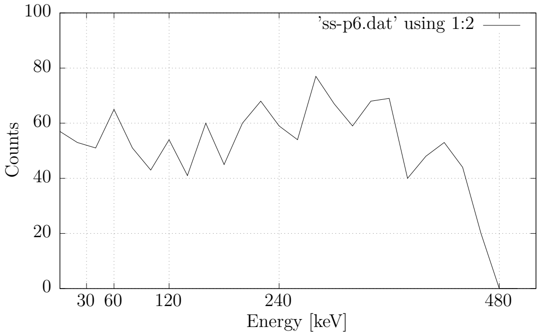

Figure 5.8: Energy distribution in pixel 6 with the emstandardSS physics list for electrons with 480 keV.

Figure 5.9 and 5.10 illustrate scattering to the nearby pixels. Figure 5.11 and 5.12 illustrate the total energy distribution in percentage.

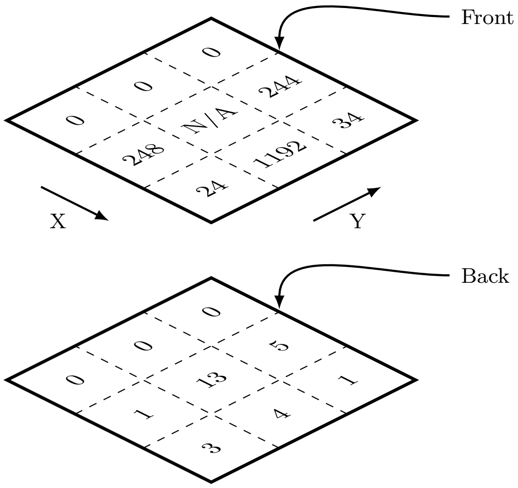

Figure 5.9: Total scattering in each pixel with the emstandard_opt4 physics list for 480 keV electrons.

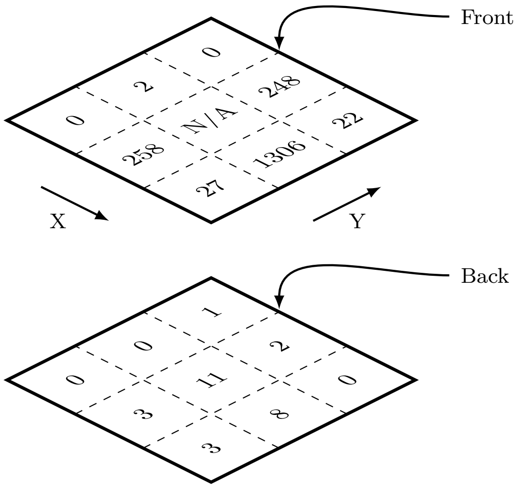

Figure 5.10: Total scattering in each pixel with the emstandardSS physics list for 480 keV electrons.

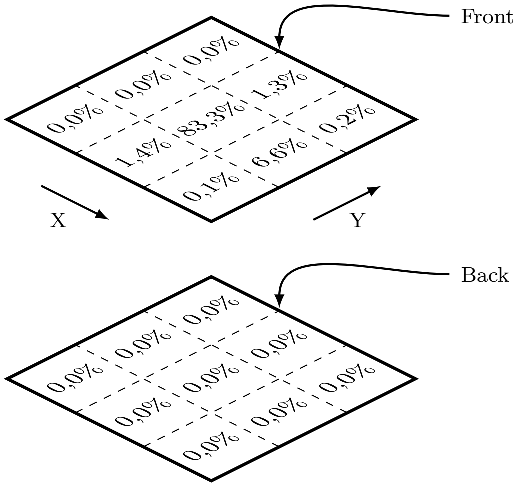

Figure 5.11: Total energy distribution in percentage with the emstandard_opt4 physics list for 480 keV electrons.

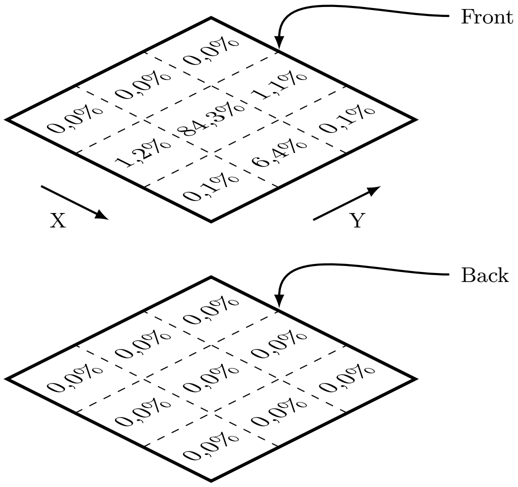

Figure 5.12: Total energy distribution in percentage with the emstandardSS physics list for 480 keV electrons.

Based on the results presented, the emstandard_opt4 appear to be the best option. Both physics lists seem to provide adequate results. In regards to computation time and size of the output file the emstandard_opt4 is superior. Some differences were observed at energies below 30 keV. However, this is not seen as problem as the front-end electronics is not able to distinguish particles from noise at 30 keV and lower. Based on these factors the emstandard_opt4 physics list is considered the best option for the simulations.

5.3 Evaluation of the emstandard_opt4

To verify that the emstandard_opt4 gives accurate results in-depth analysis must be performed. Total absorption and range simulation will provide adequate information regarding the accuracy of the emstandard_opt4. For the range simulations a total of 1×10^5 protons and electrons were used. For the total absorption simulation a total of 2.5×10^4 electrons were used.

5.3.1 Deposition Range of Electrons and Protons

The first method for validating the simulation is the particle deposition range. The simulated range for both electrons and protons is compared to the calculated range, which is provided by National Institute of Standards and Technology (NIST). NIST provides the web database *ESTAR* for electrons and the web database *PSTAR* for protons. The databases include calculation on stopping-power and range tables for electrons and protons in any user-specified material. From the range tables the CSDA range is given, and from that value the final range can calculated. The density of silicon is 2.33 g/cm^3. The range in mm of a particle can be given as

$$range[mm] = \frac{CSDA[g/cm^2]}{Density[g/cm^3]}.$$

For both proton and electrons two separate energies is used and the corresponding range been calculated. The results can be seen in table 5.7, as well as the simulated ranges. The CSDA and the projected range in table 5.7 are obtained from the web databases *ESTAR* [30] and *PSTAR* [31]. For electrons there is no projected range to compare with, however, observing that the simulated projected range (Sim. R) is less than the calculated CSDA range (Calc. R) is indicative of a reasonable result. For protons the projected range is directly comparable. For 5 MeV protons the range calculation indicate the same range as the simulated. For 10 MeV protons the simulated suggest a larger range compared to the calculated projected range. The emstandard_opt4 provides satisfactory results regarding range for protons below 10 MeV and electrons below 1 MeV.

Part.	E [MeV]	CSDA [g/cm^2]	Proj. [g/cm^2]	Calc. R [mm]	Sim. R [mm]
e^-	0.5	0.220	N/A	0.944	0.7 ± 0.1
e^-	1	0.539	N/A	2.313	2.1 ± 0.1
p	5	0.050	0.050	0.215	0.215 ± 0.01
p	10	0.167	0.166	0.712	0.730 ± 0.01

Table 5.7: Calculated and simulated range for electrons and protons in silicon.

5.3.2 Total Absorption of Electrons

The second method for validating the simulation is the total absorption. Simulated total absorbed energy for electrons is compared to calculated probability of total absorption calculated by National Bureau of Standards (NBS) [32]. The simulated results can be observed in table 5.8. The table layout has the same layout as the table from NBS. Total absorption for energies below 150 keV are new results provided by the GATE simulations. The simulated values have a margin of error equal to ± 0.01. There is good correspondence between the simulated and the calculated values, with one percent point difference at most. This is within the margin of error.

E [keV]	z [mm]	0.01	0.03	0.1	0.2	0.3	0.5	1.0	2.0
30		0.86	0.86	0.86	0.86	0.86	0.86	0.86	0.86
60			0.86	0.86	0.86	0.86	0.86	0.86	0.86
100				0.86	0.86	0.86	0.86	0.86	0.86
150					0.86	0.86	0.86	0.86	0.86
200						0.86	0.86	0.86	0.86
250						0.85	0.85	0.85	0.85
300							0.85	0.85	0.85
400								0.86	0.86
500								0.85	0.86
600								0.84	0.85
800								0.60	0.85
1000								0.34	0.83
1500								0.06	0.47
2000								0.01	0.19

Table 5.8: Simulated probability of total absorption as a function of electron energy and the detector thickness.

In general, results obtained by utilizing the emstandard_opt4 is indicative of a reasonable result. The emstandard_opt4 appear as an adequate option to determine if electron scattering cause problems when evaluating the readout. As mentioned, the emstandard_opt4 appear to be the best option compared to the emstandardSS in terms of computation time and size of the output file. This is why the emstandard_opt4 will used for the DEEP simulation setups. Hence, further validation of the emstandardSS is not performed.

5.4 DEEP Simulation Setup

For the DEEP simulations some general setup parameters was determined and utilized for all simulations. The physics list emstandard_opt4 was chosen for the simulations, as it provided adequate information while being considerable faster and the file size quite small compared to the emstandardSS. ROOT is chosen as the output format of the simulation, as it is the best choice to compensate for the slow write to disk speed in GATE. In essence the choice is between a binary file (ROOT) and a text file (ASCII). In ROOT all other trees except *Hits* are disabled to further reduce the file size. The simulation needs a random engine, and Mersenne Twister is chosen. Mersenne Twister is both more recent and a better pseudo-random number generator than the 28-year-old James Random algorithm. Mersenne Twister has better statistical properties, in addition as being much faster. Table 5.9, which is the same as table 5.1, shows an overview of the different geometry configurations for the simulation setups.

Simulation	Parallel Beam	Point Source	Wide Beam	DH	Mask
Setup 1	yes	no	no	no	no
Setup 2	yes	no	no	yes	no
Setup 3	no	yes	no	no	no
Setup 4	no	yes	no	yes	no
Wide	no	yes	yes	yes	no
Mask	yes	no	no	yes	yes

Table 5.9: Overview of the geometry configurations for the simulation setups.

5.4.1 Simulation Setup 1

This is the first DEEP simulation setup, visualized in figure 5.13. The front and the back layer are the two blue layers, where the front layer is closest to the source (pink square). The grey plane located inside the front layer illustrates where the beam from the source hits the front layer of the detector. The source is defined as a uniform monoenergetic electron beam and will emit a beam parallel to the detector. It is located -19.5 mm from the origin. The origin is in the centre between the two layers. The distribution of the beam is unidirectional pointing to the middle pixel of the detector, in other words a parallel beam. The purpose is to investigate scattering in a controllable environment. In the physics list validation simulations, in chapter 5.2, it was uncovered that electrons scatter out of the middle pixel to some degree at 480 keV. In simulation setup 1 a wider range of energies are simulated. Backscattered electrons is not documented with this setup. Simulation results can be found in chapter 6.1.

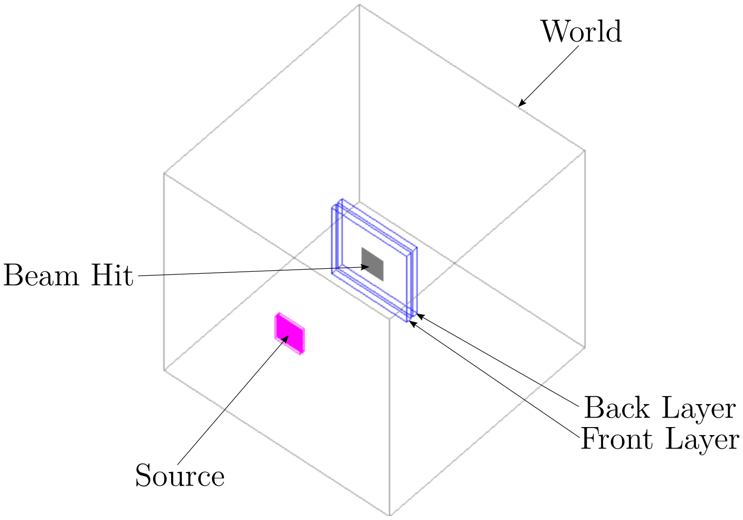

Figure 5.13: Visualization of the simulation setup 1. The front layer is closest to the source. The source emits a parallel beam of electrons onto the front layer. The beam hits the front layer as illustrated as the grey plane.

5.4.2 Simulation Setup 2

This is the second DEEP simulation setup, and it is a continuation of simulation setup 1. In simulation setup 2 a detector house is added, as illustrated in figure 5.14. In this simulation the effect from backscattering within the detector house is investigated. The geometry of the layers and parameters of the source are the same as in simulation setup 1, with one exception, the source is located -16.4 mm from origin. The source had to be moved closer to the front layer due to the detector house dimensions. The detector house is constructed so that it resembles the proposed detector house for the DEEP instrument. The detector house consist of two layers, where the outer layer is 2.5 mm thick aluminium, and the inner layer is 2 mm thick wolfram. The exterior dimensions of the outer layer is 40×40×32 mm, and the inner layer 35×35×27 mm. Simulation results can be found in chapter 6.2.

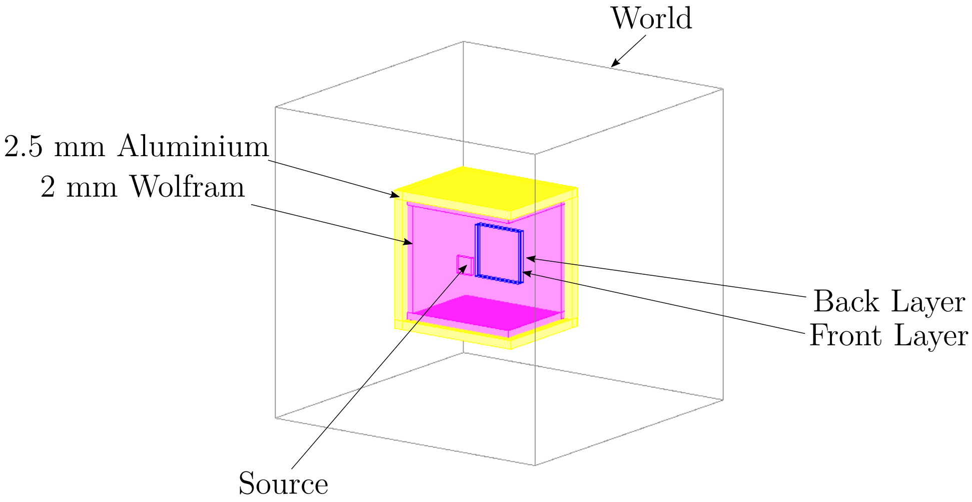

Figure 5.14: Visualization of the detector house added in simulation setup 2.

5.4.3 Simulation Setup 3

This is the third DEEP simulation setup, and it is a continuation of simulation setup 1. In simulation setup 3 the parameters of the source are adjusted. Instead of a parallel beam, the source is now a point source. This implies that electrons will hit the detector with different angles, and the degree of this effect is investigated. The maximum angle electrons can hit the detector is 13.2°. Figure 5.15 illustrates the hit pattern (red circle) on the front layer. Simulation results can be found in chapter 6.3.

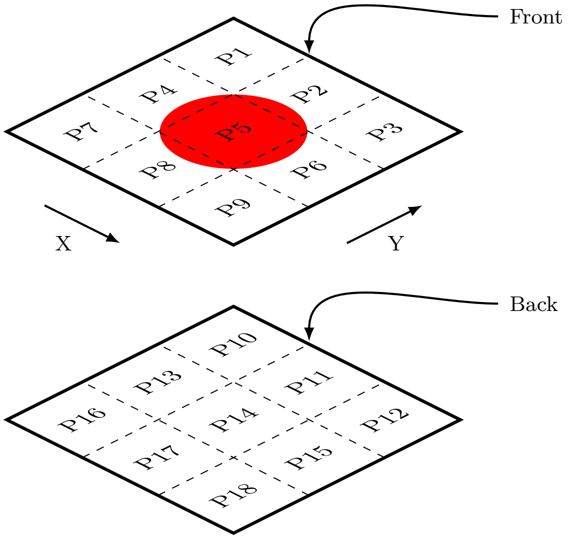

Figure 5.15: Illustration of the hit pattern (red circle) on the front layer from the point source used in simulation setup 3 and 4.

5.4.4 Simulation Setup 4

This is the fourth DEEP simulation setup, and it is a continuation of simulation setup 2 and 3. The simulation is illustrated in figure 5.16. The point source designed in simulation setup 3 is applied, in addition to the detector house designed in simulation setup 2. The effect of backscattering in the detector house with a point source is investigated. The point source has a full angle of 26.4°. This indicates the maximum angle the electrons can hit the detector is 13.2°. Which is the same maximum angle as in simulation setup 3. The detector house has the same dimensions as in simulation setup 2. Simulation results can be found in chapter 6.4.

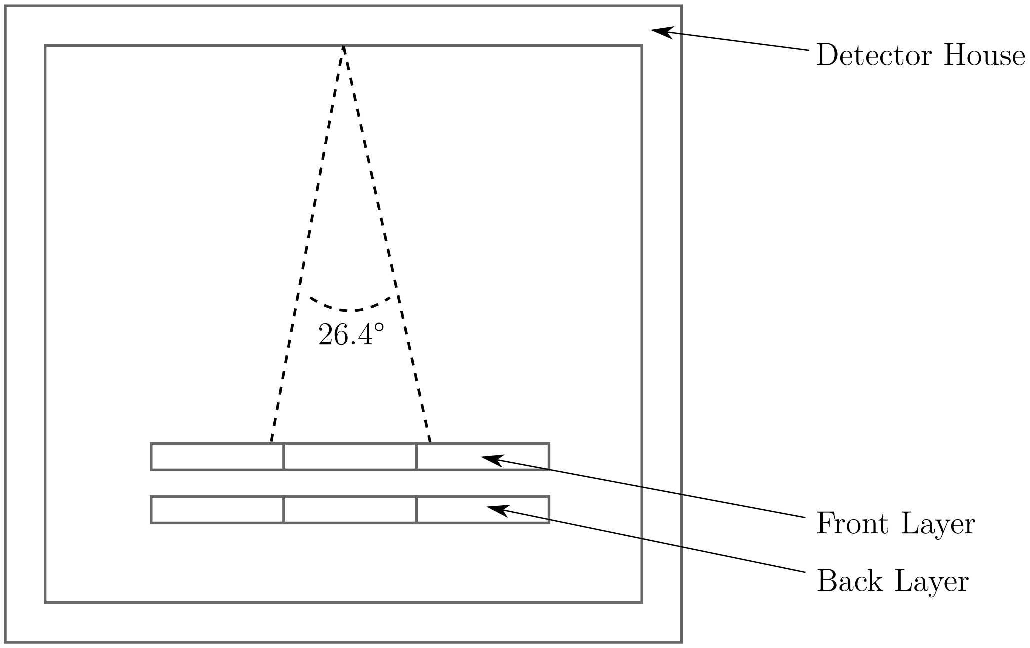

Figure 5.16: Illustration of the simulation setup 4.

5.4.5 Simulation Setup *Wide*

Simulation setup *Wide* is nearly identical to simulation setup 4. The difference is the electron distribution angle of the point source. In simulation setup *Wide* a wider beam is used. The beam has a half angle of 71°, and this is illustrated in figure 5.17. This simulation setup will provide information on baffles are needed to reduce backscattering within the detector house.

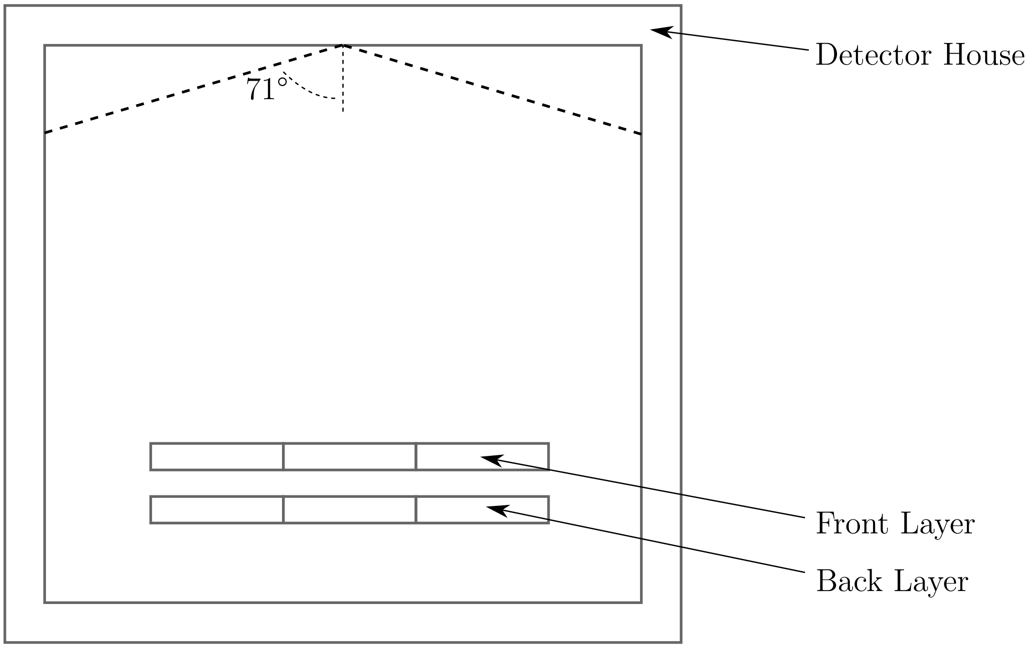

Figure 5.17: Illustration of the wide beam from the point source.

5.4.6 Simulation Setup *Mask*

This simulation setup introduces a wolfram-mask attached to the front layer. Figure 5.18 illustrates the simulation geometry. The purpose of this simulation is to investigate the effect this mask has on reducing scattering to nearby pixels, at various energies. The mask overlap the middle (pixel 5) with 1 mm and the thickness of the mask is 2.5 mm. The mask in this setup is designed so that the effect of a mask in terms of reduction in scattering out of an arbitrary pixel can be observed. The setup does not illustrate how the actual mask is attached. By adjusting the overlap and thickness of the mask the active sensor area can be optimized. Increasing the overlap and thickness of the mask indicates an increased reduction of scattering to nearby pixels. However, increasing the parameters comes with the expense of less active sensor area. Simulation results and discussion of the effectiveness at different energies can be found in chapter 7.1.2.

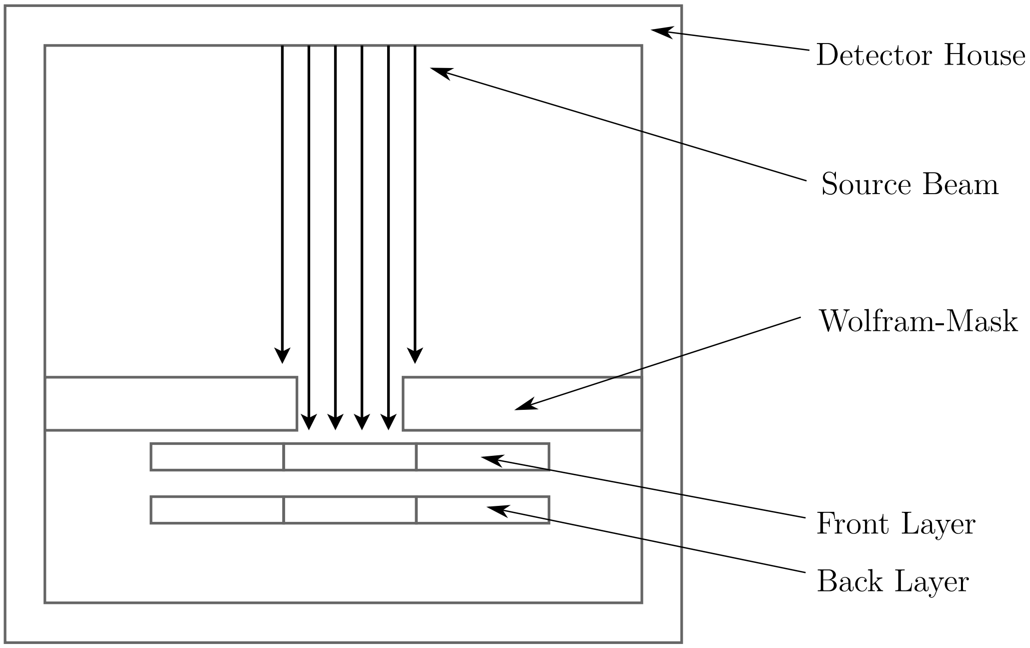

Figure 5.18: Illustration of the wolfram-mask simulation setup.

5.5 Data Extraction and Processing

The output of the GATE simulation is a ROOT file. This file consists of event ID's and the XYZ-coordinates with associated deposited energy. The purpose of the data extraction and processing is to sort the data. In this process a new file is created with relevant information presented in applicable matter for further interpretation. The file is named DEEP_OUTPUT.csv. The main purpose of this readout process is to create the pixels, as GATE only sees two silicon layers with dimensions of 15×15×1 mm. The pixels are arranged as described in chapter 5.1.2. The data file documents each event, and each new particle from the source is a new event. For each event the coordinates where the particle first hit the detector, and the energy deposited for each pixel in the detector is documented. As the front and the back layer are not pixelated, the pixels will be created in this readout process. The pixels are arranged as described earlier. The necessary information to document in the DEEP_OUTPUT.csv is the eventID, XYZ-coordinates of the first and last interaction, deposited energy in the pixels and a total deposited energy for all pixels for the event. The documented information is the foundation to calculate the amount of scattering to nearby pixels, absorbed energy per pixel, total absorption and total absorbed energy.

Table 5.10 shows an example of the data arrangement of the DEEP_OUTPUT.csv. In this example only the necessary parameters to give a clue on how the file is arranged are included. For each event, deposited energy is allocated to the correct pixel, as well as documenting where the incoming particle first hit (posX, posY). The sum of the deposited energy for each event is shown in the last column. The table shows an actual simulation consisting of electrons with energy equal to 960 keV. In event 0 and 2 all the energy has been deposited in pixel 5. For event 1 and 5 the electron penetrated the front layer (pixel 5 → pixel 14). Scattering to nearby pixels can be observed in event 4. Event 3, with its 370.09 keV deposited in pixel 5 is an example of backscattering. For further information about this process see appendix B.

eID	posX	posY	P5	P14	P1	P2	...	P17	P18	sumE
0	1.04	0.48	960.00	0.00	0.00	0.00	...	0.00	0.00	960.00
1	-1.57	1.21	602.90	357.10	0.00	0.00	...	0.00	0.00	960.00
2	0.18	-1.48	960.00	0.00	0.00	0.00	...	0.00	0.00	960.00
3	-0.35	1.65	370.09	0.00	0.00	0.00	...	0.00	0.00	370.09
4	-0.05	2.27	421.12	0.00	0.00	538.88	...	0.00	0.00	960.00
5	1.96	0.65	506.23	453.77	0.00	0.00	...	0.00	0.00	960.00

Table 5.10: Illustration of how the DEEP_OUTPUT.csv for electrons with energy equal to 960 keV is arranged.

CHAPTER 6

GATE Simulation Results

A total of 7 distinct simulation geometries were designed, and for each geometry 7 simulations were conducted. Every simulation had a monoenergetic electron beam. The energies that were simulated are 30, 60, 120, 240, 480, 960 and 1920 keV. These energies corresponds to the lower energy threshold of the integral energy channels used in the data binning, see chapter 7.2. A total of $1{\times}10^5$ particles were simulated for each energy. Stochastic models by definition imply uncertainty, but with adequate number of samples this uncertainty is manageable. Early experiments showed that $1{\times}10^5$ particles is adequate. This was decided when comparing results from $1{\times}10^4$, $5{\times}10^4$, $7.5{\times}10^4$, $1{\times}10^5$ and $2{\times}10^5$ particles with the same setup and energy. The simulation setup geometries are described in chapter 5. The results from the different simulation setups consist of absorbed energy in each pixel, each layer, scattering out of the pixels and energy distribution of the scattered particles. This chapter provides an overview of these results. For more detailed results for each energy interval for the simulation setup 1 and 2 see appendix C. For detailed results regarding all other simulation setup and energy distribution for each pixel see appendix D. For simplicity, total absorbed energy is abbreviated TAE and the number of scatterings is abbreviated SCT. SCT percentage indicates how many particles that have scattered into another pixel, except P5→P14.

6.1 Simulation Setup 1

This is the first DEEP simulation setup, which included a front and a back layer, where the front layer is closest to the source. The source is defined as a uniform monoenergetic electron beam and emit a parallel beam orthogonal to the detector and covering the area of the middle pixel (P5). The simulation setup geometry is described in chapter 5.4.2. Table 6.1 shows an overview of the results from each incoming energy. Figure 6.1 shows the total absorption as a function of energy, total absorbed energy and absorbed energy for the front and the back layer. The results indicate that when energy increases, the scattering of electrons out of P5 increases. Most of the energy below 1 MeV is absorbed in the front layer. At some point between 960 keV and 1920 keV this shifts, and more energy is absorbed in the back layer. In this energy range the total absorption rate also begins to rapidly decrease. This corresponds with what was expected from the total absorption calculated in section 5.3 earlier. It was not expected to see any hits in the back layer for 30 keV electrons. Investigating this further revealed that one electron was able to penetrate the front layer, the electron with eventID 13986. With a linear path throughout pixel 5 it was able to hit the back layer and deposit the remaining 18.487 keV energy. Considering the linear path that the particle had, little or no energy was lost in collisions throughout the pixel, and this is thereby seen as a plausible incident.

E [keV]	SCT	SCT [%]	TAE front	TAE back	Tot. Abs.	TAE
30	82	0.0	0.891	0.000	0.828	0.891
60	377	0.4	0.990	0.000	0.838	0.900
120	1153	1.1	0.907	0.001	0.843	0.908
240	3696	3.7	0.915	0.000	0.847	0.915
480	10342	10.2	0.927	0.000	0.850	0.927
960	80868	41.2	0.734	0.207	0.838	0.941
1920	148813	70.1	0.290	0.332	0.228	0.622

Table 6.1: Simulation setup 1 result overview.

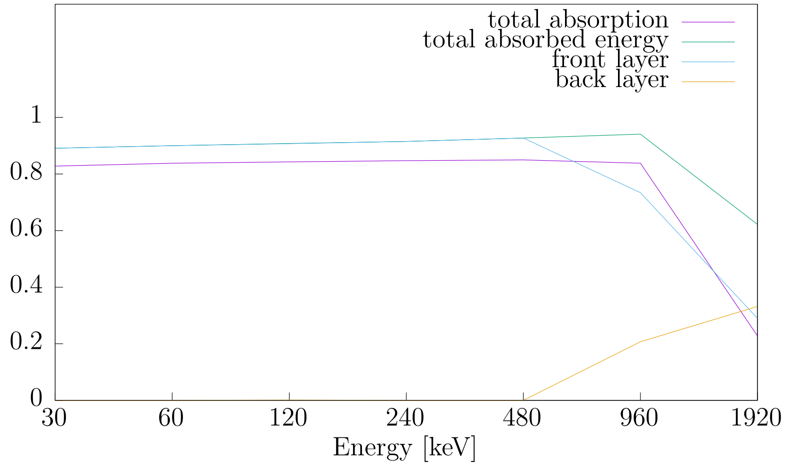

Figure 6.1: Overview of the results for both layers in simulation setup 1.

6.2 Simulation Setup 2

In this DEEP simulation setup the detector house was added. The geometry of the layers and parameters of the source are unchanged. The simulation setup geometry is described in chapter 5.4.2. In this simulation the effect from backscattering within the detector house is investigated. Table 6.2 shows an overview of the results from each incoming energy. Figure 6.2 shows the total absorption as a function of energy, total absorbed energy and absorbed energy for the front and the back layer. The results are similar to the simulation setup 1 results. The observed effect of adding a detector house is more scattering and absorbed energy in the outer pixels, especially in the back layer. The reason for the increased scattering in the back layer is that the backscattered electrons can scatter back down into the detector. In simulation setup 1, the backscattered electrons disappear out of the world after being backscattered. TAE in the back layer for 960 keV is 19.730×10^6 and it is very close to 19.703×10^6 as the TAE back in simulation setup 1. This is strange since for all the other energies the TAE in the back layer is higher in table 6.2 than in table 6.1.

E [keV]	SCT	SCT [%]	TAE front	TAE back	Tot. Abs.	TAE
30	1886	1.9	0.896	0.002	0.830	0.898
60	2096	2.1	0.905	0.001	0.839	0.906
120	2958	2.9	0.911	0.002	0.843	0.913
240	5363	5.3	0.919	0.001	0.848	0.920
480	11866	11.7	0.930	0.003	0.851	0.933
960	81736	42.2	0.737	0.209	0.839	0.946
1920	171652	92.3	0.300	0.387	0.230	0.687

Table 6.2: Simulation setup 2 result overview.

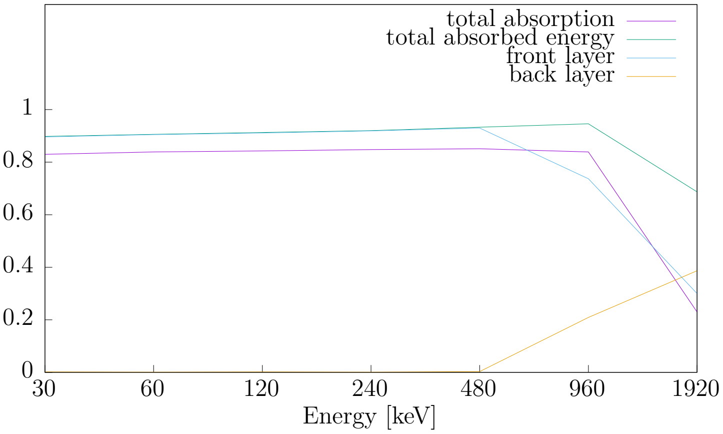

Figure 6.2: Overview of the results for both layers in simulation setup 2.

6.3 Simulation Setup 3

This DEEP simulation setup geometry is similar to the first DEEP simulation setup. However, the source is a point source that emanate electrons. This implies that electrons will hit the detector with different angles, and the degree of this effect is investigated. The simulation setup geometry is described in chapter 5.4.3. Table 6.3 shows an overview of the results from each incoming energy. Figure 6.3 shows the total absorption as a function of energy, total absorbed energy and absorbed energy for the front and the back layer. The overall results are quite similar to the results from simulation setup 1. A trend of less absorbed energy in the back layer is observed. The results indicate that particle hits near the outer edge of a pixel contribute to more scattering to nearby pixels. In this setup incoming electrons near the outer edges of P5 hits the detector at an angle. It is then reasonable that some of these electrons can scatter in a larger degree to a nearby pixel, as compared hits perpendicular to the detector. This leads to the conclusion that a non-perpendicular particle hit is less likely to penetrate the front layer and be detected in the back layer.

E [keV]	TAE front	TAE back	Tot. Abs.	TAE
30	0.888	0.000	0.824	0.888
60	0.895	0.000	0.831	0.895
120	0.902	0.000	0.837	0.902
240	0.912	0.000	0.843	0.912
480	0.923	0.000	0.845	0.923
960	0.735	0.204	0.835	0.939
1920	0.297	0.329	0.232	0.626

Table 6.3: Simulation setup 3 result overview.

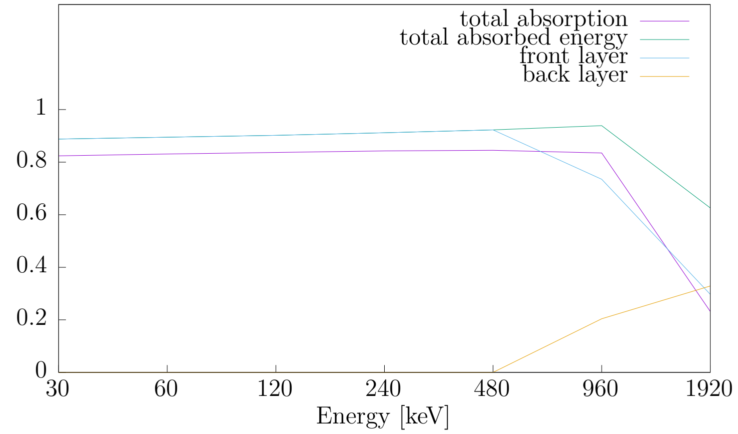

Figure 6.3: Overview of the results for both layers in simulation setup 3.

6.4 Simulation Setup 4

This DEEP simulation setup is a continuation of simulation setup 2 and 3. It uses the point source from setup 3 and the detector house from setup 2. The simulation setup geometry is described in chapter 5.4.4. Table 6.4 shows an overview of the results from each incoming energy. Figure 6.4 shows the total absorption as a function of energy, total absorbed energy and absorbed energy for the front and the back layer. Introducing particles with various incoming angles result in less energy absorbed in the back layer, as simulation setup 3 indicated as well. As indicated in simulation setup 2, by adding a detector house, more energy is absorbed as the particles that scattered out of the detector may hit the detector once more. Again, TAE in the back layer at 960 keV separate itself. TAE in the back layer for this energy is almost identical to all the other simulation setups.

E [keV]	TAE front	TAE back	Tot. Abs.	TAE
30	0.893	0.002	0.824	0.895
60	0.901	0.001	0.833	0.902
120	0.907	0.001	0.838	0.908
240	0.915	0.002	0.842	0.917
480	0.928	0.002	0.849	0.930
960	0.736	0.206	0.834	0.942
1920	0.304	0.381	0.229	0.685

Table 6.4: Simulation setup 4 result overview.

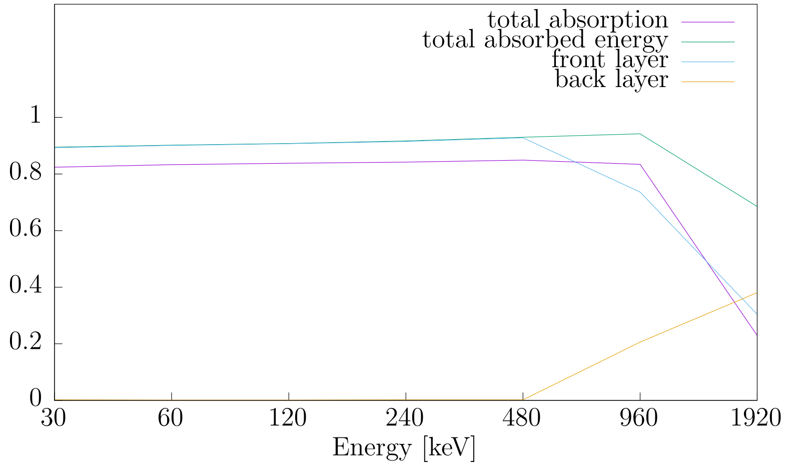

Figure 6.4: Overview of the results for both layers in simulation setup 4.

6.5 Simulation Setup *Wide*

The results from the simulation setup *Wide* indicated more scattering within the detector house. Simulation setup 4 provides adequate indication regarding the introduction of a point source and a detector house. For that reason, simulation setup *Wide* results are not provided here. However, it is of interest to reduce scattering off the walls and into the front and the back layer, and baffles should prevent this. This means that the purpose of setup *Wide* is to compare the results with the results from simulation setup *Baffle*, where the baffles are introduced. By comparing the results the effect of the baffles can be investigated.

6.6 Simulation Setup *Baffle*

Three layers of baffles, as illustrated in figure 6.5, are introduced in this simulation setup. The purpose of the baffles is to prevent electrons from backscattering down into the the front and the back layer after being backscattered from the walls of the detector house. This simulation setup will give relevant information for further detector design regarding baffles. As mentioned, by comparing the results from this simulation setup with the simulation setup *Wide*, the effect of the baffles are indicated. However, the focus was shifted to the mask-simulation, as the reduction in scattering had to be verified, as it is more relevant for this thesis. The focus shifted before all baffle 2 simulations were computed. Hence, no results are provided. Simulating all energies is proposed as further work.

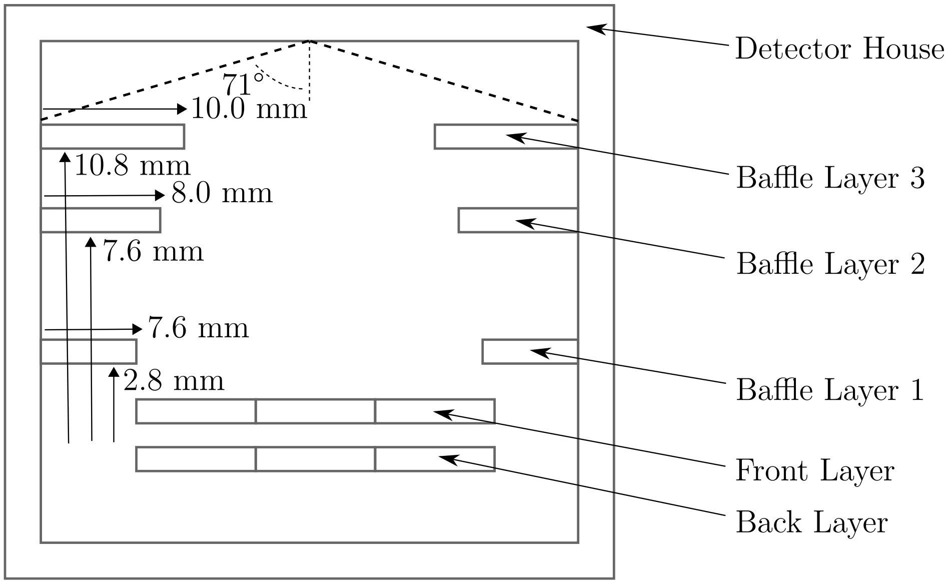

Figure 6.5: Illustration of the design of the three baffle layers, as well as the electron distribution angle of the point source.

6.7 Results Summary

A total of 7 distinct geometries were designed and simulated, and for each geometry 7 simulations were conducted with energies ranging between 30 to 1920 keV. It was uncovered that scattering, out of a pixel, increases with energy of the incoming electron. This results in uncertainty when determining which pixel was first hit if more than one pixel shows a hit at the same time. This implies that the DEEP instruments pixelated sensor has design weaknesses at high energies. At low energies the scattering to other pixels was negligible, involving 2 to 5 percent of incoming electrons. At higher energies this percentages increased to a maximum of 92.3 % at 1920 keV. At 960 keV it was 42.2 %, and at 480 keV it was 11.7 %. The scattering cross section decreases with increasing energy, this involves both elastic and inelastic spread. An electron with high energy has an increased chance to scatter out of a pixel without being absorbed, in comparison with a low energy electron. At low energy, the spread is larger, and thus the chance of scattering out of a pixel is smaller. At high energy the spread is smaller, but the effect of the spread is more severe, and thus the chance to scatter out of a pixel is larger. The simulation also indicated the effect of backscattering within the detector house.

Figure 6.6 and 6.7 illustrates the difference in scattering between electrons with energy equal to 500 and 1500 keV. The middle pixel is located between -2.5 and 2.5 mm. Some steps are needed to prevent electron scattering becoming a problem when evaluating the readout at higher energies. In chapter 7 those steps will be discussed.

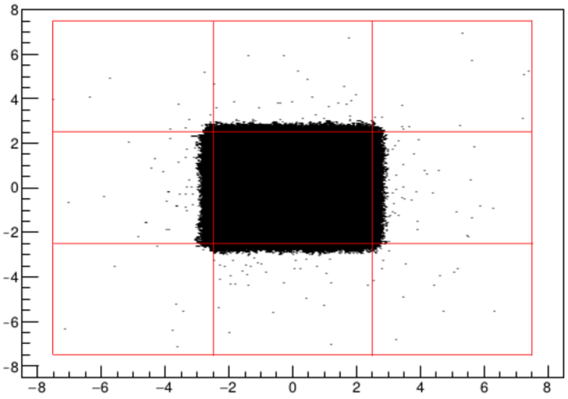

Figure 6.6: Electron scattering with energy equal to 500 keV.

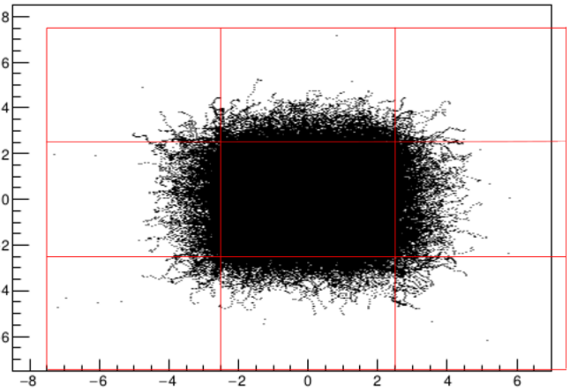

Figure 6.7: Electron scattering with energy equal to 1500 keV.

CHAPTER 7

Back-end Electronics

The main purpose of the back-end electronics is to perform digital signal processing of the incoming data. In addition, it needs to buffer and offload data, as well as controlling the data. Figure 7.1 illustrates the three main functions the DSP needs to cover. These functions are coincidence check, data binning and data packing. The FPGA is discussed in chapter 4.7. This chapter covers solutions to the electron scattering problem at higher energies, as well as detailed information about the three main DSP functions. Finally, a test system for the back-end electronics is briefly discussed.

Figure 7.1: Block diagram of the three main functions the DSP must cover.

7.1 Coincidence Check

The coincidence check adds together the energy absorbed in the front and back layer pixels in the detector. This information is used to determine the energy of the incoming particle. It may also be used to determine the direction of the incoming particle (Front→Back or Back→Front). Figure 7.2 illustrates the pixels for the electron and the proton detector. There are two types of coincidences that can occur, these are vertical and horizontal coincidence. Both will be introduced further. Simply stated, a particle can hit the pixels in the detector vertically (E1→E9) or horizontally (E1→E2), and in some cases both as the simulations indicated. Hits in more than one horizontal pixel in the same sampling interval makes the exact determination of direction impossible. Solutions to manage the horizontal scattering is proposed.

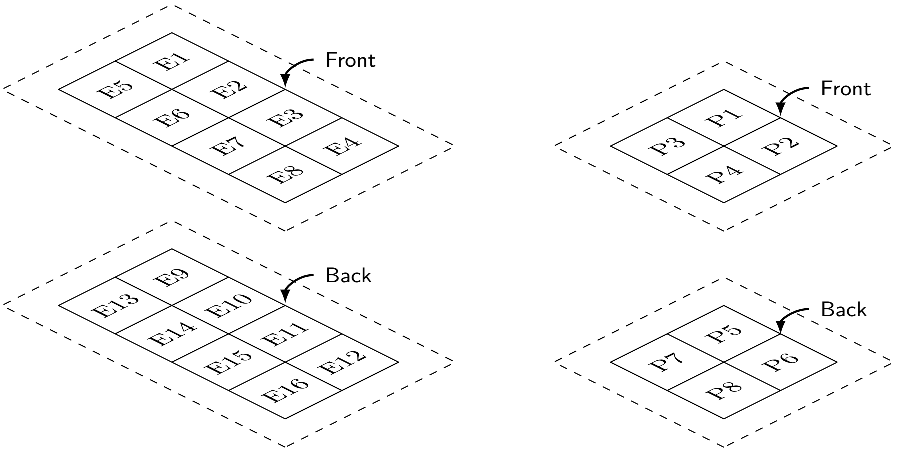

(a) The electron pixels. (b) The proton pixels.

Figure 7.2: The detector pixels.

7.1.1 Vertical Coincidence

Vertical coincidence is when a particle hit is detected vertical through both the front and back pixel. This type of coincidence will give information about the total energy of the incoming particle and may be used to determine the incoming direction (Front→Back or Back→Front) of the particle as well. Two methods for detecting a particle is considered.

The straightforward scenario

In this scenario it is assumed that the incoming particle can be detected first in the front pixel and then in the back, or vice versa. If this happens, it is possible to determine the direction (Front→Back or Back→Front) of the incoming particle. To verify if this scenario is practical, the time it takes for a particle to travel between the pixels must be calculated. This time implies at what sampling frequency the electronics need to operate on to record this. Figure 7.3 illustrates the size of the electron pixel and figure 7.4 illustrates the size of the proton pixel.

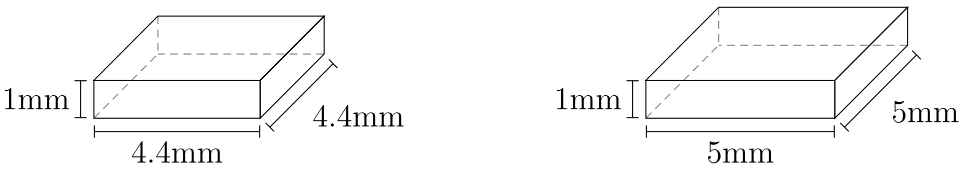

(a) Front pixel size. (b) Back pixel size.

Figure 7.3: The size of the electron pixels.

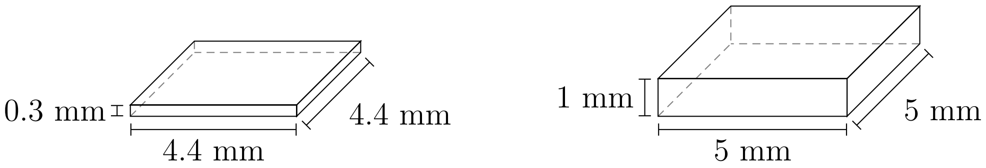

(a) Front pixel size.

(b) Back pixel size.

Figure 7.4: The size of the proton pixels.

Based on the simulations it was found that an electron must have an energy at approximately 480 keV to be able (to a large extent) to penetrate the front layer pixel and hit the back layer pixel. Electrons with this energy will have relativistic velocity. The distance between the front and back pixel is 0.4 mm. The distance between the top of the front pixel and the top of the back pixel is therefore 1.4 mm. The time of travel for the electron is, assuming the speed of light:

$$t_e \approx \frac{1.4 \times 10^{-3} m}{3 \times 10^{8} m/s} = 4.7 \times 10^{12} s = 4.7 ps.$$

The proton, on the other hand, must have an energy equal or higher than 5 MeV to be able to penetrate the front layer pixel and hit the back layer pixel. At this energy, it is assumed that the proton will have a velocity equal to 0.1 of the speed of light. The distance between the top of the front pixel and the top of the back pixel is 0.7 mm. The time of travel for the proton is:

$$t_p \approx \frac{0.7 \times 10^{-3} m}{3 \times 10^{7} m/s} = 23.3 \times 10^{12} s = 23.3 ps.$$

Based on the calculation the time of travel for the electron between the front and the back layer is 4.7 picoseconds. To be able to detect if the electron hits the front or the back layer first the repeating event per unit of time (frequency), must be calculated. The frequency for the electron is roughly 200 GHz. According to the Nyquist Theorem, to adequately reproduce a signal it should be periodically sampled at a rate equal to, or greater than, twice the highest frequency. Sampling at this rate will prevent aliasing. Aliasing is an effect that causes signals to become falsely represented. Based on this, to be able to detect if a particle first hit the front or the back, a sampling frequency in the magnitude of hundreds of gigahertz is needed. This is not possible, thus another solution must be found.

The most likely scenario

The most likely scenario consider that the energy deposited is dependent on the incoming energy. The ratio between the energy deposited in the front detector and in the back detector is dependant on the energy of the incoming electron. This relationship can be seen in figure 7.5. The black line illustrates the incoming energy. The energy deposited in the pixels can be compared to determine which direction the particle came from. For low energy electrons: the energy deposited in the front layer is larger than the energy deposited in the back layer, the particle must have hit the front before the back, and thus the direction Front→Back (F→B) is determined. However, as the energy increases, it will at some point be opposite.

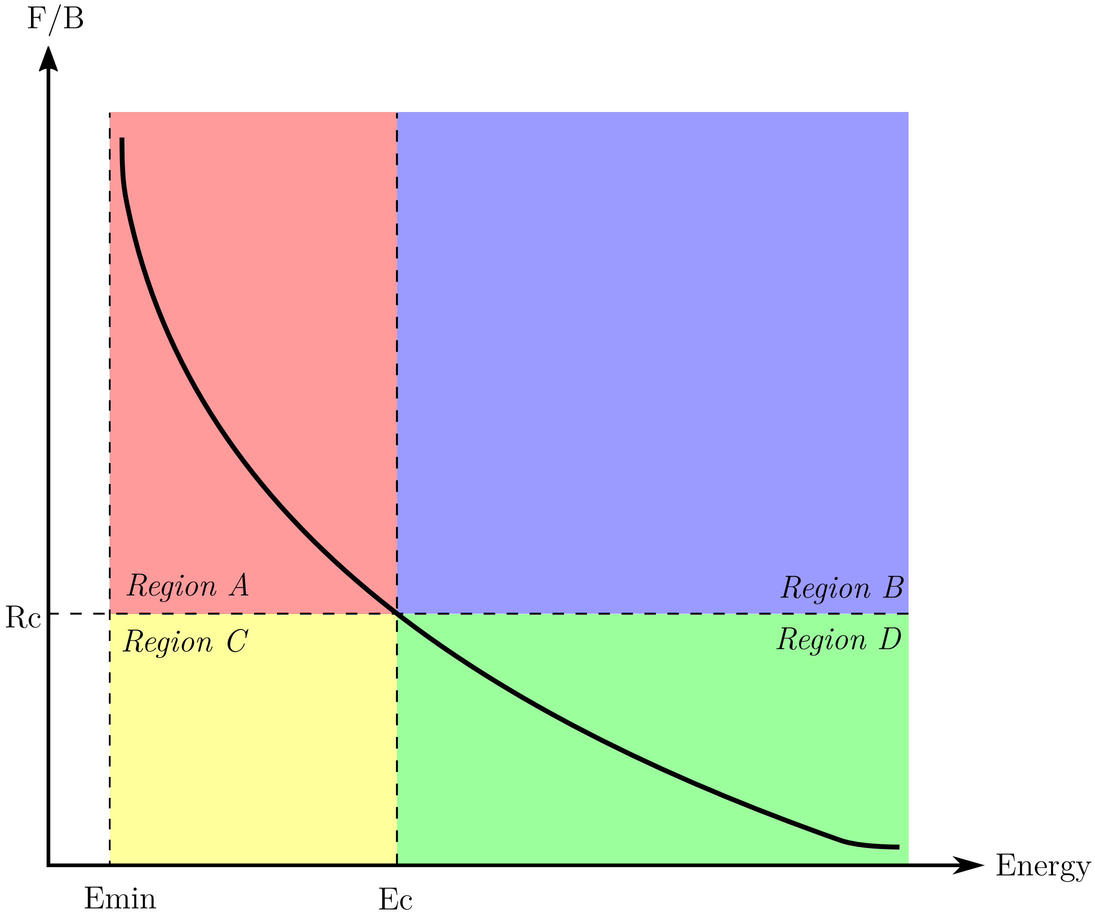

Figure 7.5: The correlation between incoming energy (black line) and the ratio between the deposited energy in the front and back detector.

E_{min} is the minimum detectable energy. If energies near E_{min} has a Front/Back (F/B) ratio above the critical ratio (R_C), the direction of the particles is Front→Back. The same conclusion can be made for all energies up to the critical energy (E_C). In region A the direction of the particle is Front→Back. Region C show particles with the same energy, but with a ratio less than R_C, which means the direction of the particle is Back→Front. For energies above E_C the behaviour is opposite of the behaviour in region A and C. In region B, where the energy is higher than E_C and the Front/Back ratio is above R_C, the direction of the particle is Back→Front. In region D, with the same particle energy, but with a ratio less than R_C, the particle direction is Front→Back.

A module that can determine vertical coincidence is proposed in figure 7.6. This algorithm take front and back pixels as input and decide which of the pixels that were hit first and gives that as output. If a particle hit only the front layer, the information is stored. However, if only the back layer is hit, the information is not stored, but the incident will be recorded. The same happens when it is determined that a particle hit the back layer before the front. However, if the satellite link and data requirements allow it, information about these scenarios could be stored as well. Information on all hits are stored, but only data from particles determined to have hit the front layer, or Front→Back is sent into the data binning module. Table 7.1 shows the truth table for the vertical coincidence module. Figure 7.7 illustrates the design architecture and flow of the module.

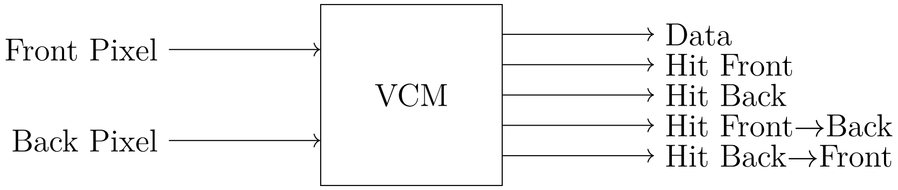

Figure 7.6: Vertical coincidence module.

In	F+B Sum	F/B Ratio	Region	HitF	HitB	HitF→B	HitB→F	Data
F	B=0	∞	A	1	0	0	0	F
B	F=0	0	C	0	1	0	0	0
F&B	Sum<E_C	>R_C	A	1	1	1	0	F+B
F&B	Sum<E_C	<R_C	C	1	1	0	1	0
F&B	Sum>E_C	<R_C	D	1	1	1	0	F+B
F&B	Sum>E_C	>R_C	B	1	1	0	1	0

Table 7.1: Truth table for the vertical coincidence module.

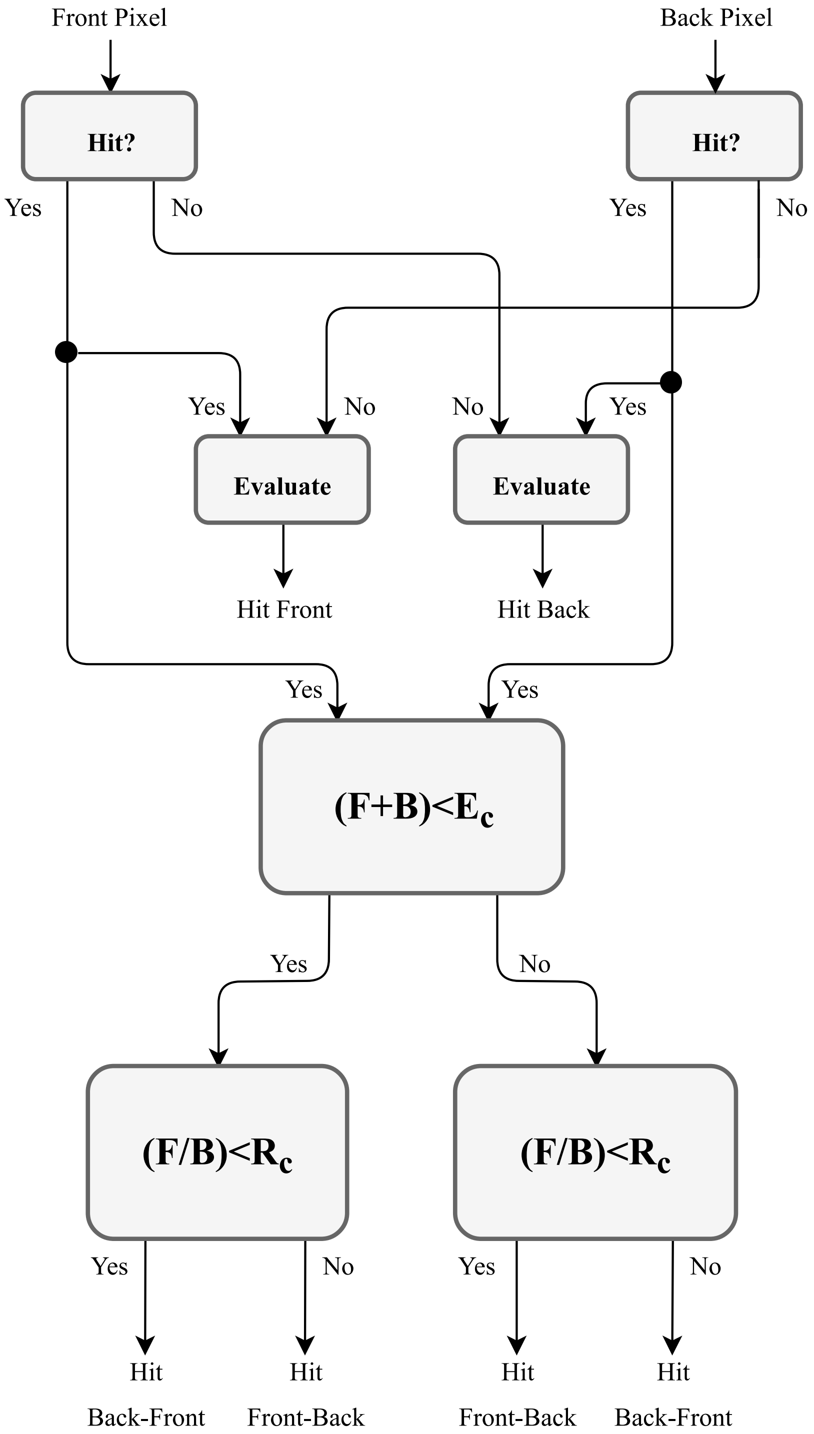

Figure 7.7: Design architecture and flow of the vertical coincidence module.

7.1.2 Horizontal Coincidence

Horizontal coincidence is when a hit is detected horizontal over either the front or back pixels. An example of this is a particle hit in pixels E1 and E2. For electrons this coincidence is the one that cause the most problems. For protons, on the other hand, horizontal coincidence is less likely to occur as protons scatter less than electrons. Protons will have a much more linear path throughout the sensor. The geometry of the detector house must be designed so that horizontal hits are minimized. Two solutions to the electron scattering problem is presented. Both solutions have their advantages and disadvantages. An optimum solution, which is a combination of the two, is proposed as well. Deciding on a method will ultimately depend on power, memory, or weight requirements.

The Super Pixel

The Super Pixel (SP) method combines pixels, resulting in the creation of larger pixels. This is illustrated in figure 7.8, where E1-E2 is combined to a super pixel. By creating super pixels all hits are recorded. A total of 13 super pixels is needed. Table 7.2 indicates this arrangement. For instance, SP1 consists of the pixels E1+E2+E9+E10.

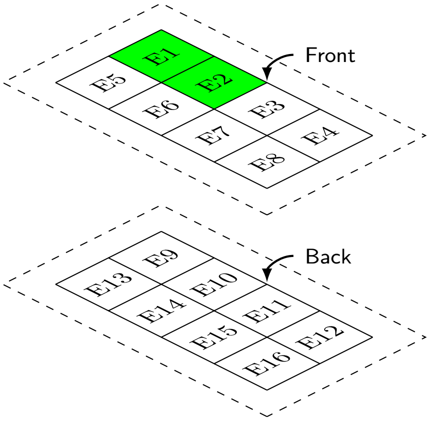

Figure 7.8: Illustration of a super pixel consisting of pixel E1 and E2.

The proposed super pixels are based on the simulation results, in regards of the range electrons can scatter. As the DEEP instrument has a pixel design it should be able to handle bad pixels as well. A bad pixel could be a pixel that does not behave as expected, or that is producing anomalous values. Either way, no information should be extracted from them. The data obtained by the bad pixel is less reliable, and can in a worst case scenario give wrong scientific data. The super pixel solution comes at the expense of greater data packet size, resulting in larger memory requirements. This method is complex to fully implement and include many variants, and it is unlikely that all these variants provide any benefits.

SP	Pixel	1	2	3	4	5	6	7	8	9	10	11	12	13	14	15	16
1		1	2							9	10						
2		1				5				9				13			
3						5	6							13	14		
4			2				6				10				14		
5			2	3							10	11					
6							6	7							14	15	
7				3				7				11				15	
8				3	4							11	12				
9								7	8							15	16
10					4				8				12				16
11		1	2			5	6			9	10			13	14		
12			2	3			6	7			10	11			14	15	
13				3	4			7	8			11	12			15	16

Table 7.2: Arrangement of the super pixels.

Masking the Pixels

By masking the pixels mechanically, as illustrated in figure 7.9, the problem of horizontal scattering is managed before the back-end electronics is involved. Masking will also result in a reduction of overall processing power. However, the solution comes at the expense of less particle flux on the sensors and more overall backscattering in the detector.

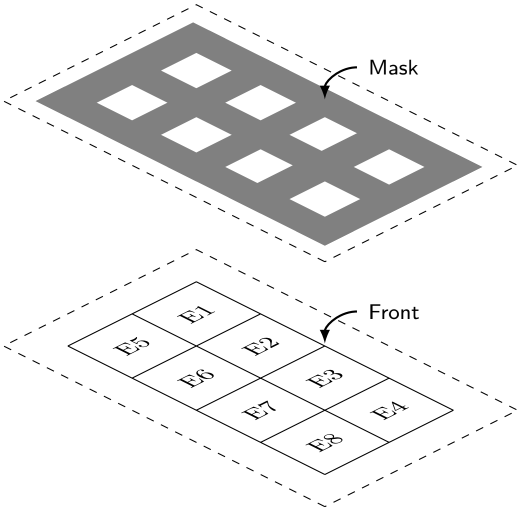

Figure 7.9: Illustration of the mask which will be attached to the front layer.

Based on the results in chapter 5.2, a 1 mm wide mask (from outer edge to centre) is proposed. The results indicate that the majority of the particles are not able to scatter more than 1 mm. However, a major concern with this solution is the rapidly decreasing sensor area as the mask size is increased. A total mask width of 2 mm separate the pixels by 1 mm, as illustrated in figure 7.10.

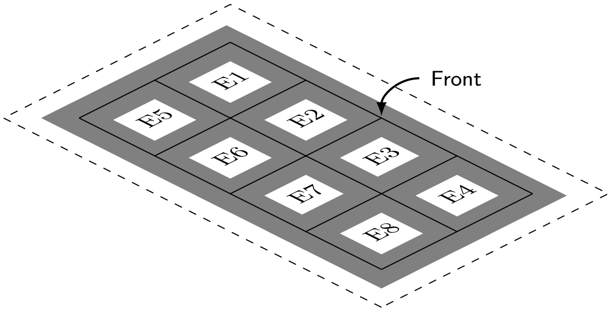

Figure 7.10: Illustration of the mask attached to the front layer.

The thickness of the mask should be at least 2 mm to prevent high energy particles to penetrate the mask, which contaminates the results. The mask must be attached to the front layer of the detector, where the dimensions of a pixel are somewhat smaller than the dimensions of the back pixel. A complicating factor is that the incoming particles at the edges will have a relatively large incoming angle. This means that the mask must be shifted slightly in relation to the dividing line between the pixels. Table 7.3 shows the sensor area with related mask width and the active sensor area decreases rapidly with the width of the mask. Masking every pixel with a 1 mm thick mask reduces the active sensor area from 155 mm^2 to 46 mm^2. This is a 70 % reduction, or a factor 3 reduction.

Mask Width [mm]	Sensor Area [mm^2]	Reduction [%]
0.00	154.9	N/A
0.25	121.7	21.4
0.50	92.5	40.3
0.75	67.3	56.6
1.00	46.1	70.2
1.25	28.9	81.3
1.50	15.7	89.9

Table 7.3: Active sensor area with related mask widths.

A simulation setup geometry which tested the effect of masking showed that scattering, out of a pixel, was decreased by employing a wolfram-mask. The simulation setup is identical to setup 2, except for the added mask.

The improvement (imp.) by employing a 2 mm wide, 2.5 mm thick wolfram-mask is observed in table 7.4. The largest improvement of 75 % (factor 3.94 reduction) was achieved at 960 keV. Improvement was achieved at 480 and 1920 keV as well, with 65 % (factor 2.85 reduction) and 55 % (factor 2.23 reduction). Improvement is expected at all energies below 240 keV. By adjusting the width and the thickness of the mask further reduction in scattering can be achieved, but at the expense of the active sensor area. The dimensions of the front layer pixels in the simulations were 5×5 mm, and the dimensions of the front layer pixels in DEEP instrument are 4.4×4.4 mm. The expected effect of this is increased scattering in the pixel directly behind the front layer pixel that was hit. By either using a wider or thicker mask, scattering can be improved further, but at the expense of active sensor area.

E [keV]	SCT (w/o mask) [%]	SCT (w/ mask) [%]	Imp. [%]	Factor
30	1.9	N/A	N/A	N/A
60	2.1	N/A	N/A	N/A
120	2.9	N/A	N/A	N/A
240	5.3	3.4	35.5	1.56
480	11.7	4.1	65.1	2.85
960	42.2	10.7	74.7	3.94
1920	92.3	41.3	55.3	2.23

Table 7.4: Effect of 1 mm wide and 2.5 mm thick wolfram-mask.

Optimum Solution

By combining the super pixel method and masking method, an optimum solution is achieved. This method will balance the advantages and disadvantages of the two. The solution is illustrated in figure 7.11.

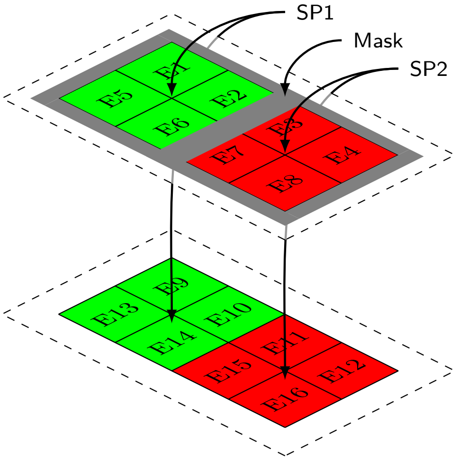

Figure 7.11: Optimum solution employing a mask and two super pixels.

Two super pixels are created, and the arrangement can be observed in table 7.5. Masking the sides with 0.5 mm and the middle pixels with 1 mm, result in an active sensor area of 114 mm^2. This is a 26 % reduction, or a factor 1.4 down. Another possibility is removing the masking on the long edges all together. This results in an active sensor area of 137 mm^2. The final decision will on be based on the compromise between active sensor area and horizontal hits. For the lowest energies, around 480 keV, no super pixels are needed, as only 2 to 5 percent of the incoming electrons scatter to nearby pixels. However, the need for a super pixel will be kept a record on, as this will indicate how many particles has scattered into a nearby pixel. For the highest energies a super pixel is needed for almost every incoming particle and thus, only super pixels will be used.

SP	Pixel	1	2	3	4	5	6	7	8	9	10	11	12	13	14	15	16
1		1	2			5	6			9	10			13	14		
2				3	4			7	8			11	12			15	16

Table 7.5: Arrangement of the super pixels for the optimum solution.

Figure 7.12 illustrates the design architecture and flow of the optimum solution algorithm. Considering a scenario with a hit in pixel E1:

If a hit is registered in pixel E1, a horizontal coincidence check with pixels E2/E5/E6 is performed. If a hit is registered in the E2/E5/E6 pixels, the values are added together, and the corresponding back layer pixels (E9+E10+E13+E14) are added together. This essentially creates the super pixel 1. A vertical coincidence check is then performed.

If there are no hits in pixels E2/E5/E6, a vertical coincidence check is performed. The optimum solution algorithm can be implemented using hardware implementation. Such implementation of DSP algorithms usually shows higher performance compared to software implementation. FPGAs can easily implement algorithms with higher parallelism.

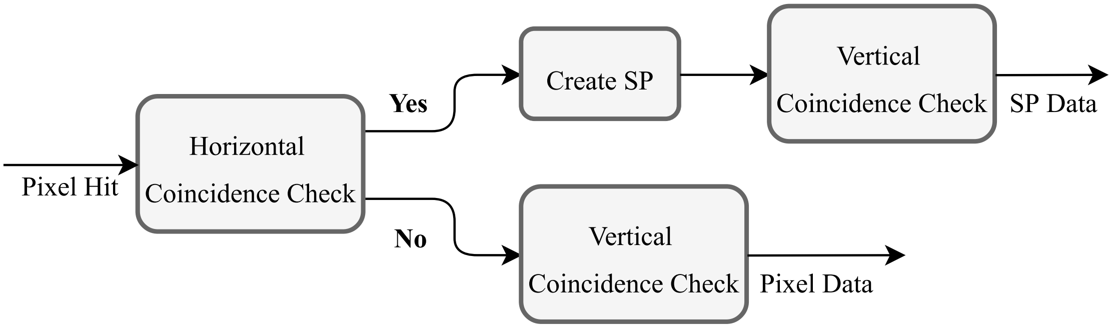

Figure 7.12: Design architecture and flow of the optimum solution.

7.2 Data Binning

The data pre-processing technique of data binning is used to reduce the data size and thus make it possible to transfer the data with a satellite link. A histogram is used to represent the distribution of the numerical data from each pixel. It is expected that 7 energy bins provide sufficient scientific data.

Figure 7.13 shows the typical expected count rate out of the front-end electronics for the different energies [26]. As observed, the count rate decreases rapidly with increasing energy. This relationship can be taken advantage of when determining the various bin sizes. The maximal count rate is observed at 30 keV. It is the front-end electronic that determines this rate.

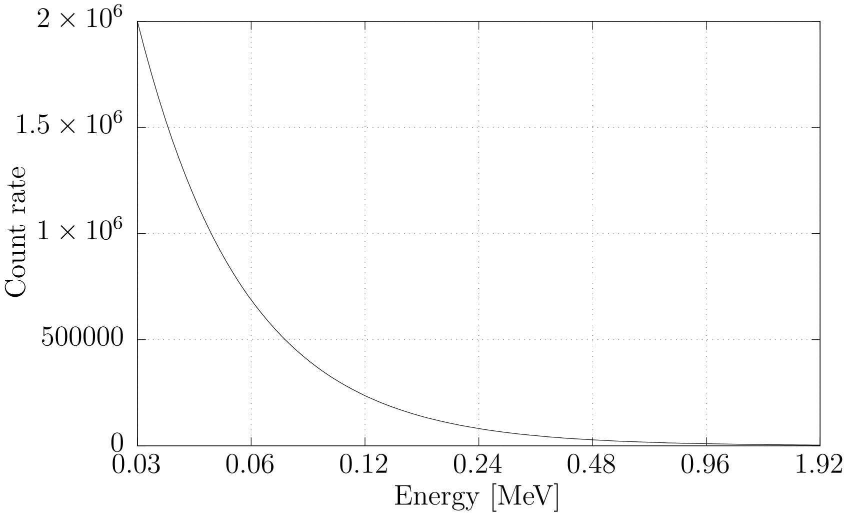

Figure 7.13: Expected count rate out of the front-end electronics.

To cover the highest count rate of 1×10^6 at 30 keV, a bin size of 21 bit is sufficient. However, the Medium Energy Proton and Electron Detector (MEPED), which is a similar instrument on the Polar Orbiting Environmental Satellites (POES), achieved a count rate of 1.5×10^5 at 30 keV [33]. It is likely that the instrument was paralyzed at high count rates. The real count rate would be in the order of 2×10^6 [34]. This leads to the conclusion that the DEEP instrument should be designed for an even higher count rate. The CPU on the Microsemi SmartFusion2 SoC FPGA is an ARM Cortex-M3 32-bit microprocessor [28]. This means 32-bit registers and addresses are used [35], hence a bin size of 32 bit is suggested. A possible solution is to split the 32 bit into 2×16 bit, but this provides little room for error detecting and correcting codes. With a 32 bit bin there is plenty of room to implement error detecting and correcting codes. Table 7.6 shows the expected count rate, minimum- and proposed bin sizes for the 7 energy bins.

Energy [keV]	Count Rate	Minimum Bin Size	Prop. Bin Size
30	2,000,000	21 bit = 2,097,152	32 bit
60	687,283	20 bit = 1,048,576	32 bit
120	236,180	18 bit = 262,144	32 bit
240	81,161	17 bit = 131,072	32 bit
480	27,891	15 bit = 32,768	32 bit
960	9,584	14 bit = 16,384	32 bit
1920	3,293	12 bit = 4,096	32 bit

Table 7.6: Expected count rate, minimum- and proposed bin sizes for the various energies.

Data from each pixel will be distributed into 7 energy bins. Table 7.7 shows the energy resolution for each bin. Table 7.8 shows the same for the proton detector. In addition, the tables include proposed bin sizes for various bit precisions, ranging from 8- to 12-bit resolution. The exact bit precision is to be decided at a later stage, based on the front-end electronics.

Bin	Energy [keV]	Size [bit]	8-bit	10-bit	12-bit
0	>30		>4	>16	>64
1	>60		>8	>32	>128
2	>120		>16	>64	>256
3	>240		>32	>128	>512
4	>480		>64	>256	>1024
5	>960		>128	>512	>2048
6	>1920		>255	>1023	>4095

Table 7.7: Bin sizes for the electron detector with various bit precisions.

Bin	Energy [keV]	Size [bit]	8-bit	10-bit	12-bit
0	>150		>4	>16	>64
1	>300		>8	>32	>128
2	>600		>16	>64	>256
3	>1200		>32	>128	>512
4	>2400		>64	>256	>1024
5	>4800		>128	>512	>2048
6	>9600		>255	>1023	>4095

Table 7.8: Bin sizes for the proton detector with various bit precisions.

Figure 7.14 illustrates the design architecture and flow of the data binning, and it is implemented as a loop. First it checks if the binning length timer is reached. If the timer criteria is not met, the data is evaluated and the correct bin increases its value by one. If the timer is reached, the readout control initiates readout of the hit counts in the bins, in addition to resetting the binning length timer.

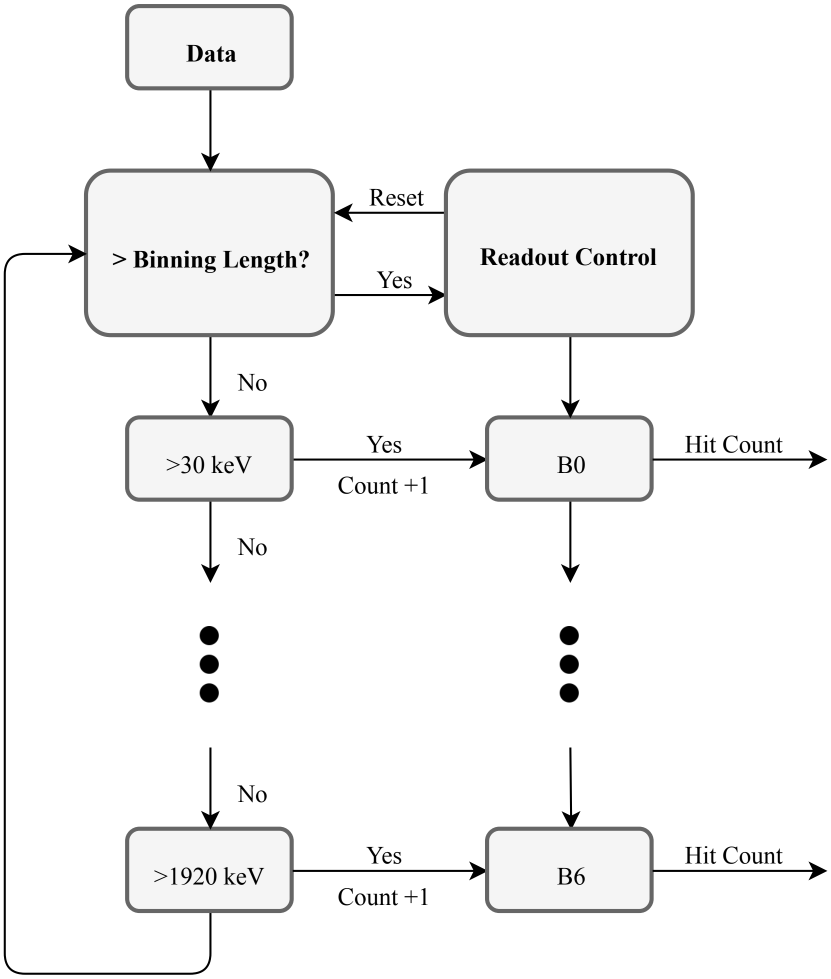

Figure 7.14: Design architecture and flow of the data binning.

7.3 Packet Definition

Over a digital network a packet is a basic unit of communication. Depending on the protocol, the structure of the packet is decided. The typical packet has a header, a payload and a trailer. The data packet is illustrated in figure 7.15. Information about error-detection and error-correction is based on [21] and [36].

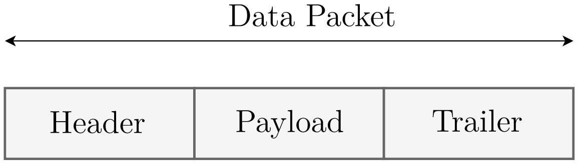

Figure 7.15: The structure of the data packet.

The header keeps overhead information about the packet and other transmission related data. The instructions a typical header contains are the length of the packet, synchronization bits, packet number, which protocol is used, destination address and the originating address. Some systems have fixed-lengths packets, while others rely on the header to contain this information. Synchronization bits will help the packet match up to the receiving system.

The payload is the actual data the packet is delivering. The payload may also be referred to as the body or the data. The payload may be padded with blank information (zeros) to make it the right size in a fixed-length packet system. Information in the energy bins is the payload for the DEEP instrument. This information must be packed in practical manner and it is assumed that the data always arrive in the same order.

The trailer contains information to inform the receiving device that it has reached the end of the packet. The trailer may also be referred to as the footer. Error-detecting and error-correcting codes can be implemented to increase system reliability. Error-detecting and error-correcting codes can be used to detect any accidental changes to raw data. Bit-flips can be detected and corrected by adding a few extra check bits to each bin. In some systems the receiving device can send a request back to the originating device requesting it to resend that packet.

7.3.1 Error Control

Cyclic Redundancy Check (CRC) is a common error checking used in packets. CRC is an error-detecting code and can detect accidental changes to raw data. When blocks of data enters the system each block gets a short check value attached. The check value is based on the remainder of a polynomial division of their contents. On the receiving device the calculation is repeated and, in the event the check values does not match, action can be taken to prevent data corruption.

Error-Correcting Codes (ECCs) can detect and correct bit-flips. ECCs uses multiple parity check bits and each bit is a parity bit for a group of data bits. When the receiving device receive data it can evaluate parity of each group, including the check bit. If the parity is correct for all groups it implies that no detectable error has occurred. If one or more parity values are incorrect, the pattern of check bits that have the wrong parity is called the syndrome. The syndrome can be used identify which bit position has an error and the receiver can flip this bit in order to recover the correct result.

Hamming code is a common type of ECC. In Hamming code y parity bits are added to an x-bit data word, forming a new word of x+y bits. The code can be used with words of any length. For a bin size of 32 bit, a 5 bit Hamming code is needed. This means that the effective 27 bits can be used (to count hits) and this is plenty of bits for all energies. Implementing this code, which does not increase the total payload size, will give a significant increase in reliability.

7.3.2 Electron Payload

The electron payload will be arranged with a constant size of 27 bits for every energy bin. Table 7.9 shows the bits needed to describe the necessary parameters for the electron payload with energy channels. The parameters are the detector house (DH), sensor (S), bin with hit count (b) and ECC bits. A total of 229 bit is needed.

	DH	S	b0	b1	b2	b3	b4	b5	b6	ECC
Bits	2	3	27	27	27	27	27	27	27	35

Table 7.9: Electron payload with 7 energy channels and equal bin size.

7.3.3 Proton Payload

It is assumed that the proton payload can be arranged similar to the electron payload, which implies a total of 229 bit is needed.

7.3.4 Size of the Payload Packet

The EDS has 48/2 pixels, which implies that the total size for the system is 5,496 bits. The PDS has 24/2 pixels, which implies that the total size of the system is 2,748 bits. Adding these values together the total is 8,244 bits. This results in total data generation of 45 Mbit/orbit with a constant bin size. The size of the payload packet with the super pixel method, which introduced 13 additional pixels, is 61 Mbit/orbit. The size of the payload packet with optimum solution method, which introduced two new pixels, is 47 Mbit/orbit. Figure 7.16 shows how the payload data size increases with increasing bins for this solution.

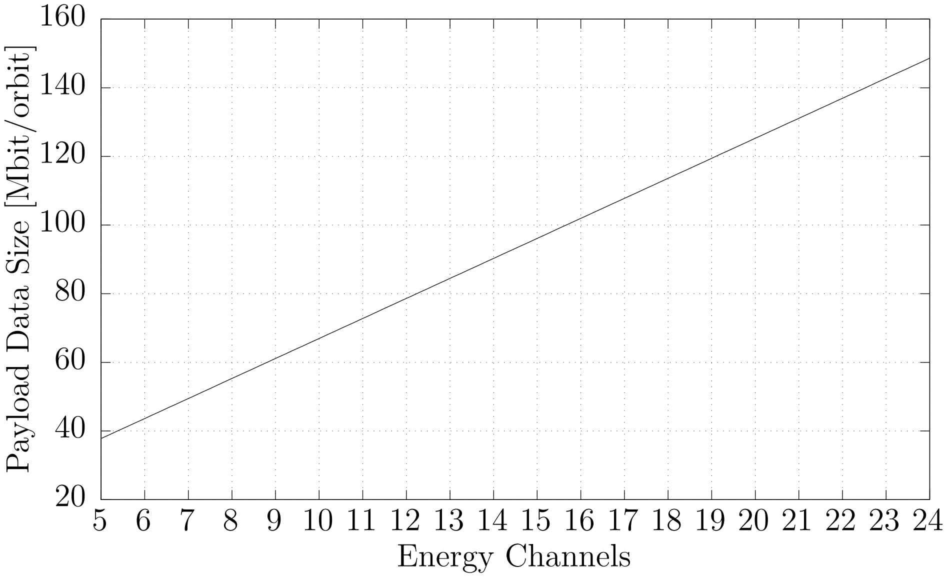

Figure 7.16: Payload data size as a function of number of energy channels for the optimum solution.

7.4 System Implementation

The use of a System on Chip (SoC) design has become increasingly common, due to the constant development of ever more complex systems. With a SoC system it is implied that the system combines different hardware modules through a common bus, on a single chip. A SoC configuration test system for the back-end electronics is proposed. In addition, a structured testbench architecture for verifying the VHDL code is designed and implemented.

7.4.1 Test System

The purpose of the back-end electronics test system is to verify the behaviour of the DSP functions. This can be achieved by sending validation data (synthetic real-life data) on the input, process this data in the FPGA and comparing the output data with input data. A proposed back-end electronics test system is illustrated in figure 7.17. Validation data is input on the Central Processing Unit (CPU) using e.g. an Ethernet cable. This data is temporary stored in a ring buffer before transferred into the FPGA. The FPGA has FIFOs that will buffer data and ensure that no data is lost. The DSP can choose from two distinct inputs and a multiplexer (MUX) decides which data stream is used. This means that the DSP has the option to either test the synthetic validation data or process actual data from the DEEP instrument sensor. The sensor can be tested using an electron beam. The signal from the sensor must be fed to the ADC IC.

At the time of writing, two master students at UiB are working on a system for a detector capable of detecting Terrestrial Gamma-ray Flashes (TGFs) [37] [38]. Their system has similar functionality as the test system proposed in this thesis. Their system uses a Xilinx Digilent Zybo SoC Trainer Board. The board contains the Z-7010 SoC, and features peripherals such as gigabit ethernet and SD memory card capability. The SoC uses a dual-core microprocessor system embedded on a FPGA. This means that DSP functions proposed in this thesis can be implemented and tested on their system, without much effort. Occasionally, it is possible to define modules that enable reuse, and regularity is the principle that define similar modules for reuse. In this occasion a system will be reused. Reuse simplifies the design process and minimizes the effort needed to verify the functionality. Reuse of existing design do not only reduce cost and effort, but will also enhance the quality of the existing design, as reuse verifies the behaviour. Reuse leads to reduced time spent on development. To verify the behaviour of the DSP functions proposed in this thesis, the mentioned SoC system will be reused.

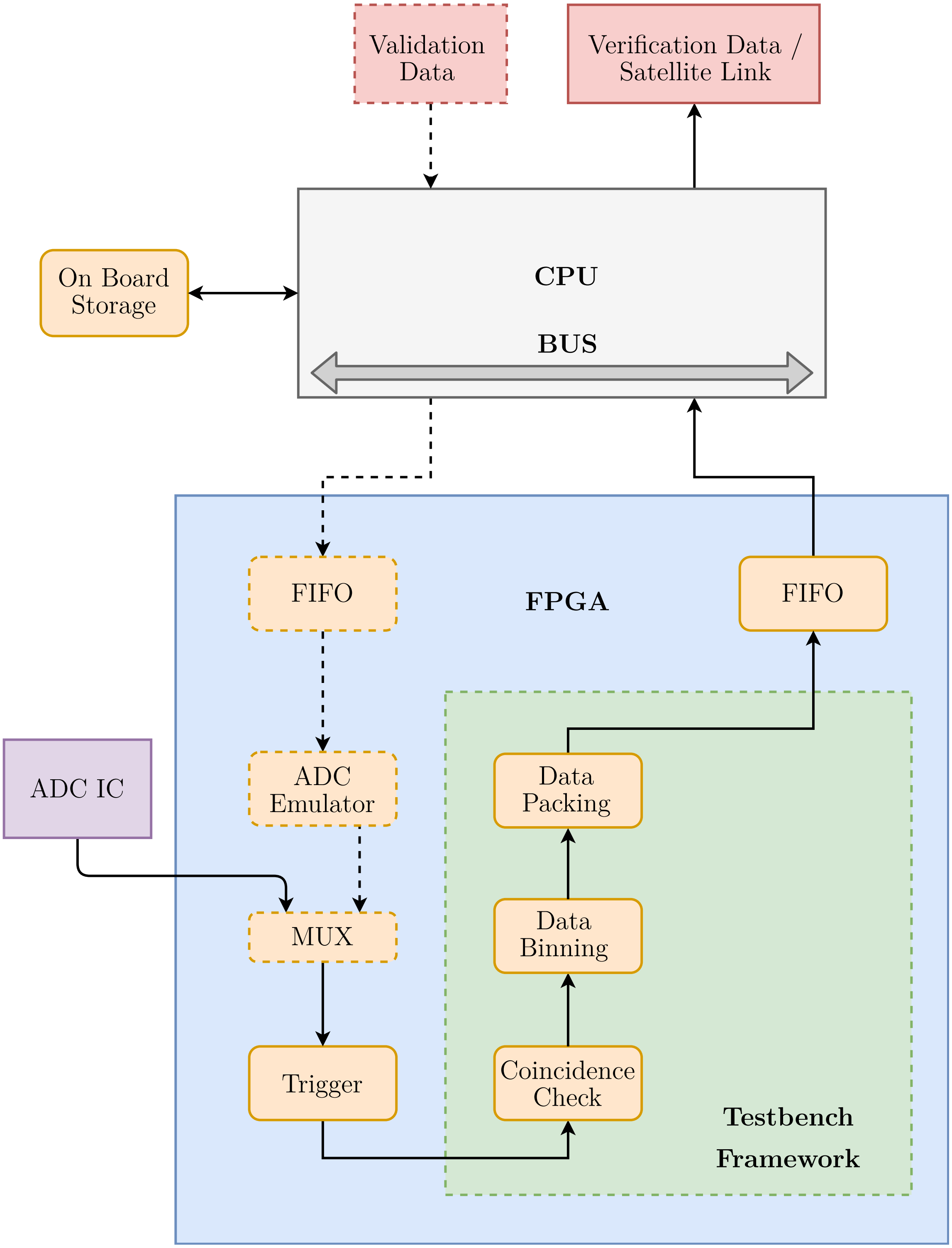

Figure 7.17: Block diagram of the proposed test system for the back-end electronics.

7.4.2 Testbench Framework

The testbench framework is a structured testbench architecture for verifying the VHDL code in the DSP. It is important to make this framework efficient and easy to use and maintain. Hence, Bitvis Universal VHDL Verification Methodology (UVVM) is used. Utilizing this testbench framework in the FPGA design will speed up the verification process considerably. For more information about Bitvis UVVM, see [39]. The verification process is made as automated as possible using various scripts. The user only has to call one script inside the verification software, e.g. ModelSim. The test procedure is illustrated in 7.18 (adapted from [39]). Device under test is abbreviated DUT.

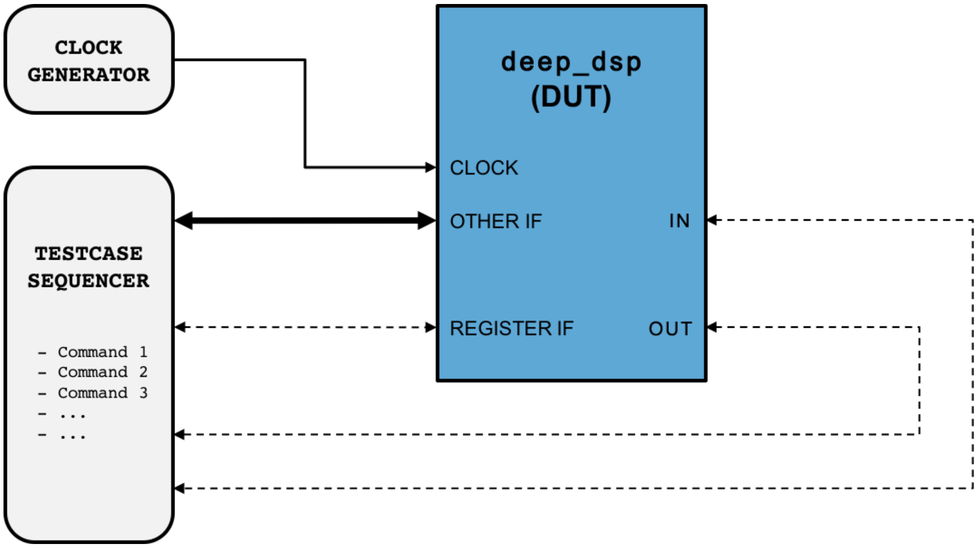

Figure 7.18: The deep_dsp in the testbench framework environment.

A simple device with parallel input and output was created (deep_dsp.vhdl), and a testbench (deep_dsp_tb.vhdl) for this device was designed and implemented. The tests that were created for this device was checking the default values (command 1), before enabling the device (2), and after a while checking the expected values on the output (3). Followed by clearing the device (4) and checking the output again (5). Then values was set on the input (6), and the expected value on the output was checked (7). The device was cleared again (8), and the output checked (9). Creating additional extensive tests is easily manageable within this framework. For more information about the testbench_framework repository see appendix E.

7.5 Back-end Electronics Summary

The design of the main DSP functions mentioned so far (coincidence check, data binning and data packet) has been specified. The coincidence check provides solutions to the electron scattering problem indicated in the GATE simulations. Various data bins has been specified based on different bit precisions. The data packet for the DEEP instrument has been specified as well. Based on the satellite link specifications, which is unclear at this point, a decision on how many energy bins to be used, must be made. As different payload data sizes with varying energy bins is already pre-calculated, this decision can easily be done.

To be able to test the strengths and weaknesses of the implementation of DSP functions a test system is proposed. A SoC configuration system that inputs validation data, processes it in the FPGA and compares it afterwards is proposed. A structured testbench architecture for verifying VHDL code is designed and implemented as well.

CHAPTER 8

Discussion and Conclusion

This chapter evaluates the results discussed in chapter 6 and the solutions proposed in chapter 7. It offers an outline of the topics that needs to be addressed in the future to create a complete working instrument.

8.1 Conclusion

This thesis has presented design solutions for the three main DSP functions needed for the DEEP instrument. The solutions are based on extensive GATE simulations. Two potential physics lists; emstandard_opt4 and emstandardSS were found to be suitable. Studies indicated that emstandard_opt4 physics list was the best option, and hence the emstandard_opt4 was used for the DEEP simulation setups. A total of 10 GATE simulation geometries were designed, where 7 of those were distinct DEEP relevant geometries. For each geometry 7 simulations were conducted with energies ranging between 30 to 1920 keV. It was found that scattering, out of a pixel, increases with energy of the incoming electron. At low energies the scattering to other pixels was negligible, involving 2 to 5 percent of incoming electrons. At higher energies this percentages increased to a maximum of 92 % at 1920 keV. At 960 keV it was 42 %, and at 480 keV it was 12 %.

Information regarding scattering was crucial for the design of the coincidence check. Without this information, the DEEP instrument will not be capable of determining which pixel is hit first, if more than one pixel shows a hit in the given sampling interval. The DEEP simulation setups gives overall beneficial information in further work with the detector design, especially in regard to the detector house.

Based on the DEEP simulation results the DSP function coincidence check has been specified. In addition, an innovative solution to manage the scattering out of a pixel, especially at higher energies, is proposed. By masking the pixels mechanically the scattering is managed before the back-end electronics is involved. Masking will also contribute to a reduction in overall processing power needed, as an alternative option was to use 13 additional super pixels. An optimum solution combining a wolfram-mask with two super pixels is proposed. The solution balances the advantages and disadvantages of these two alternatives. The active sensor area is 114 mm^2, which is a factor 1.4 reduction.

By employing a 1 mm wide, 2.5 mm thick wolfram-mask, a reduction of scattering into an adjacent pixel is achieved. The largest improvement of 75 % (factor 3.94 reduction) was achieved at 960 keV. Improvement was achieved at 480 and 1920 keV as well, with 65 % (factor 2.85 reduction) and 55 % (factor 2.23 reduction). Improvement is expected at all energies below 240 keV. By adjusting the width and the thickness of the mask further, reduction in scattering can be achieved, but at the expense of the active sensor area.

The two other DSP functions; data binning and data packet have been specified as well. Architecture of the data binning is designed and various bit precisions are proposed. A structured packet with five bit hamming code to each bin is proposed as part of the packet definition. The total data generation for the DEEP instrument is 47 Mbit/orbit with the optimum solution, constant bin size and 7 energy channels. Based on the satellite link specifications the number of energy channels can be adjusted and the pre-calculated payload data sizes will aid in this process.

To verify the behaviour of the DSP functions a SoC configuration test system is proposed. Reusing an existing design reduces the time spent on development. A structured testbench framework architecture for verifying VHDL code is designed and implemented as well. The framework is efficient and easy to use and maintain.

The lack of GATE simulation documentation resulted in the creation of the GATE simulation guide. The guide will ease the effort for new project members to familiarize themselves with GATE simulations. In addition, the guide is structured in such a manner that it can serve as a simulation guide for users without prior knowledge to GATE. The guide provides introduction to GATE, guides the user through the installation process and describes how to set-up their first GATE simulation.

Detailed and thorough documentation in all the steps of the GATE simulation development process, as well as the testbench framework, was achieved by employing a version control system, Git. The DEEP Git repository will be useful for further development with the DEEP instrument.

8.2 Future Work

There are many tasks that must be addressed before a fully functional DEEP instrument readout system is realized. The three main DSP functions, coincidence check, data binning and data packet must be fully implemented and tested. It is recommended to study and utilize the test system being developed at University of Bergen, as reusing an existing design reduces the time spent on development. The VHDL testbench framework implemented will contribute to a simpler testing process.

The SoC configuration and the FPGA to be utilized on the satellite must be studied even further, and a decision must be made. However, two suitable FPGAs for this task are already proposed, and it is recommended to start with the Microsemi SmartFusion2.

By simulating all the energies for the *Baffle* setup and comparing the results with the *Wide* setup results, useful information regarding baffle design can be obtained. The *Wide* simulation showed that it is necessary to reduce backscattering in the detector house to prevent contamination of the measurements, and this can be achieved by employing baffles.

As part of the overall detector design the pinhole size, which ultimately decides how many particles hit the sensor pixels, must be studied further. The front-end electronics specifications will be a factor to consider when deciding this size. In addition simulation with various detector house configurations must be conducted. As this will indicate how well the detector house is able to stop background radiation from penetrating the detector house and contaminating the measurements.

APPENDIX A

GATE Simulation Guide

This chapter will give an introduction to GEANT4 Application for Emission Tomography (GATE) simulations with a focus on the DEEP simulation setup. Both introduction to the installation procedure and how to get started with a simulation is covered. Information is based on [40] and [41].

A.1 Introduction

GATE is a Monte Carlo simulation platform developed by the OpenGATE collaboration since 2001, first publicly released in 2004. Configuration of the various experimental settings is done by an easy-to-learn macro mechanism. Both simple and highly sophisticated experimental settings are available. Since 2004, new versions has been frequently released with new enhanced features to the platform. All upgrades have been well-validated to stay consistent with regular GEometry ANd Tracking 4 (GEANT4) public releases. Some of the major enhancements since the initial release is the additional options for speeding up simulations, and optical physics models for accurate modelling of the detector response. GATE supports various simulations such as: Computed Tomography (CT), Optical Imaging (Bioluminescence and Fluorescence), Positron Emission Tomography (PET), Radiotherapy and Dosimetry and Single Photon Emission Computed Tomography (SPECT).

A.2 Installation

The newest available GATE version was 8.1. The required dependencies for this version is GEANT4 version 10.3 or 10.4, and ROOT version 6 [42]. For the installation setup it is also required that GNU Compiler Collection (GCC) must be between version 6.0-7.3. For the same setup a minimal version of CMake is also required, and the version must be at least 3.3 with Secure Socket Layer, SSL support. Version 3.10.2 is used. As specified in the release notes of GEANT4, the supported Class Library for High Energy Physics (CLHEP) version is 2.4.0.0, and use of a different version may cause incorrect simulation results [43]. Version 2.4.0.4 were chosen as it was the newest and had bug fixes for version 2.4.0.0.

The software and version all GATE simulations are computed on, is documented in table A.1 and the hardware in table A.2. The newest possible version for all software were chosen.

Item	Version
GATE	8.1
GEANT4	10.04 Patch 1
CLHEP	2.4.0.4
ROOT	6.13/02

Table A.1: Software and associated versions that all GATE simulations are computed on.

Item	Details
OS	Ubuntu 18.04 LTS
CPU	Intel(R) Core(TM) i7-3610QM @ 2.30 GHz
RAM	Micron Technology DDR3 8 GB @ 1600 MHz
SSD	Samsung PM83 256 GB

Table A.2: Hardware all GATE simulations are computed on.

Over the next subsections, a guide to installation the required software will be given. This software is CLHEP 2.4.0.4, ROOT 6.13/02, GEANT4 10.04 Patch 1 and GATE 8.1. Depending on the operating system used, different libraries is required as well. Usually the libraries given below is sufficient. If any libraries are missing the installation to the given software will fail, and an error message will tell which library is missing. The user should install the missing library and start the installation procedure once more. The library installation is the most inconvenient part of the installation procedure. Every "/PATH_TO/" must be changed with the actual path to that directory.

Minimum required packages and libraries:

```
sudo apt-get install cmake cmake-curses-gui
build-essential libqt4-opengl-dev qt4-qmake libqt4-dev
libx11-dev libxmu-dev libxpm-dev libxft-dev
```

A.2.1 CLHEP 2.4.0.4

CLHEP can be downloaded at the following address:

```
http://proj-clhep.web.cern.ch/proj-clhep/clhep23.html
```

Start with unzip/untar the downloaded file and, in the same directory, create two new directories to build and install:

```
mkdir 2.4.0.4-build
mkdir 2.4.0.4-install
```

Move into the build directory:

```
cd 2.4.0.4-build
```

Starting the actual installation by calling CMake:

```
cmake -DCMAKE_INSTALL_PREFIX=/PATH_TO/2.4.0.4-install
/PATH_TO/2.4.0.4/CLHEP/
```

And then Make as follows:

```
make -jN (N is the number of processors available)
make install
```

Finally, update the environment variables:

```
export PATH=$PATH:/PATH_TO/2.4.0.4/-install/bin
:/PATH_TO/2.4.0.4-install/include

export LD_LIBRARY_PATH=$LD_LIBRARY_PATH
:/PATH_TO/2.4.0.4-install/lib
```

A.2.2 ROOT 6.13/02

ROOT can be downloaded at the following address:

```
https://root.cern.ch/downloading-root
```

Start with unzip/untar the downloaded file and, in the same directory, create two new directories to build and install:

```
mkdir root_v6.13.02-build
mkdir root_v6.13.02-install
```

Move into the build directory:

```
cd root_v6.13.02-build
```

Starting the actual installation by calling CMake:

```
cmake --build . --target install
cmake -DCMAKE_INSTALL_PREFIX=../root_v6.13.02-install/
-P cmake_install.cmake
```

And then Make as follows:

```
make -jN (N is the number of processors available)
make install
```

Finally, update the environment variables:

```
source /PATH_TO/root_v6.13.02-install/bin/thisroot.sh
```

A.2.3 GEANT4 10.04 Patch 1

Geant4 can be downloaded at the following address:

```
http://geant4.web.cern.ch/support/download
```

Start with unzip/untar the downloaded file and, in the same directory, create two new directories to build and install:

```
mkdir geant4.10.04.p01−build
mkdir geant4.10.04.p01−install
```

Move into the build directory:

```
cd geant4.10.04.p01−build
```

Run the CMake configuration interface as follows:

```
ccmake ../geant4.10.04.p01
```

Fill in the necessary "/PATH_TO/" CLHEP and ROOT variables. Required variable settings:

- GEANT4_INSTALL_DATA ON
- GEANT4_USE_OPENGL_X11 ON
- GEANT4_USE_QT ON

Press "c" to configure, and "g" to generate the compilation environment.

Starting the actual installation by calling Make as follows:

```
make −jN (N is the number of processors available)
make install
```

Finally, update the environment variables:

```
source /PATH_TO/geant4.10.04.p01−install/bin/geant4.sh
```

A.2.4 GATE 8.1

GATE can be downloaded at the following address:

```
http://www.opengatecollaboration.org/node/82
```

Start with unzip/untar the downloaded file and, in the same directory, create two new directories to build and install:

```
mkdir gate_v8.1-build
mkdir gate_v8.1-install
```

Move into the build directory:

```
cd gate_v8.1-build
```

Run the CMake configuration interface as follows:

```
ccmake ../gate_v8.1
```

Fill in the necessary "/PATH_TO/" CLHEP, ROOT, and GEANT4 variables. Required variable settings:

- BUILD_TESTING ON
- GATE_DOWNLOAD_BENCHMARK_DATA ON
- GATE_USE_GEANT4_UIVIS
- GATE_USE_STDC11 ON

Press "c" to configure, and "g" to generate the compilation environment.

Starting the actual installation by calling Make as follows:

```
make -jN (N is the number of processors available)
make install
```

Finally, update the environment variables:

```
export PATH=$PATH:/PATH_TO/gate_v8.1-install/bin
```

A.2.5 Configuration of the Linux environment

Configure the "your_file.bashrc" file to set up all the environment variables which is mandatory to perform a GATE simulation. This is achieved by adding the following lines to the file:

```
# User specified for GATE simulation:
export PATH=$PATH:/PATH_TO/2.4.0.4-install/bin
export LD_LIBRARY_PATH=$LD_LIBRARY_PATH
:/PATH_TO/2.4.0.4-install/lib

source /PATH_TO/root_v6.13.02-install/bin/thisroot.sh
source /PATH_TO/geant4.10.04.p01-install/bin/geant4.sh
export PATH=$PATH:/PATH_TO/gate_v8.1-install/bin
```

A.3 Installation Validation

GATE come with an optional test to validate the installation. However, some prior adjustments must be made in CMake configuration. The required settings are:

- GATE_USE_ECAT7 ON
- GATE_USE_OPTICAL ON

ECAT7 can be downloaded at the following address:

```
http://www.opengatecollaboration.org/ECAT
```

To automatically start the validation call:

```
make test
```

The output should look something like this:

```
Running tests...
Test project /PATH_TO/gate_v8.1-build
Start 1: benchRT_gamma
1/7 Test #1: benchRT_gamma ...........   Passed   14.30 sec
Start 2: benchRT_proton
2/7 Test #2: benchRT_proton ..........   Passed    1.32 sec
Start 3: benchRT_carbon
3/7 Test #3: benchRT_carbon ..........   Passed    5.12 sec
Start 4: benchImaging_ct
4/7 Test #4: benchImaging_ct .........   Passed   33.54 sec
Start 5: benchImaging_optical
5/7 Test #5: benchImaging_optical ....   Passed    3.02 sec
Start 6: benchImaging_spect
6/7 Test #6: benchImaging_spect .......  Passed   25.89 sec
Start 7: benchImaging_pet
7/7 Test #7: benchImaging_pet ........   Passed   12.15 sec
100% tests passed, 0 tests failed out of 7
Total Test time (real) = 95.34 sec
```

To manually start one of the tests, the user can for instance call:

```
./gate_run_test.sh benchRT gamma
```

A.4 Getting started

For each typical GATE simulation the user must:

1. Define visualization elements (Optional).
2. Define material database.
3. Define the scanner geometry.
4. Set up the detector model.
5. Set up the physics processes.
6. Initialize the simulations.
7. Define the source.
8. Specify the data output format.
9. Start the acquisition.

Figure A.1 illustrates a simple GATE simulation geometry. The simulations consist of a blue layer of silicon with dimensions 15×15×1 mm, consisting of 3×3 pixels. It is the silicon that is the actual detector. The pink square illustrates a particle source translated 20 cm in the Z-axis from the silicon layer. The grey lines illustrate the world in which the whole simulation takes place. It is only interactions inside the world that can be kept a record on.

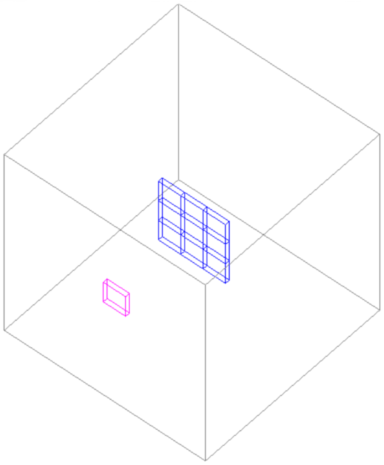

Figure A.1: Visualization of a possible GATE simulation geometry.

A.4.1 Visualization Elements

The first step which is optional, is to define the visualization elements which gives the users the ability to visualize the geometry of the simulation. This step will visually confirm that the geometry is set up correctly. To visualize the simulation geometry:

```
Gate --qt
```

Followed by opening the mac/DEEP_GATE.mac file.

The visualization parameters which produced the illustration in figure 5.13 is:

```
/vis/open                                      OGLSQt
/vis/viewer/zoom                               1
/vis/viewer/set/viewpointThetaPhi              120 120
/vis/viewer/set/style                          surface
/tracking/storeTrajectory                      1
/vis/scene/endOfEventAction accumulate         25000
/vis/drawVolume
/vis/viewer/update
/vis/viewer/refresh
```

The parameters for the "viewpointThetaPhi" can be edited to visualize other viewing angles as desired.

A.4.2 Material Database

The second step is to define a material database for the materials used in the simulation. For each element the user must specify the density, atomic weight and which state the element is in. The DEEP simulation consists of four materials. The definition of these materials are listed in table A.3.

Element	Density [g/cm^3]	Atomic weight [g/mole]	State
Aluminium	2.7	26.98	Solid
Silicon	2.33	28.09	Solid
Vacuum	1e-9	N/A	N/A
Wolfram	19.3	183.84	Solid

Table A.3: Material definition of the elements involved in the simulation.

The material definition is saved in a material database named "GateMaterials.db". Material database is defined as:

```
/gate/geometry/setMaterialDatabase GateMaterials.db
```

A.4.3 Scanner Geometry

The third step is to define the scanner geometry. The user must define the geometry of the simulation based on volumes. All volumes are linked together following a tree structure where each branch represents a volume. Each volume is characterized by shape, size, position, and material composition. The default material assigned to a new volume is Air.

The world volume is the base of the tree and it is the experimental environment of the simulation. The world volume is a box centred at the origin and can be of any size, but it has to be large enough to include the entire simulation geometry. The tracking of any particle stops when it escapes from the world volume. The world contains one or more sub volumes referred to as daughter volumes. The name of the first daughter of the world has a specific meaning and name. It specifies the type of scanner to be simulated.

The world, which should be large enough to include the DEEP geometry and its simulation elements is defined as a box with dimensions 45×45×45 mm. The material of the world volume is set to vacuum. A visualization of the world can be seen in figure 5.13 as the grey lined square.

World is defined as:

```
/gate/world/geometry/setXLength         45. mm
/gate/world/geometry/setYLength         45. mm
/gate/world/geometry/setZLength         45. mm
/gate/world/setMaterial                 Vacuum
/gate/world/vis/setColor                gray
/gate/world/vis/forceWireframe          1
/gate/world/vis/setVisible              1
```

The “scanner” is the first daughter volume. The name itself describe the purpose of this daughter volume, it is a scanner. The scanner is a box with dimensions of 15×15×2.4 mm. In this volume the DEEP instrument geometry will be defined.

Scanner is defined as:

```
/gate/world/daughters/name              scanner
/gate/world/daughters/insert            box
/gate/scanner/geometry/setXLength       15. mm
/gate/scanner/geometry/setYLength       15. mm
/gate/scanner/geometry/setZLength       2.4 mm
```

A.4.4 Instrument Geometry

The fourth step is to set up the geometry for the given instrument. The definition of a geometry is a key step in designing a simulation, because it is through the geometry definition that the imaging device and object to be scanned are described. Particles are then tracked through the components of the geometry. The geometry set up is where GATE has the advantage over GEANT4, but also its disadvantage. In GATE it is easy to set up simple geometries, but on the other hand, only simple geometries are possible. In GATE "setTranslation" is used to move geometry in X, Y and Z directions. To achieve desired geometry with 1 mm thick silicon layer, then 0.4 mm vacuum, and another 1 mm thick silicon layer, both front and back layer is moved in opposite directions from the centre.

SiFront layer is defined as:

```
/gate/scanner/daughters/name                  SiFront
/gate/scanner/daughters/insert                box
/gate/SiFront/geometry/setXLength             15. mm
/gate/SiFront/geometry/setYLength             15. mm
/gate/SiFront/geometry/setZLength             1. mm
/gate/SiFront/placement/setTranslation        0 0 −0.7 mm
/gate/SiFront/setMaterial                     Silicon
/gate/SiFront/vis/setColor                    yellow
/gate/SiFront/vis/forceWireframe              1
/gate/SiFront/vis/setVisible                  1
```

SiBack layer is defined as:

```
/gate/scanner/daughters/name                  SiBack
/gate/scanner/daughters/insert                box
/gate/SiBack/geometry/setXLength              15. mm
/gate/SiBack/geometry/setYLength              15. mm
/gate/SiBack/geometry/setZLength              1. mm
/gate/SiBack/placement/setTranslation         0 0 0.7 mm
/gate/SiBack/setMaterial                      Silicon
/gate/SiBack/vis/setColor                     yellow
/gate/SiBack/vis/forceWireframe               1
/gate/SiBack/vis/setVisible                   1
```

All layers must now be attached to the scanner:

```
/gate/SiFront/attachCrystalSD
/gate/SiBack/attachCrystalSD
```

A phantom source is created to make the placement of the source easier. The phantom is easily moved around in the world volume. The source will be attached to the phantom source. The phantom has dimensions of 5×5×1 mm, and translated -19.5 mm along the Z-axis. This will result in that the particles from the source has travelled roughly 2 cm before they hit the detector. This is to make the simulation as real life relevant as possible. The material is set to be vacuum so that it will not interfere with the simulation.

Phantom source is defined as:

```
/gate/world/daughters/name                    pSource
/gate/world/daughters/insert                  box
/gate/pSource/geometry/setXLength             5 mm
/gate/pSource/geometry/setYLength             5 mm
/gate/pSource/geometry/setZLength             1 mm
/gate/pSource/placement/setTranslation        0. 0. -19.5 mm
/gate/pSource/placement/setRotationAxis       1 0 0
/gate/pSource/placement/setRotationAngle      180 deg
/gate/pSource/setMaterial                     Vacuum
/gate/pSource/vis/setColor                    green
/gate/pSource/vis/forceWireframe              1
/gate/pSource/vis/setVisible                  1
```

A.4.5 Physics Processes

The fifth step is the physics processes, and once the volumes and corresponding sensitive detectors are described, the interaction processes of interest in the simulation must be specified. GATE uses the GEANT4 models for physical processes and the user has to choose among these processes for each particle.

A user can construct his own physics list, use one of the physics lists provided by GEANT4 or modify any of the offered physics lists. To decide which physics list to be used in the DEEP simulation, the most relevant ones must be validated first. Validating the physics list is important as different lists are made for different applications. A physics list is usually made for distinct applications. Assume a physics list is made for application X, but the user changes parameters such as energy, primary particles and/or material, the results from this new application Y may give inaccurate simulation results.

The two most promising physics list for the DEEP simulation is:

- emstandard_opt4
- emstandardSS (QGSP_BIC___SS)

Physics list is defined as:

```
/gate/physics/addPhysicsList emstandard_opt4
```

A.4.6 Initialization

The sixth step is to initialize the simulations. The initialization triggers the calculation of the cross section tables. After this step, the physics list cannot be further modified and new volumes cannot be inserted into the geometry. The initialization is accomplished by writing:

```
/gate/run/initialize
```

A.4.7 Source

The seventh step is to define a source. In GATE, a source is represented by a volume in which the particles (gamma, ion, proton, electron, positron, etc.) are emitted. The user can define the geometry of the source and its characteristics such as the direction of emission, the energy distribution, the activity and the lifetime of unstable sources.

The source is defined as a uniform monoenergetic electron beam. It is attached to the phantom source, and the direction is set to beam electrons onto the middle pixel of the detector. The beam is a general particle source with particles consisting of only electrons. These electrons will be monoenergetic for each simulation. The distribution of the beam is unidirectional. The source will emit a beam parallel to the detector. There are two variables included in the source, these are "energy" and "particles". These variables will make it easier to set up new simulations faster. To start a new simulation with different energy and or primary particles one just need to include those variables in the command line. The pink square in figure 5.13 is a visualization of the source.

Source is defined as:

```
/gate/source/addSource                          uniformBeam gps
/gate/source/uniformBeam/gps/particle           e-
/gate/source/uniformBeam/gps/energytype         Mono
/gate/source/uniformBeam/gps/monoenergy         {energy} keV
/gate/source/uniformBeam/gps/type               Beam
/gate/source/uniformBeam/gps/shape              Square
/gate/source/uniformBeam/gps/pos/centre         0 0 0 mm
/gate/source/uniformBeam/gps/direction          0 0 1
/gate/source/uniformBeam/gps/halfx              2.5 mm
/gate/source/uniformBeam/gps/halfy              2.5 mm
/gate/source/uniformBeam/gps/centre             0. 0. 0. mm
/gate/source/uniformBeam/gps/angtype            iso
/gate/source/uniformBeam/gps/mintheta           0 deg
/gate/source/uniformBeam/gps/maxtheta           0 deg
/gate/source/uniformBeam/gps/minphi             0 deg
/gate/source/uniformBeam/gps/maxphi             360 deg
/gate/source/uniformBeam/attachTo               pSource
/gate/application/setTotalNumberOfPrimaries     {particles}
/gate/source/uniformBeam/visualize              25000 green 1
```

A.4.8 Data Output Format

The eight step is to define the data output. By default, the data output formats for all systems used by GATE are ASCII and ROOT. To write on a disk is the slowest operation in GATE and it is recommended that if the user does not need ASCII files, it should be disabled. Output as ASCII is not compressed either, making the files very large. Based on this, the data output format is defined as a ROOT file. The file is named "DEEP_OUTPUT.root" and saved in the "Output" folder. In ROOT there are many trees, such as "Hits", "Singles", "Ntuple", etc., and the ones of no interest can be disabled to save file size. It will only be the tree "Hits" that will be used further in the readout, which means everything else is disabled. Output is defined as:

```
/gate/output/root/enable
/gate/output/root/setFileName Output/DEEP_OUTPUT
/gate/output/root/setRootHitFlag 1
/gate/output/root/setRootSinglesFlag 0
/gate/output/root/setRootNtupleFlag 0
/gate/output/verbose 2
```

A.4.9 Acquisition

The ninth and final step, is where the acquisition is defined. The choice of the generator seed is also important. There are three options:

1. Default option. In this case the default CLHEP seed is taken. This seed is always the same.
2. Auto option. In this case, a new seed is automatically generated each time GATE is run. To randomly generate the seed, the time in millisecond since January 1, 1970 and the process ID of the GATE instance (i.e. the system ID of the running GATE process) are used. So that each time GATE is run, a new seed is used.
3. Manual option. In this case, the user can manually set the seed. The seed is an unsigned integer value and it is recommended to be included in the interval [0,900000000].

As a Monte Carlo tool, GATE needs a random generator. The CLHEP libraries provide various ones. Three different random engines are currently available in GATE, the Ranlux64, the James Random and the Mersenne Twister. The default one is the Mersenne Twister. The level of verbosity of the random engine can be chosen as well. The verbosity is the level of detailed information regarding the random engine status printed to terminal while running the simulation.

Before the acquisition is started the random engine is defined as Mersenne Twister and the seed is set to auto, which mean a random seed is chosen. In chapter 5.2 when validating physics lists, the same seed is chosen for both lists. Initially GATE simulations were based on James Random algorithm, but this generator is now 28 years old and has poor statistical properties. Mersenne Twister on the other hand is a more recent pseudo-random number generator, and is much better statistical as well as much faster, and therefore it is the best choice. This is achieved by:

```
/gate/random/setEngineName MersenneTwister
/gate/random/setEngineSeed auto
/gate/application/start
```

The simulation is then finally started by calling:

```
Gate DEEP_GATE.mac -a '[energy,X] [particles,Y]'
```

Where X is energy in keV, and Y is number of particles.

APPENDIX B

Data Extraction and Processing

As GATE creates a ROOT file with a lot of different information, the data extraction and processing will gather the necessary data and present them in a new and more applicable matter. This is achieved by writing a custom program, named DEEP_READOUT.C. One of the features in this program is the creation of the desired pixels.

B.1 Readout Process

The custom program named DEEP_READOUT.C is written in C. It will handle the readout from the ROOT-file and generate new data file named DEEP_OUTPUT.csv. The file type of the output file is set as a Comma-Separated Values (CSV) file. Each line is a record and the values are separated with a comma. Even though the file type is not standardized, it is commonly used as a data exchange format and can be processed by almost all existing applications. Using the CSV file type will make it more manageable to transfer the data between programs. It is simple to implement and parse, as well as it being fast to handle and small in size.

The readout process will first open output file (Output/DEEP_OUTPUT.csv), and set the header. Further, it will initialize ROOT with all the necessary variables and start to loop through all data in the ROOT-file. It will get event ID, X and Y position for the first interaction of particles and output status to terminal. It will check XYZ-coordinates and calculate the pixel energy for that event. At the end of each event it will write the calculated data for the event into the output file. Temporary memory is cleared (set to zero) before next event. When the last event ID has been calculated, a simulation report is printed to the terminal. Finally, it will close the output file and clean up temporary memory in ROOT.

The simulation report gives information about the computation time of the simulation, as well as absorbed energy in the front and back layer. Unresolved energy is the energy that is absorbed in the silicon, but the pixel could not be determined, however the rate this error occurs is negligible. Below is an example of a simulation report, from the simulation setup 1, with electrons with energy of 960 keV.

```
Simulation Time: 1743 s


=====================================================================
==                      Simulation Report                          ==
=====================================================================
Absorbed energy in front pixels:              70673240 keV
Absorbed energy in back pixels:               19409250 keV
Total Absorbed energy in pixels (f+b):        90422840 keV

Total unresolved energy in pixels:            1353 keV
Total energy absorbed in Si:                  89948672 keV
=====================================================================
```

B.2 Functions

Explanation of all the DEEP_READOUT.C functions is given below.

ReadOut() is the main program. It loops through all data from the ROOT-file and output the desired data in the DEEP_OUTPUT.csv file. The code below illustrates how to initialize and loop through and get the necessary information from the ROOT-file is achieved:

```
TFile* fr = new TFile("Output/DEEP_OUTPUT.root");
TTree* htree = (TTree*)f1->Get("Hits");

for (int i=0; i<htree->GetEntries(); ++i) {
htree->GetEntry(i);
... rest of code ...
}
```

This process can take some time depending on the number of total particles and/or particle collisions. That is why the event ID that is currently calculated is printed to terminal, so the progress of the readout can be monitored.

GetEntries() read the number of entries in the "tree" and returns the number of entries matching the selection. For more information see [44].

GetEntry() reads an entry, and returns the number of bytes read. For more information see [44].

calculatePixelEnergy() creates the pixels. It is achieved by first checking if the deposited energy is between the front or the back pixels. Thereafter checking if the energy is between pixel 1-3, 4-6 etc. and then allocating the deposited energy to that associated pixel.

calculateTotalEnergy() sums up all the energy for each event. This gives the total absorbed energy for each event.

openOutputFile() opens the output file and creates it if necessary. The header is also set in this process.

writeToOutputFile() writes the calculated data to the output file. The data is written to the output file for each event.

printToTerminal() creates a simulation report. The simulation report consists of calculating the absorbed energy in the front pixels, back pixels and a total absorbed energy in the silicon.

clearMemory sets the values of the pixel array, and total energy to zero before next event begins.

B.3 Starting the Data Extraction Process

A macro is made to make the readout as simple as possible. To start the data extraction process the user needs to call:

```
root −q −b src/DEEP_ROOT_MACRO.cxx
```

The macro will ensure that the DEEP_READOUT.C is compiled, and the ReadOut() is started.

APPENDIX C

Detailed GATE Simulation Results

In this chapter detailed information about simulation setup 1 and 2 is presented. Every simulation had a monoenergetic electron beam. The energies that were simulated are 30, 60, 120, 240, 480, 960 and 1920 keV. These energies corresponds to the lower energy threshold of the integral energy channels used in the data binning, see chapter 7.2. A total of 1×10^5 particles were simulated for each energy. A total of 1×10^5 particles were simulated for each energy. For more information about the setups see chapter 5, and for overview of the results see chapter 6.

The results consists of absorbed energy and scattering in each pixel, as well as total energy distribution in percentage. Results also provides plots with energy distribution in the front and the back layer. For more results, and detailed information regarding energy distribution for each pixel see the "gate_simulation" repository. Information about this repository can be found in appendix D. Average energy deposited by each incoming electron is abbreviated E/e$^-$. For simplicity, total absorbed energy is abbreviated TAE and the number of scatterings is abbreviated SCT.

C.1 Simulation Setup 1

Information about this setup can be found in chapter 5.4.1.

C.1.1 Electron - 30 KeV

Pixel	SCT	TAE [keV]	E/e$^-$ [keV]	TAE [%]
P1	0	0	0	0.0
P2	25	535	21	0.0
P3	0	0	0	0.0
P4	23	440	19	0.0
P5	N/A	2.673×10^6	27	89.1
P6	12	154	13	0.0
P7	0	0	0	0.0
P8	21	397	19	0.0
P9	0	0	0	0.0
P10	0	0	0	0.0
P11	1	19	19	0.0
P12	0	0	0	0.0
P13	0	0	0	0.0
P14	0	0	0	0.0
P15	0	0	0	0.0
P16	0	0	0	0.0
P17	0	0	0	0.0
P18	0	0	0	0.0

Table C.1: Electrons with energy equal to 30 keV.

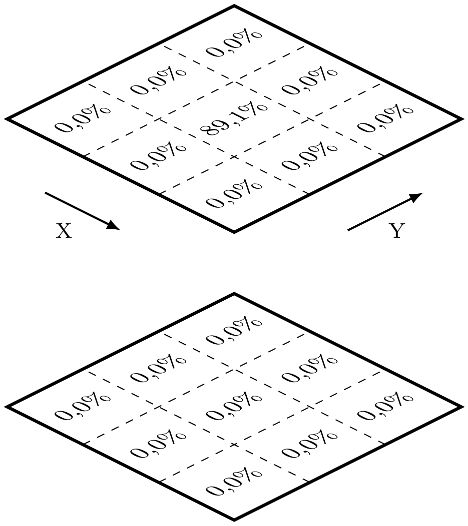

Figure C.1: Total energy distribution in percentage for 30 keV electrons.

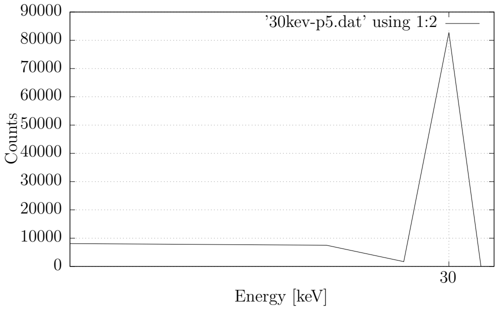

Figure C.2: Energy distribution in pixel 5 with 30 keV.

C.1.2 Electron - 60 KeV

Pixel	SCT	TAE [keV]	E/e^- [keV]	TAE [%]
P1	1	0	0	0.0
P2	88	3120	36	0.1
P3	0	0	0	0.0
P4	82	2883	35	0.1
P5	N/A	5.386×10^6	54	89.8
P6	95	3275	35	0.1
P7	0	0	0	0.0
P8	107	3861	36	0.1
P9	0	0	0	0.0
P10	0	0	0	0.0
P11	0	0	0	0.0
P12	0	0	0	0.0
P13	0	0	0	0.0
P14	1	22	22	0.0
P15	1	27	27	0.0
P16	0	0	0	0.0
P17	0	0	0	0.0
P18	1	22	22.0	0.0

Table C.2: Electrons with energy equal to 60 keV.

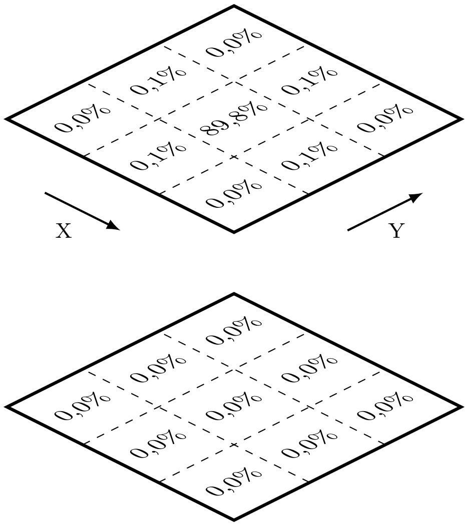

Figure C.3: Total energy distribution in percentage for 60 keV electrons.

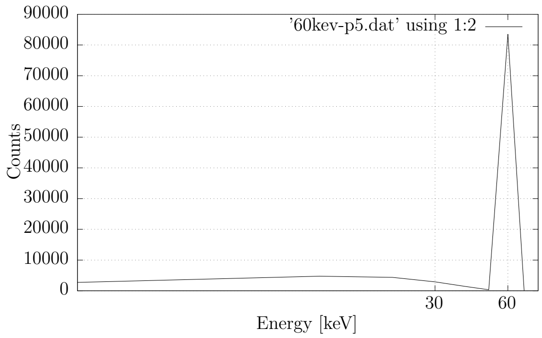

Figure C.4: Energy distribution in pixel 5 with 60 keV.

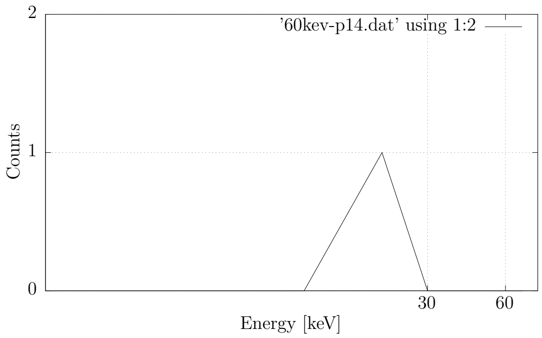

Figure C.5: Energy distribution in pixel 14 with 60 keV.

C.1.3 Electron - 120 KeV

Pixel	SCT	TAE [keV]	E/e- [keV]	TAE [%]
P1	0	0	0	0.0
P2	296	20.316×10^3	69	0.2
P3	2	111	56	0.0
P4	245	17.797×10^3	73	0.2
P5	N/A	10.796×10^6	108	90.0
P6	287	20.244×10^3	71	0.2
P7	1	44	44	0.0
P8	291	20.222×10^3	70	0.2
P9	6	250	42	0.0
P10	0	0	0	0.0
P11	2	72	36	0.0
P12	0	0	0	0.0
P13	1	34	34	0.0
P14	14	370	26	0.0
P15	3	67	22	0.0
P16	0	0	0	0.0
P17	5	173	35	0.0
P18	0	0	0	0.0

Table C.3: Electrons with energy equal to 120 keV.

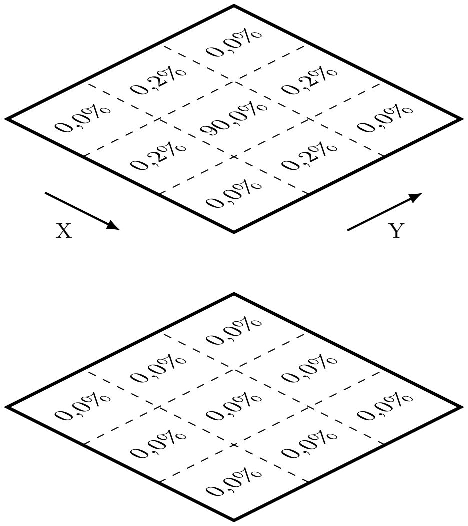

Figure C.6: Total energy distribution in percentage for 120 keV electrons.

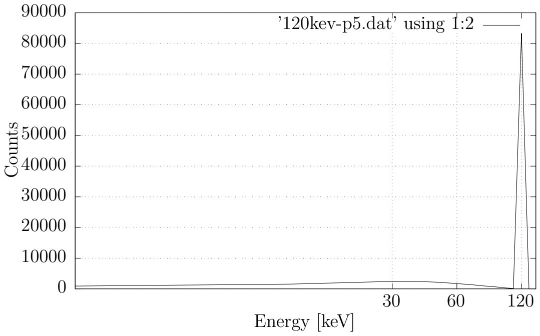

Figure C.7: Energy distribution in pixel 5 with 120 keV.

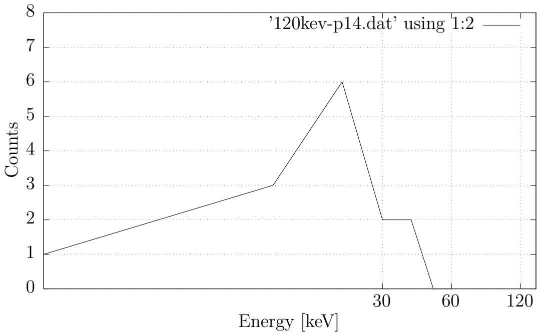

Figure C.8: Energy distribution in pixel 14 with 120 keV.

C.1.4 Electron - 240 KeV

Pixel	SCT	TAE [keV]	E/e$^-$ [keV]	TAE [%]
P1	9	756	84	0.0
P2	863	112.027×10^{3}	130	0.5
P3	12	844	70	0.0
P4	893	119.646×10^{3}	134	0.5
P5	N/A	21.487×10^{6}	215	89.5
P6	902	119.090×10^{3}	132	0.5
P7	12	956	80	0.0
P8	915	122.609×10^{3}	134	0.5
P9	11	878	80	0.0
P10	2	61	31	0.0
P11	7	169	24	0.0
P12	4	126	31	0.0
P13	3	122	41	0.0
P14	47	1199	26	0.0
P15	5	167	33	0.0
P16	0	0	0	0.0
P17	8	247	31	0.0
P18	3	110	37	0.0

Table C.4: Electrons with energy equal to 240 keV.

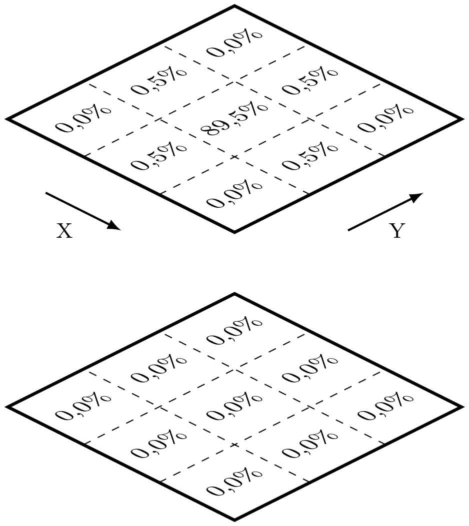

Figure C.9: Total energy distribution in percentage for 240 keV electrons.

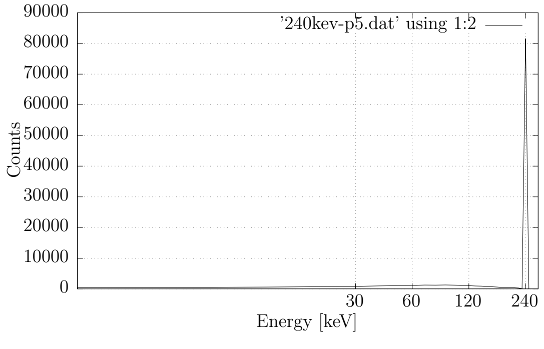

Figure C.10: Energy distribution in pixel 5 with 240 keV.

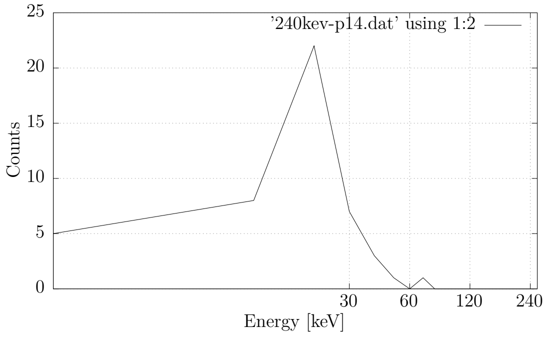

Figure C.11: Energy distribution in pixel 14 with 240 keV.

C.1.5 Electron - 480 KeV

Pixel	SCT	TAE [keV]	E/e$^-$ [keV]	TAE [%]
P1	65	11.774×10^3	181	0.0
P2	2485	637.955×10^3	257	1.3
P3	70	13.384×10^3	191	0.0
P4	2461	631.277×10^3	257	1.3
P5	N/A	41.905×10^3	419	87.3
P6	2467	643.346×10^3	261	1.3
P7	45	7.717×10^3	172	0.0
P8	2405	622.989×10^3	259	1.3
P9	64	10.286×10^3	161	0.0
P10	10	308	31	0.0
P11	23	865	38	0.0
P12	8	319	40	0.0
P13	24	734	31	0.0
P14	155	3.898×10^3	25	0.0
P15	24	587	25	0.0
P16	7	209	30	0.0
P17	20	744	37	0.0
P18	9	298	33	0.0

Table C.5: Electrons with energy equal to 480 keV.

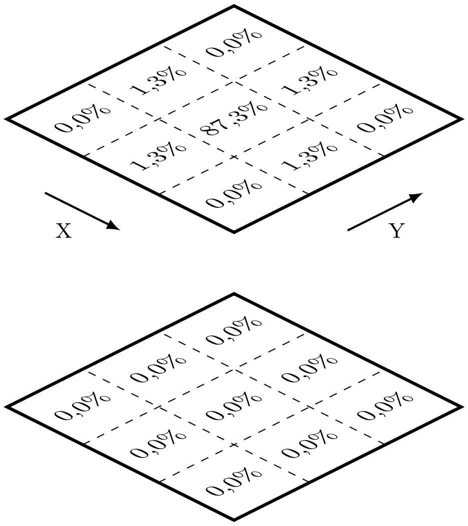

Figure C.12: Total energy distribution in percentage for 480 keV electrons.

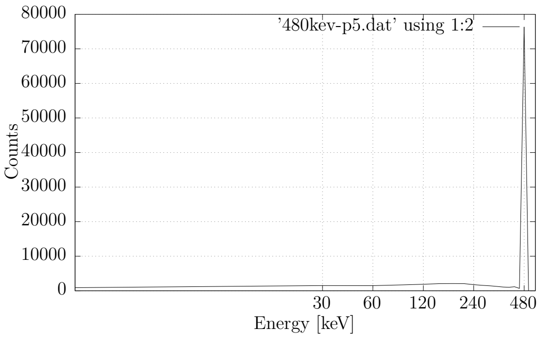

Figure C.13: Energy distribution in pixel 5 with 480 keV.

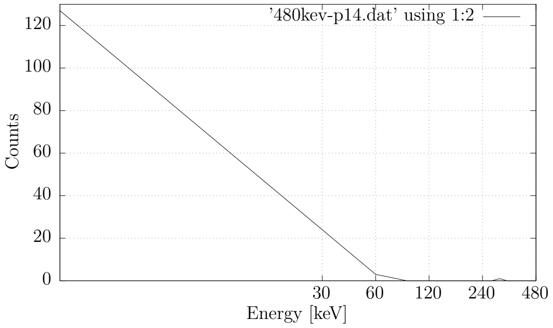

Figure C.14: Energy distribution in pixel 14 with 480 keV.

C.1.6 Electron - 960 KeV

Pixel	SCT	TAE [keV]	E/e^- [keV]	TAE [%]
P1	461	128.044×10^3	278	0.1
P2	6003	2.306×10^6	384	2.4
P3	476	128.399×10^3	270	0.1
P4	6010	2.353×10^6	392	2.4
P5	N/A	60826764	608	63.4
P6	5913	2.282×10^6	386	2.4
P7	490	137.599×10^3	281	0.1
P8	6033	2.327×10^6	386	2.4
P9	489	134.270×10^3	275	0.1
P10	369	78.871×10^3	214	0.1
P11	3473	1.044×10^6	301	1.1
P12	366	83.317×10^3	228	0.1
P13	3465	1.044×10^6	301	1.1
P14	39620	15.216×10^6	384	15.9
P15	3457	1.035×10^6	299	1.1
P16	389	87.813×10^3	226	0.1
P17	3463	1.032×10^6	298	1.1
P18	391	83.179×10^3	213	0.1

Table C.6: Electrons with energy equal to 960 keV.

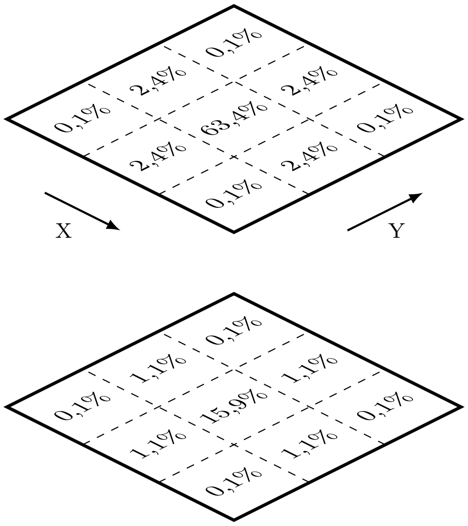

Figure C.15: Total energy distribution in percentage for 960 keV electrons.

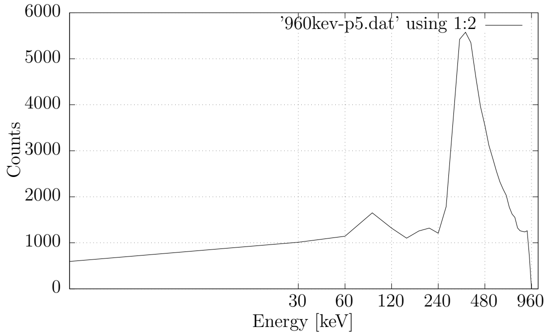

Figure C.16: Energy distribution in pixel 5 with 960 keV.

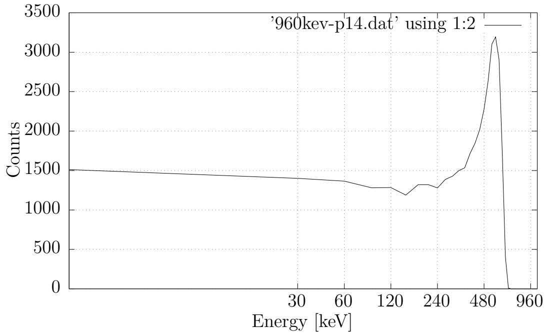

Figure C.17: Energy distribution in pixel 14 with 960 keV.

C.1.7 Electron - 1920 KeV

Pixel	SCT	TAE [keV]	E/e$^-$ [keV]	TAE [%]
P1	904	379.812×10^3	420	0.2
P2	5632	2.340×10^6	415	1.2
P3	920	385.062×10^3	419	0.2
P4	5499	2.240×10^6	407	1.2
P5	N/A	45.495×10^6	455	23.7
P6	5564	2.297×10^6	413	1.2
P7	894	368.009×10^3	412	0.2
P8	5604	2.338×10^6	417	1.2
P9	924	386.557×10^3	418	0.2
P10	1442	666.378×10^3	462	0.4
P11	9491	4.832×10^6	509	2.5
P12	1507	705.479×10^3	468	0.4
P13	9557	4.845×10^6	507	2.5
P14	78681	40.978×10^6	520	21.3
P15	9590	4.789×10^6	499	2.5
P16	1500	680.127×10^3	453	0.4
P17	9607	4.884×10^6	508	2.5
P18	1497	693.678×10^3	463	0.4

Table C.7: Electrons with energy equal to 1920 keV.

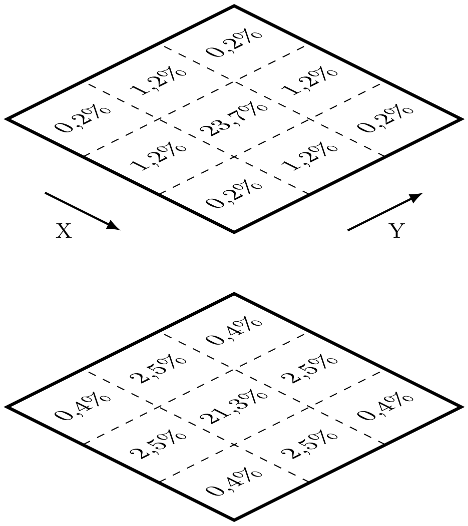

Figure C.18: Total energy distribution in percentage for 1920 keV electrons.

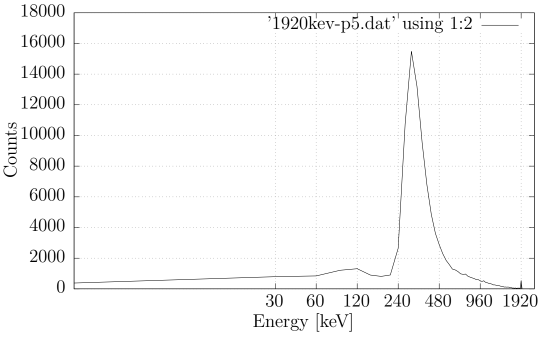

Figure C.19: Energy distribution in pixel 5 with 1920 keV.

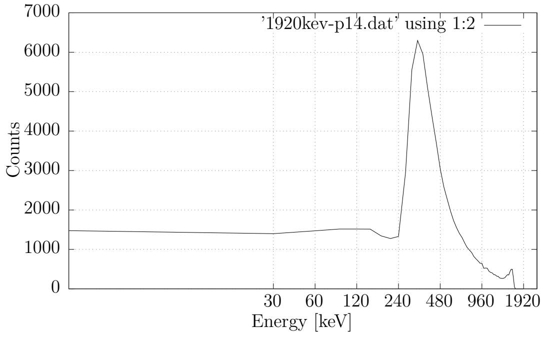

Figure C.20: Energy distribution in pixel 14 with 1920 keV.

C.2 Simulation Setup 2

Information about this setup can be found in chapter 5.4.2.

C.2.1 Electron - 30 KeV

Pixel	SCT	TAE [keV]	E/e$^-$ [keV]	TAE [%]
P1	168	1810	11	0.1
P2	181	2155	12	0.1
P3	190	1882	10	0.1
P4	199	2142	11	0.1
P5	N/A	2.675×10^6	27	89.2
P6	179	1948	11	0.1
P7	182	1860	10	0.1
P8	184	2258	12	0.1
P9	171	1889	11	0.1
P10	65	504	8	0.0
P11	45	349	8	0.0
P12	47	311	7	0.0
P13	36	293	8	0.0
P14	19	155	8	0.0
P15	35	231	7	0.0
P16	62	478	8	0.0
P17	46	375	8	0.0
P18	77	595	8	0.0

Table C.8: Electrons with energy equal to 30 keV.

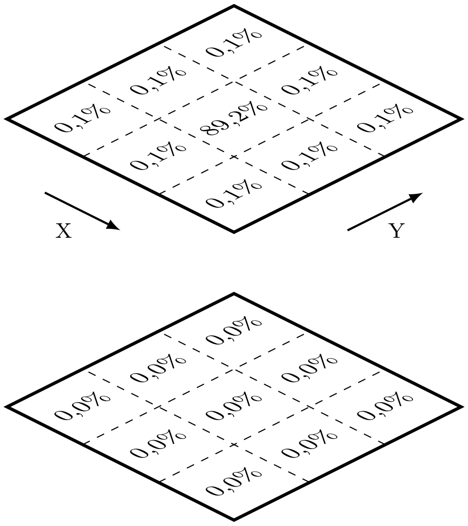

Figure C.21: Total energy distribution in percentage for 30 keV electrons.

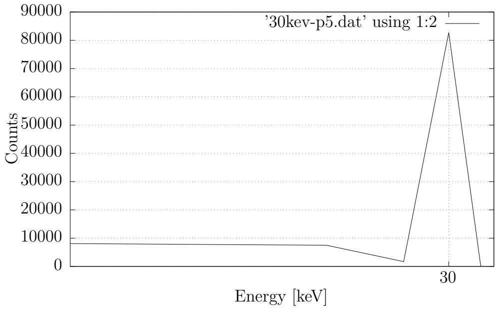

Figure C.22: Energy distribution in pixel 5 with 30 keV.

C.2.2 Electron - 60 KeV

Pixel	SCT	TAE [keV]	E/e$^-$ [keV]	TAE [%]
P1	241	3521	20	0.1
P2	199	6364	26	0.1
P3	199	4261	21	0.1
P4	255	6552	26	0.1
P5	N/A	5.389×10^6	54	89.8
P6	254	7008	28	0.1
P7	166	3185	19	0.1
P8	254	6284	25	0.1
P9	153	3045	20	0.1
P10	56	793	14	0.0
P11	34	543	16	0.0
P12	53	858	16	0.0
P13	32	416	13	0.0
P14	30	543	18	0.0
P15	37	513	14	0.0
P16	57	899	16	0.0
P17	44	596	18	0.0
P18	51	1004	20	0.0

Table C.9: Electrons with energy equal to 60 keV.

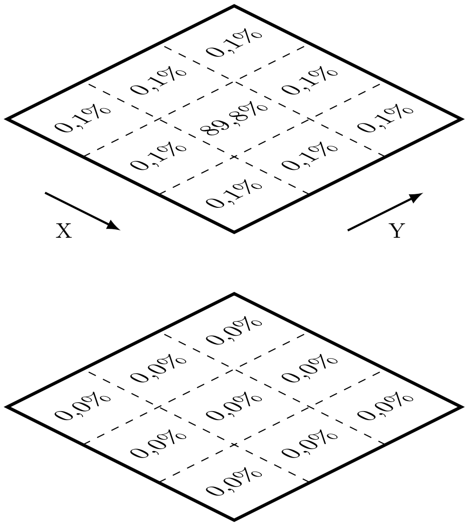

Figure C.23: Total energy distribution in percentage for 60 keV electrons.

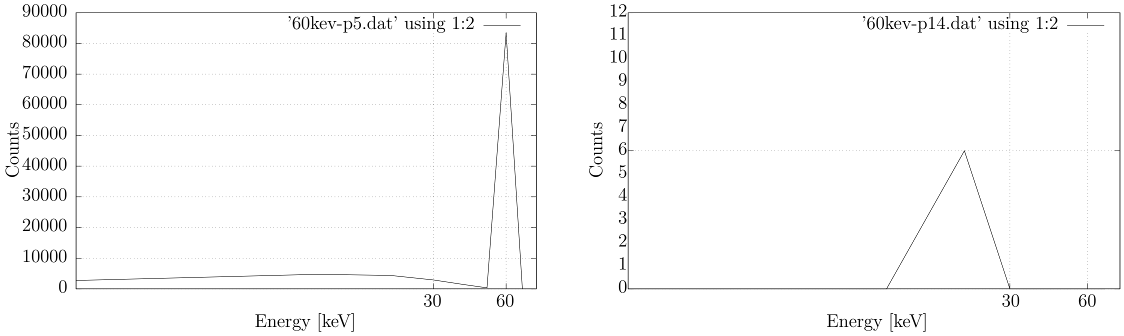

Figure C.24: Energy distribution in pixel 5 with 60 keV.

Figure C.25: Energy distribution in pixel 14 with 60 keV.

C.2.3 Electron - 120 KeV

Pixel	SCT	TAE [keV]	E/e$^-$ [keV]	TAE [%]
P1	166	6730	41	0.1
P2	436	25.302×10^3	58	0.2
P3	175	6699	38	0.1
P4	457	27.297×10^3	60	0.2
P5	N/A	10.806×10^6	108	90.0
P6	442	25.462×10^3	58	0.2
P7	174	7020	40	0.1
P8	452	25.391×10^3	56	0.2
P9	200	7801	39	0.1
P10	63	1778	28	0.0
P11	52	1634	31	0.0
P12	60	1779	30	0.0
P13	39	1315	34	0.0
P14	31	852	28	0.0
P15	46	1306	28	0.0
P16	76	2334	31	0.0
P17	29	843	29	0.0
P18	60	1765	29	0.0

Table C.10: Electrons with energy equal to 120 keV.

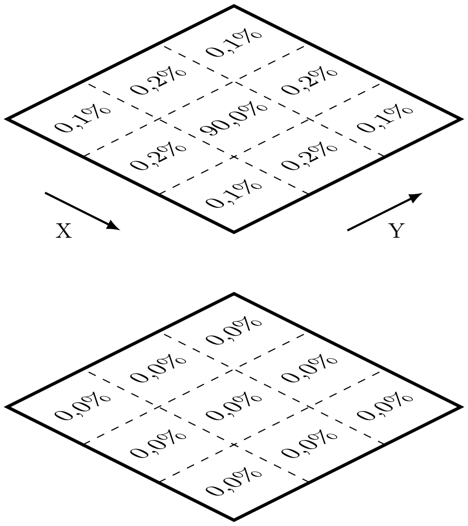

Figure C.26: Total energy distribution in percentage for 120 keV electrons.

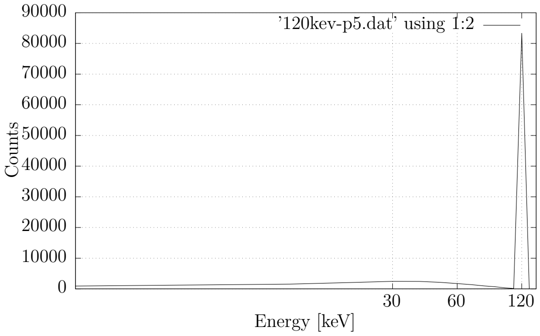

Figure C.27: Energy distribution in pixel 5 with 120 keV.

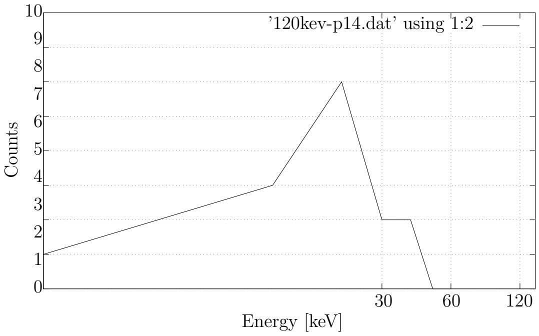

Figure C.28: Energy distribution in pixel 14 with 120 keV.

C.2.4 Electron - 240 KeV

Pixel	SCT	TAE [keV]	E/e$^-$ [keV]	TAE [%]
P1	177	13.985×10^{3}	79	0.1
P2	1012	127.145×10^{3}	126	0.5
P3	190	14.420×10^{3}	76	0.1
P4	1065	136.432×10^{3}	128	0.5
P5	N/A	21.507×10^{6}	215	89.6
P6	1000	125.071×10^{3}	125	0.5
P7	170	12.966×10^{3}	76	0.1
P8	1040	129.347×10^{3}	124	0.5
P9	178	13.604×10^{3}	76	0.1
P10	69	3794	55	0.0
P11	48	2710	57	0.0
P12	72	3587	50	0.0
P13	46	2227	48	0.0
P14	62	2611	42	0.0
P15	45	2206	49	0.0
P16	82	4654	57	0.0
P17	50	2501	50	0.0
P18	57	6921	69	0.0

Table C.11: Electrons with energy equal to 240 keV.

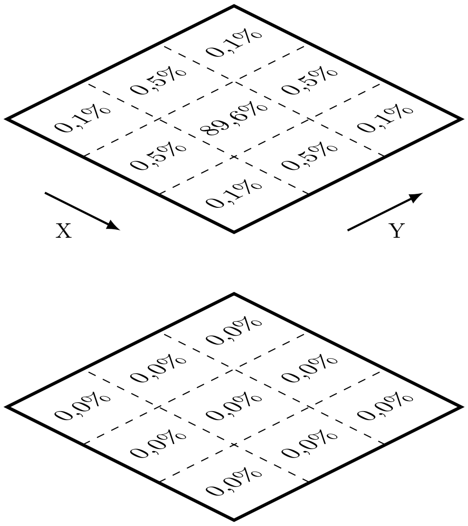

Figure C.29: Total energy distribution in percentage for 240 keV electrons.

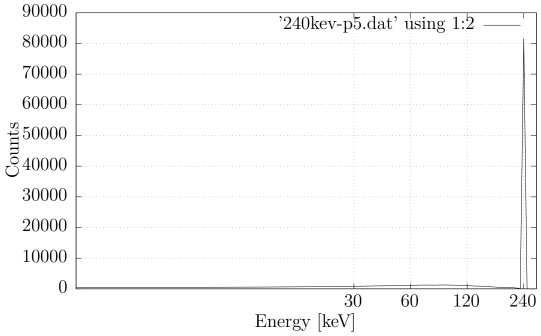

Figure C.30: Energy distribution in pixel 5 with 240 keV.

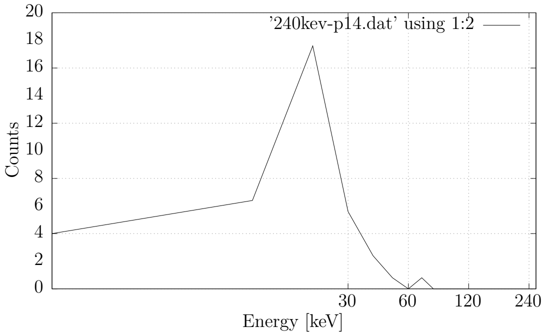

Figure C.31: Energy distribution in pixel 14 with 240 keV.

C.2.5 Electron - 480 KeV

Pixel	SCT	TAE [keV]	E/e$^-$ [keV]	TAE [%]
P1	207	29.210×10^3	141	0.1
P2	2491	630.875×10^3	253	1.4
P3	202	28.821×10^3	143	0.1
P4	2700	690.301×10^3	256	1.4
P5	N/A	41.918×10^6	419	87.3
P6	2583	662.809×10^3	257	1.4
P7	194	28.950×10^3	149	0.1
P8	2613	658.075×10^3	252	1.4
P9	202	30.015×10^3	149	0.1
P10	58	5386	93	0.0
P11	63	3450	55	0.0
P12	62	5208	84	0.0
P13	66	5170	78	0.0
P14	154	5580	36	0.0
P15	65	4434	68	0.0
P16	72	6406	89	0.0
P17	70	4150	59	0.0
P18	64	5454	85	0.0

Table C.12: Electrons with energy equal to 480 keV.

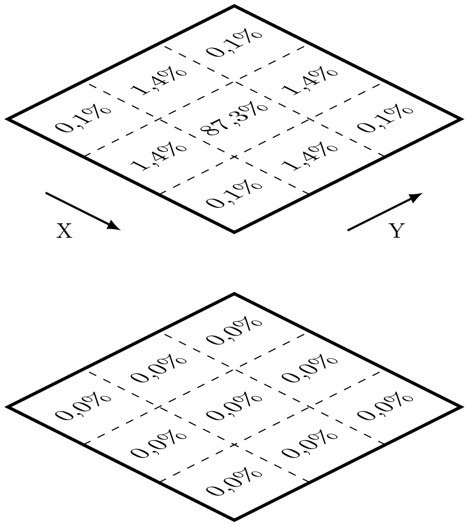

Figure C.32: Total energy distribution in percentage for 480 keV electrons.

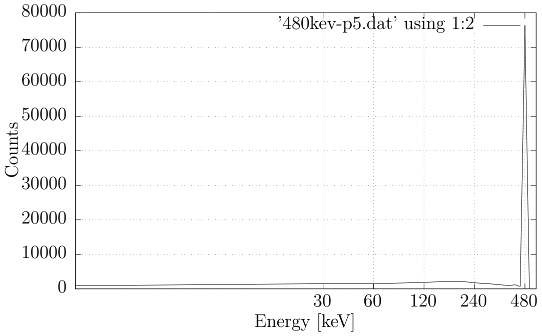

Figure C.33: Energy distribution in pixel 5 with 480 keV.

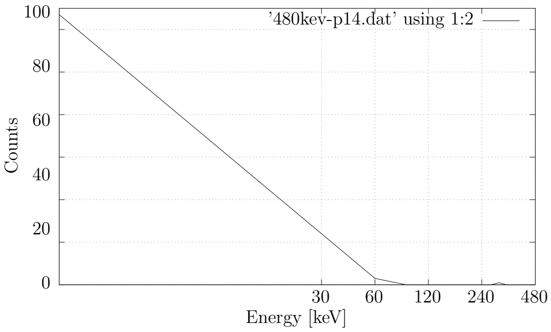

Figure C.34: Energy distribution in pixel 14 with 480 keV.

C.2.6 Electron - 960 KeV

Pixel	SCT	TAE [keV]	E/e$^-$ [keV]	TAE [%]
P1	573	140.533×10^3	245	0.2
P2	5791	2.292×10^6	384	2.4
P3	633	165.125×10^3	261	0.2
P4	6103	2.331×10^6	383	2.4
P5	N/A	60.978×10^6	610	63.5
P6	6262	2.406×10^6	384	2.4
P7	628	17.219×10^3	275	0.2
P8	6005	2.296×10^6	382	2.4
P9	611	156.477×10^3	256	0.2
P10	447	92.432×10^3	207	0.1
P11	3370	1.004×10^6	298	1.1
P12	415	92.786×10^3	224	0.1
P13	3546	1.030×10^6	290	1.1
P14	39555	15.300×10^6	387	15.9
P15	3436	1.016×10^6	296	1.1
P16	425	93.823×10^3	221	0.1
P17	3344	1.008×10^6	301	1.1
P18	412	92.436×10^3	224	0.1

Table C.13: Electrons with energy equal to 960 keV.

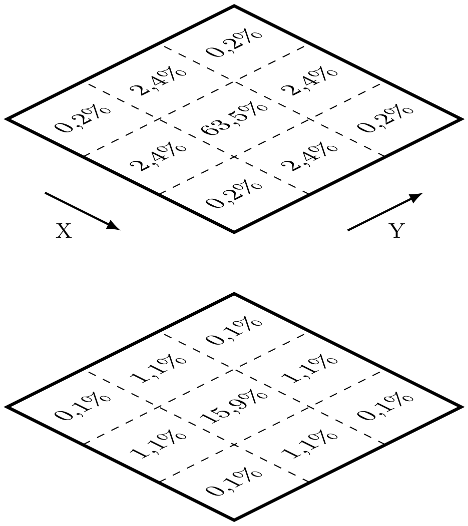

Figure C.35: Total energy distribution in percentage for 960 keV electrons.

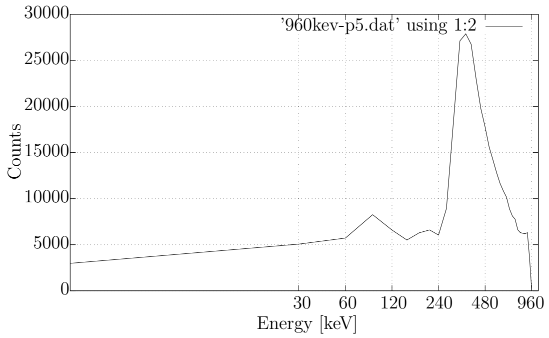

Figure C.36: Energy distribution in pixel 5 with 960 keV.

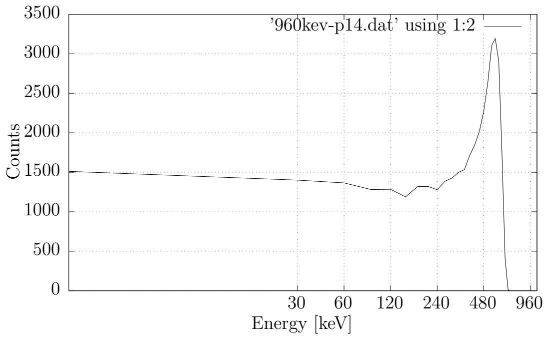

Figure C.37: Energy distribution in pixel 14 with 960 keV.

C.2.7 Electron - 1920 KeV

Pixel	SCT	TAE [keV]	E/e$^-$ [keV]	TAE [%]
P1	1463	556.521×10^3	380	0.3
P2	6179	2.519×10^6	408	1.3
P3	1544	584.545×10^3	379	0.3
P4	6004	2.460×10^6	410	1.3
P5	N/A	45.780×10^6	458	23.8
P6	6288	2.555×10^6	408	1.3
P7	1483	573.007×10^3	386	0.3
P8	6232	2.569×10^6	412	1.3
P9	1483	589.585×10^3	398	0.3
P10	3509	1.594×10^6	454	0.8
P11	11967	6.030×10^6	504	3.2
P12	3441	1.554×10^6	452	0.8
P13	11843	5.977×10^6	505	3.2
P14	79354	42.819×10^6	540	22.3
P15	12082	6.144×10^6	509	3.2
P16	3450	1.559×10^6	452	0.8
P17	11893	6.059×10^6	509	3.2
P18	3457	1.551×10^6	449	0.8

Table C.14: Electrons with energy equal to 1920 keV.

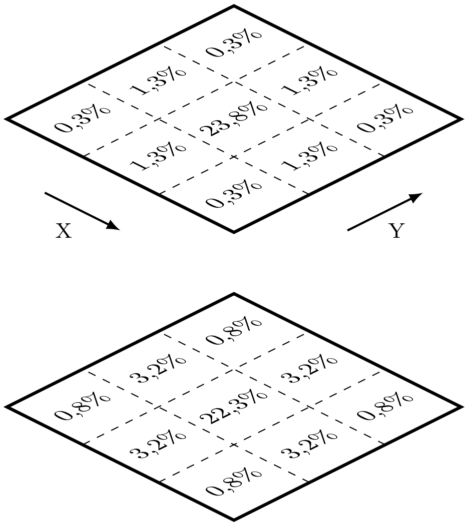

Figure C.38: Total energy distribution in percentage for 1920 keV electrons.

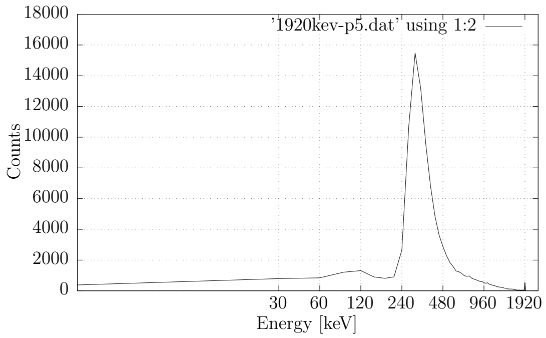

Figure C.39: Energy distribution in pixel 5 with 1920 keV.

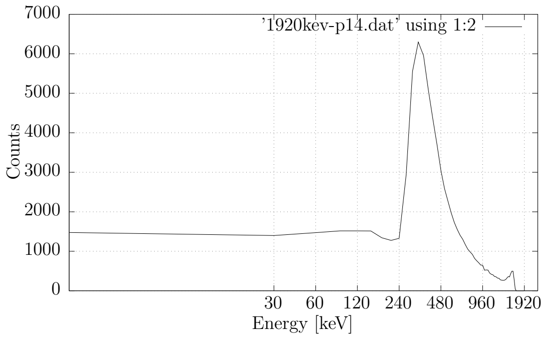

Figure C.40: Energy distribution in pixel 14 with 1920 keV.

APPENDIX D

GATE Simulation Repository

All the steps of the GATE simulation development process has been carefully tracked by employing Git. Below is the outline of the structure of the **gate_simulation**[1] repository. Every simulation folder has the same subfolder structure as the sim_setup_1.

```
gate_simulation
├📁sim_setup_1                 # execution from this folder
│ ├📁output                    # .ROOT and .csv results
│ ├📁mac                       # macrofile for GATE
│ ├📁data                      # material database for GATE
│ ├📁src                       # macro and readout file for ROOT
│ ├📁doc                       # simulation and readout reports
│ └README.md
├📁sim_setup_wide
├📁sim_setup_baffle
├📁sim_setup_mask
├📁physics_list_validation
├📁2mm_thick_silicon_layer
└📁proton_range
```

---

[1] git.app.uib.no/Hogne.Andersen/DEEP/tree/master/gate_simulation

APPENDIX E

Testbench Framework Repository

All the steps of the testbench framework development process has been carefully tracked by employing Git. Below is the outline of the structure of the **testbench_framework**[1] repository.

```
testbench_framework
├─deep_dsp               # testbench framework
│ ├─doc                  # simulation report
│ ├─script               # scripts for automation
│ ├─sim                  # temporary simulation files
│ ├─src                  # .vhdl file for the device
│ ├─tb                   # testbench file for the device
│ └─README.md
├─bitvis_vip_sbi         # testbench library
└─uvvm_util              # testbench library
```

---

[1] git.app.uib.no/Hogne.Andersen/DEEP/tree/master/testbench_framework

Bibliography

[1] H. N. Tyssøy, J. Stadnes, F. Søraas, K. Ullaland, and D. Röhrich, "Distribution of Energetic Electron and Proton (DEEP) Instrument Conceptual design report - Simplified vs ideal version," University of Bergen, Tech. Rep., Oct. 2017.

[2] Birkeland Centre for Space Science, "How is the Earth coupled to space?" [Online]. Available: https://birkeland.h.uib.no/

[3] Glenn Elert, "The Physics Hypertextbook." [Online]. Available: http://physics.info/fusion/

[4] J. Stadsnes and K. Snekvik, "Lecture notes for PHYS251 - Near Earth Space, University of Bergen."

[5] National Aeronautics and Space Administration, "Coronal Mass Ejections, Solar Flares, and the Sun-Earth Connection," 2015. [Online]. Available: http://hesperia.gsfc.nasa.gov/sftheory/cme.htm

[6] Store Norske Leksikon, "Solvinden," 2012. [Online]. Available: https://snl.no/solvinden

[7] HowStuffWorks, "Van Allen Radiation Belts." [Online]. Available: http://science.howstuffworks.com/dictionary/astronomy-terms/van-allen-radiation-belts-info.htm

[8] Hilde N. Tyssøy, "email correspondence," Jun. 2018.

[9] David P. Stern and Mauricio Peredo, "Trapped Radiation – History." [Online]. Available: https://www-istp.gsfc.nasa.gov/Education/whtrap1.html

[10] Linn-Kristine G. Ødegaard, "Energetic particle precipitation into the middle atmosphere - optimization and applications of the NOAA POES MEPED data," Ph.D. dissertation, University of Bergen, 2016.

[11] The Australian Antarctic Division, “Middle atmosphere.” [Online]. Available: http://www.antarctica.gov.au/about-antarctica/environment/atmosphere/middle-atmosphere

[12] Space.com, “Earth’s Atmosphere: Composition, Climate & Weather.” [Online]. Available: https://www.space.com/17683-earth-atmosphere.html

[13] Martin Seelye (University of Washington), *Introduction to Ocean Remote Sensing.* Cambridge University Press, 2014.

[14] E. Turunen, P. T. Verronen, A. Seppälä, C. J. Rodger, M. A. Clilverd, J. Tamminen, C.-F. Enell, and T. Ulich, “Impact of different energies of precipitating particles on NOx generation in the middle and upper atmosphere during geomagnetic storms,” *Journal of Atmospheric and Solar-Terrestrial Physics*, vol. 71, no. 10-11, pp. 1176–1189, jul 2009.

[15] Glenn F. Knoll, *Radiation Detection And Measurement, 4Th Edition.* Wiley India, 2011.

[16] Herman Cember and Thomas E. Johnson, *Introduction to Health Physics: Fourth Edition.* McGraw-Hill Education, LLC CoreSource, 2008.

[17] National Institute of Standards and Technology, “Appendix: Significance of Calculated Quantities.” [Online]. Available: https://physics.nist.gov/PhysRefData/Star/Text/appendix.html

[18] Helmuth Spieler, *Semiconductor Detector Systems (Series on Semiconductor Science and Technology).* Oxford University Press, 2005.

[19] Chris Leonard, “Challenges for Electronic Circuits in Space Applications.” [Online]. Available: http://www.analog.com/en/technical-articles/challenges-for-electronic-circuits-in-space-applications.html

[20] Syed N. Ahmed, *Physics and Engineering of Radiation Detection.* Elsevier Science & Technology, 2014.

[21] Neil H. E. Weste and David M. Harris, *Integrated Circuit Design: International Version: A Circuits and Systems Perspective.* Pearson Education, 2010.

[22] John P. Bentley, *Principles of Measurement Systems (4th Edition).* Pearson Education, 2004.

[23] K. Yando, R. M. Millan, J. C. Green, and D. S. Evans, “A monte carlo simulation of the NOAA POES medium energy proton and electron detector instrument,” *Journal of Geophysical Research: Space Physics*, vol. 116, no. A10, oct 2011.

[24] Torstein Frantzen, "email correspondence," May 2018.

[25] K. Shimazoe, H. Takahashi, B. Shi, T. Orita, T. Furumiya, J. Ooi, and Y. Kumazawa, "Dynamic time over threshold method," *IEEE Transactions on Nuclear Science*, vol. 59, no. 6, pp. 3213–3217, dec 2012.

[26] Are Haslum, "under development," Ph.D. dissertation, University of Bergen, 2020.

[27] Microsemi, "RTG4 Radiation-Tolerant FPGAs." [Online]. Available: https://www.microsemi.com/product-directory/rad-tolerant-fpgas/3576-rtg4

[28] Microsemi, "SmartFusion2 SoC FPGAs." [Online]. Available: https://www.microsemi.com/product-directory/soc-fpgas/1692-smartfusion2

[29] Geant4 Collaboration, "Physics Lists EM constructors in Geant4 10.4." [Online]. Available: http://geant4.web.cern.ch/node/1731

[30] National Institute of Standards and Technology, "ESTAR." [Online]. Available: https://physics.nist.gov/PhysRefData/Star/Text/ESTAR.html

[31] National Institute of Standards and Technology, "PSTAR." [Online]. Available: https://physics.nist.gov/PhysRefData/Star/Text/PSTAR.html

[32] M. J. Berger, S. M. Seltzer, S. E. Chappell, J. C. Humphreys, and J. W. Motz, "Tables of Response Functions for Silicon Electron Detectors," National Bureau of Standars, Tech. Note 489, 1969.

[33] E. D. Peck, C. E. Randall, J. C. Green, J. V. Rodriguez, and C. J. Rodger, "POES MEPED differential flux retrievals and electron channel contamination correction," *Journal of Geophysical Research: Space Physics*, vol. 120, no. 6, pp. 4596–4612, jun 2015.

[34] Johan Stadsnes, "email correspondence," Jun. 2018.

[35] Arm Developer, "Cortex-M3." [Online]. Available: https://developer.arm.com/products/processors/cortex-m/cortex-m3/

[36] M. Morris Mano and Charles Kime, *Logic and Computer Design Fundamentals, Third Edition.* Prentice Hall, 2003.

[37] Mats F. Heigre, "Evaluation and Design of Embedded Readout System for the ALOFT Gamma-Ray Detector Instrument," Master's thesis, University of Bergen, 2018.

[38] Alexander N. Nesse, "Electronic Readout SoC Design for Measurement of Gamma Radiation," Master's thesis, University of Bergen, 2018.

[39] Bitvis, “Universal VHDL Verification Methodology.” [Online]. Available: https://bitvis.no/dev-tools/uvvm/

[40] OpenGATE Collaboration, “Users Guide.” [Online]. Available: http://wiki.opengatecollaboration.org/index.php/Users_Guide

[41] OpenGATE Collaboration, “FAQ.” [Online]. Available: http://www.opengatecollaboration.org/FAQ

[42] OpenGATE Collaboration, “GATE 8.1.” [Online]. Available: http://www.opengatecollaboration.org/node/82

[43] Geant4 Collaboration, “Geant4 10.4 Release Notes.” [Online]. Available: http://geant4-data.web.cern.ch/geant4-data/ReleaseNotes/ReleaseNotes4.10.4.html

[44] CERN, “ROOT - Reference Guide.” [Online]. Available: https://root.cern.ch/doc/master/classTTree.html